# Cable Driven Robots: Hysteretic Cable Stretch, Cable-Pulley Network Friction, Fatigue Life, and Kinematics of Two-Arm Multi Staged Flexible Manipulator

Muneaki Miyasaka

A dissertation

submitted in partial fulfillment of the

requirements for the degree of

Doctor of Philosophy

University of Washington

2017

Reading Committee:

Blake Hannaford, Chair

Brian Fabien

Santosh Devasia

Program Authorized to Offer Degree:
Mechanical Engineering

University of Washington

## Abstract

Cable Driven Robots: Hysteretic Cable Stretch, Cable-Pulley Network Friction, Fatigue Life, and Kinematics of Two-Arm Multi Staged Flexible Manipulator

Muneaki Miyasaka

Chair of the Supervisory Committee:
Professor Blake Hannaford
Department of Electrical Engineering

Cable driven mechanisms face control challenges associated with hysteretic response of cable and dynamic friction from guide pulleys due to variable cable tension. In this thesis, a new dynamic models of cable driven mechanism, cable-pulley network friction and hysteretic stretch of longitudinally loaded cable, are developed in order to improve control accuracy and robustness. Moreover, fatigue life of cable is investigated and a prediction model is presented which can ensure safe operation of the robot. The specifications used for the experimental setups for the model development are based on the RAVEN II cable driven surgical robot and the model verification was performed using the same system.

This thesis also presents the kinematics of the Roboscope, surgical robot for skullbase surgery and neurosurgery. The system has two-arm flexible cable driven manipulator which faces coupling effect. Detailed kinematics the system with the coupling effect is developed and analyzed.

# TABLE OF CONTENTS

# LIST OF FIGURES

# ACKNOWLEDGMENTS

I would like to thank to my adviser prof. Blake Hannaford, my Ph.D. advisory committee members prof. Brian D. Flinn, prof. Brian Fabien, and prof. Santosh Devasia, the members of the UW BioRobotics lab, the Korean Institute of Advanced Technology (KIST, Dr. Hujoon Project), and National Science Foundation via Stanford University (grant number 1227406) for their support and contribution throughout the entire project.

# Chapter 1
# GUIDE TO THIS THESIS

The main theme of this thesis is "cable" or "wire rope" used for actuation in robotics field. The goal of chapter 2, 3, and 4 is to improve the position accuracy of cable driven robots by developing a detailed dynamic model. In chapter 2, friction at cable guide pulley is investigated. Cable tension changes during operation of cable driven robots and the friction at each pulley fluctuates because of that. This subsequently affects the robot's dynamics. Chapter 3 inquires the response of the cable to the strain applied. Cable consists of a bundle of strands and wires. Due to the inter strand and wire movement, the response of the cable becomes complex. The models developed in chapters 2 and 3 are applied to the RAVEN II cable-driven surgical robot and the performance was evaluated in chapter 4.

Fatigue of the cable is another problem of the cable driven mechanisms. Chapter 5 investigates the fatigue life of the cable due to bending over the sheave. This type of fatigue is significant especially robot with light payload such as the RAVEN II. By predicting the fatigue life of the cable, cable can be replaced before failure and the robot can be operated safely.

Roboscope is a surgical robot designed for skullbase surgery and neuro-surgery which has cable-driven, flexible, multi-staged joints. Because of the structure, the Roboscope experiences strong coupling effect. In chapter 6, detailed derivation of the kinematics together with the coupling effect is presented.

Even though the platforms we employ and analysis we perform are based on surgical robots, this study could be extended to any other cable driven mechanisms if they have the similar specifications presented.

# Chapter 2

# CABLE-PULLEY NETWORK FRICTION

## *2.1 Introduction*

Robotic surgery has become an increasingly popular alternative to traditional minimally-invasive surgery. FDA-approved systems such as the da Vinci surgical system (Intuitive Surgical, Inc.) have been used for well over a decade, and provide advantages such as the ability to scale motions, eliminate physiologic tremors, and improve dexterity [43].

Since minimally-invasive surgery requires a long and thin tool to be inserted into the patient's body, surgical robots are primarily cable driven systems. Generally, cables used for surgical robots have a diameter of less than a few millimeters and consist of multiple strands helically surrounding a center core strand. When the cable is under stress, it exhibits unique and complex behavior due to its structure. Townsend [79] investigated input and output relations of tension element drives (e.g. cable, belt) and analyzed efficiencies based on thermodynamic principles. Also, autonomous surgical robotics has recently been the focus of research [34] [50], and [33]. However, control systems for cable driven robots with sufficient accuracy for medical automation have not yet been developed.

The eventual goal of our research is to improve the performance of control by accurately defining a dynamic model of the system that takes into account cable stretch and friction. Our application is to achieve better position control of the RAVEN II Surgical Robotic Research Platform (Fig. 2.1) [29]. Developed by the University of Washington's BioRobotics Lab, the RAVEN II has a workspace with three joints (two rotational and one prismatic) and a four Degree of Freedom (DOF) tool head, totaling seven cable drives. The cable to transmit motor torque to each joint traverses multiple pulleys of three different diameters. Currently, control of each joint is based on an encoder and motor fixed on the proximal end

of the cable. Therefore, accurate position and force control of the robot is susceptible to position errors between the motor and joint due to cable stretch, and force errors due to cable-pulley friction.

The contribution of this chapter is the development of a cable-pulley interaction model of Coulomb and viscous friction based on experimental measurements. The model and the experimental procedures can be applied to cable-driven systems with structure, tension, load, and cable and pulley parameters similar to the RAVEN II.

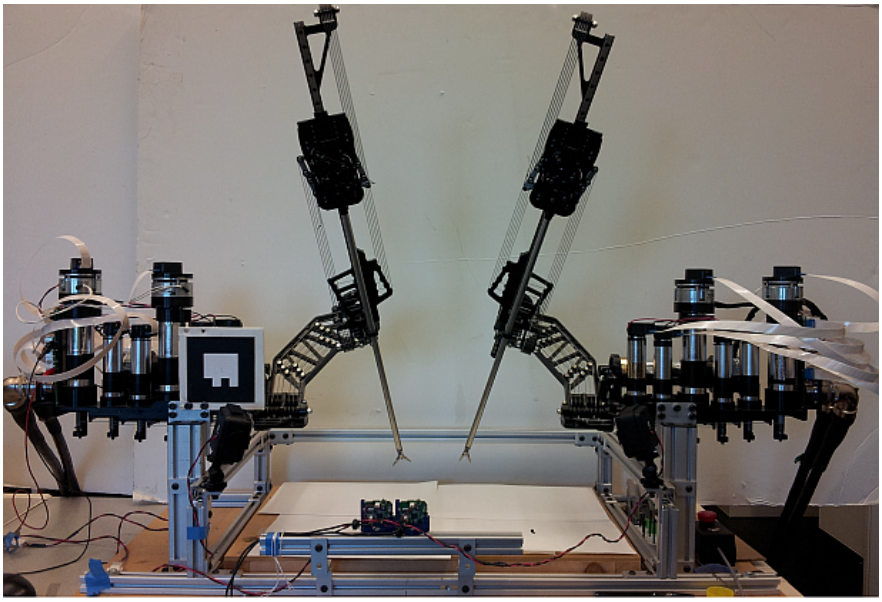

Figure 2.1: The RAVEN II Surgical Robot is the target system in this research.

## *2.2 Cable Related Force Model*

Ramadurai et al. [65] developed a dynamic model of the RAVEN II for the purpose of simulation. The model associated with cable stretch consists of an exponential spring and linear dashpot system with constant parameters. The pulley friction is combined with motor friction and treated as a force with constant parameters. In [40], Kosari et al. used a similar cable force model for a single DOF RAVEN mock-up system to identify model parameters.

Each parameter was dynamically adjusted and estimated using position feedback from an encoder mounted on a joint with the use of an Unscented Kalman Filter.

When a cable is in motion under tension, ideal pulleys rotate without slip at the cable and pulley interface. As pulleys rotate, the frictional force at the pulley bearing disturbs the motion, causing frictional loads on the cable. Because tension varies when linkages are actuated and it changes the load on the pulley bearing, friction due to cable-pulley interaction should be a function of tension. Also, internal motion of cables exhibits internal damping with hysteresis behavior. There are a number of studies dedicated to modeling the behavior of cables under load, both static and dynamic, but most focus on models of bending, lateral vibration, or large-diameter cables and they are not directly applicable for surgical robot systems. Spak et al. summarizes established and recently developed modeling methods of helically twisted cable and categorized the internal damping models based on their mechanisms, the inter-wire friction, variable bending stiffness, and material internal friction [77]. One of the related studies discussed is [71] in which Sauter uses a Masing model [53] to capture dynamic behavior of stockbridge dampers. Alternate hysteritic models include the Bouc-Wen hysteresis model [85] which is used to describe a wide range of systems that show hysteresis characteristics and is investigated for modeling a wire rope spring in [61]. A detailed model of hysteretic force is out of the scope of this chapter but in general, hysteretic forces are modeled as a function of displacement, velocity, and a hysteretic variable.

Based on the existing literature [65], [40], [76] and an analysis of the structure of the robot, the force on the pulling side of a cable ($F_{Pulling}$) can be modeled with cable hysteretic force ($F_h$), cable damping ($F_d$), and cable-pulley friction ($F_p$). Hysteretic force is defined as a function of the difference in the joint side and motor side displacement ($\Delta x$) and velocity ($\Delta \dot{x}$) and the hysteretic variable ($z$), while cable-pulley friction is defined as a function of tension ($T$) as well as three possible variables: cable velocity ($\dot{x}$), number of pulleys ($n_p$), and wrap angle ($\theta_w$).

$$F_{Pulling} = F_h[\Delta x, \Delta \dot{x}, z] + F_d[\Delta \dot{x}] + F_p[T, \dot{x}, n_p, \theta_w] \tag{2.1}$$

Eytelwein's formula relates the drop in the tension of flexible element which is wound around a cylindrical object such as pulley and capstan. The equation is a function of the warp angle. However, the actual change in cable tension across pulley is related to the pulley bearing friction since that is where the slippage occurs. Therefore, Eytelwen's fomula is not applicable. Friction coefficient of sliding bearing can be calculated using Petroff equation. However, according to the the experimental results from Lee et al. [46], the equation is not valid for surgical robot instruments with cable pulley structure. They found out the friction proportionally increases as the cable's pretension increases. Yu et al. [91] also experimentally measured the force transmitted by cable for a cable driven surgical robot instrument with idler pulleys and the model was obtained from a curve fitting method. However, both work do not explicitly present a model of cable pulley friction. Kraus et al. [41] modeled force transmitted by cable running through multiple guide pulleys using Dahl and Coulomb friction models but the model requires force sensor measurements near the winches.

Since no generalized model currently exist, cable/pulley network friction needs to be developed based on a generic friction model. A friction model generally consists of four terms; Coulomb, viscous, stiction, and Stribeck friction [62]. Coulomb friction is the constant frictional force whose sign is determined by the direction of motion. Viscous friction is the linear increase of friction as a function of velocity. Stiction or stick-slip friction is the frictional force at rest and its highest value is typically greater than the magnitude of Coulomb friction. Stribeck term is the non-linear change of friction at low velocity regime. The friction drops from the highest stiction value toward the Coulomb friction as velocity increases due to presence of lubrication film. Moreover, friction becomes complex when velocity is zero, called pre-sliding friction dynamics, where friction shows backlash or hysteresis response. However, we will ignore the pre-sliding friction because pre-sliding occurs when the displacement is very small (in the range of micro meter) and has negligible effect to the entire robot dynamics. The pulleys we use consist of rolling-element bearings which can be considered to have no

stiction [16] and it consequently indicates Stribeck friction can also be omitted from the model. Hence, the cable-pulley friction ($F_p$) is written as

$$F_p = f_c[T, n_p, \theta_w] sign(\dot{x}) + f_v[T, n_p, \theta_w]\dot{x} \tag{2.2}$$

where $f_c$ and $f_v$ are Coulomb and viscous friction from cable-pulley interaction, respectively, and $\dot{x}$ is the velocity of the running cable. In this work, we focus on determining the model of the cable-pulley friction (2.2) based on experimentally measured data.

### *2.3 Identification of Cable-Pulley Friction Model*

The range of cable tension and cable velocity for the experiment was determined based on measurements of the actual tensions and velocities observed in use of the RAVEN II. Cable tension ranges up to 33 N and velocities peak at 12 m/s. While the absolute maximum value of observed velocity is 12 m/s, this is very rare and thus the upper limit of cable velocity for the experiments was set to the empirical RMS value of 1.3 m/s. The cable and pulleys used in this experiment are the same as those used in the construction of the RAVEN II. The cable is pre-stretched and it is assumed creep does not occur. Also, it is assumed there is no slip at the cable and pulley interface because slippage generally occurs when operation velocity is high. The cable is made out of type 304 stainless steel and has a construction of 7 twisted strands of 19 individual wires, a diameter of 0.61 mm, and breaking strength of 311 N. Material of the pulley is 6061 aluminum with hard anodized finish and the sheave diameters are 7.6 mm (small), 15.64 mm (medium), and 22.9 mm (large) (Fig. 2.2). The pulley bearings have dynamic and static load ratings of 29.03 N and 9.07 N for the small pulleys and 36.74 N and 13.15 N for medium and large pulleys.

The RAVEN II uses up to 13 small, 10 medium, and 2 large pulleys per cable run. The individual wrap angle ($\theta_{w,i}$) is 30°-180° for small and medium pulleys with the average individual wrap angles ($\theta_{w,i,av}$) of 70° and 75° respectively and for large pulley, both $\theta_{w,i}$ and $\theta_{w,i,av}$ are 180°. However, during the experiment we used up to 19 pulleys and extended

uniform $\theta_{w,i}$ and $\theta_{w,i,av}$ ranges of 15°-180° and 45°-150° for all pulleys in order to compare them side by side and investigate their behavior in depth.

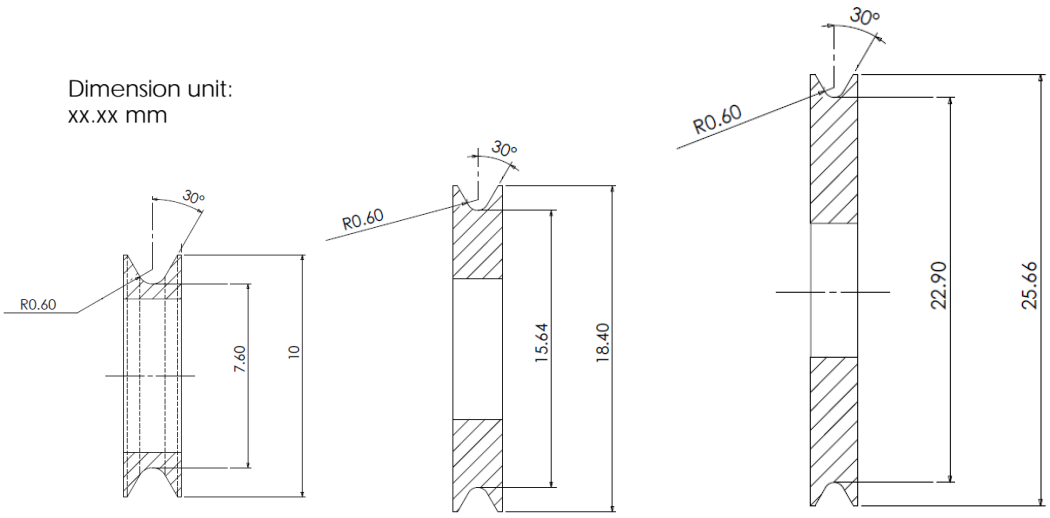


Figure 2.2: Small, medium, and large pulleys (from left to right) used for the RAVEN II.

### *2.3.1 Motor Driven System*

*Setup*

We constructed the test setup shown in Fig. 2.3 to test how cable velocity correlates to pulley friction. In order to eliminate the dynamic force and exclusively investigate the viscous friction of the test pulleys, the cable was driven at constant speed. The cable running through an array of pulleys was fixed at a capstan mounted on a motor and the cable tension was kept with a mass hung at the other end of the cable. The system uses a PID controller to run the cable at a targeted constant velocity. The motor and servo amplifier used are a Maxon RE 30 brushed motor and an AMC Z12A8, the same as the ones used for the RAVEN II system. For I/O, an Arduino Mega 2560 chip was employed. The Arduino provides control signals to the motor via servo amplifier and acquires motor current for analysis. Motor current was converted to torque based on the motor specification which was assumed to be

accurate. Motor friction at each constant speed was measured and subtracted to obtain just the cable-pulley friction. The software runs roughly at 5 kHz and is capable of generating and measuring cable velocity of 7 m/s and cable tension of 48 N.

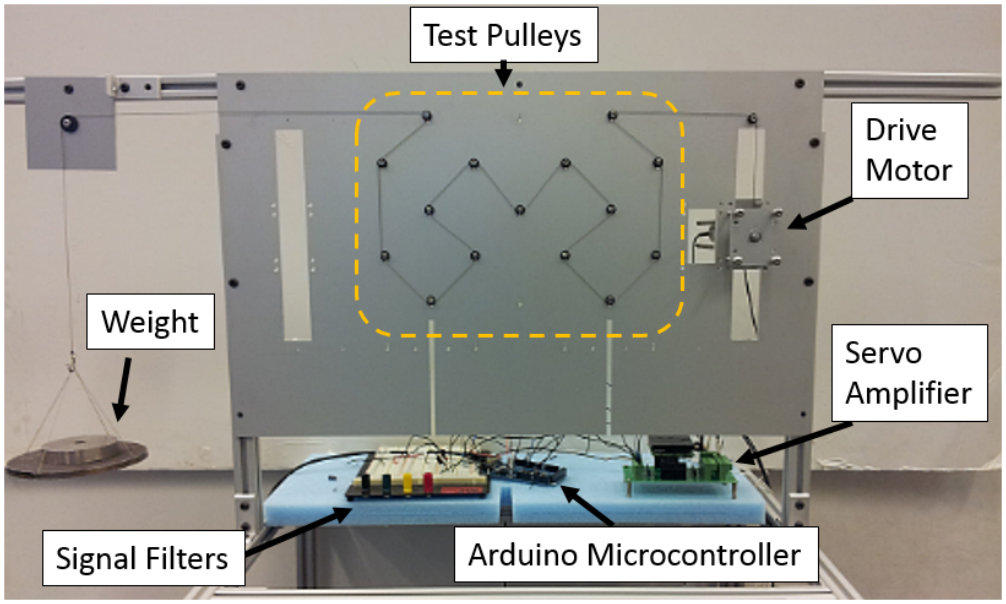


Figure 2.3: Motor driven pulley board. The motor (right side) moves cable through the pulleys and tension is set by weight (left side).

*Measurements and Results*

In order to test dependency of each variable on the cable-pulley viscous friction at a time, we plotted the cable-pulley friction as a function of one variable while holding other variables as constants.

We first collected data for 9 medium-size test pulleys, keeping $\theta_{w,i,av}$ of 85°, while applying various constant tensions. Since tension is not consistent throughout the cable due to the friction at each pulley, we defined a nominal tension as the average of capstan side tension and mass side tension. The results are summarized in Fig. 2.4. The data contain some noise when reading the motor current and determining the cable-pulley friction and it is amplified

for the larger tension. The plot shows that data are scattered around the mean without trend of friction force being a linear function of cable velocity.

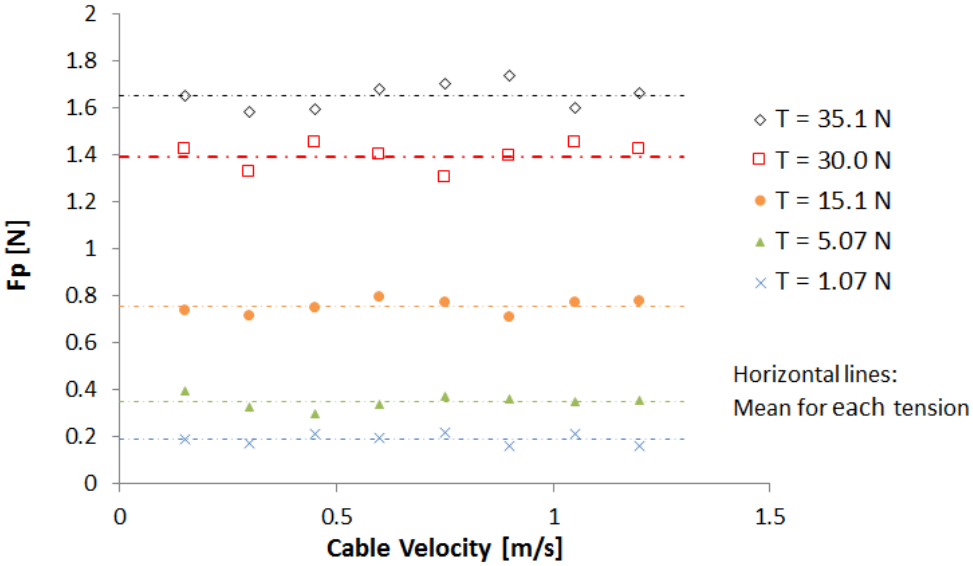


Figure 2.4: Cable-pulley friction against cable velocity for a setup with 9 medium pulleys and $\theta_{w,i,av} = 85°$ at five different tensions.

Likewise, the data for the small and large pulleys were collected for three different tensions each and results are plotted in Fig. 2.5. All data points are around the mean and do not exhibit definite increasing trend as tension varies for both small and large pulleys. Hence, it can be concluded that viscous friction is not a function of cable tension.

Next, $\theta_{w,i,av}$ was changed to 50° and 135° while keeping the number of the pulley the same (Fig. 2.6). To keep the tension constant, 1.5 kg mass was applied and the nominal tensions are calculated to be 15.8, 15.1, and 15.0 N for small, medium, and large pulley respectively. These tensions are also used in Fig. 2.4 and 2.5 so that the results for $\theta_{w,i,av} = 85°$ can be comparable. The results indicate that there is no dependency of the wrap angle on the viscous friction.

We then employed 5 and 15 pulleys with $\theta_{w,i,av}$ of 85° and took measurements for the same tension used in the previous plot (Fig. 2.7). Including the results for 9 pulleys from

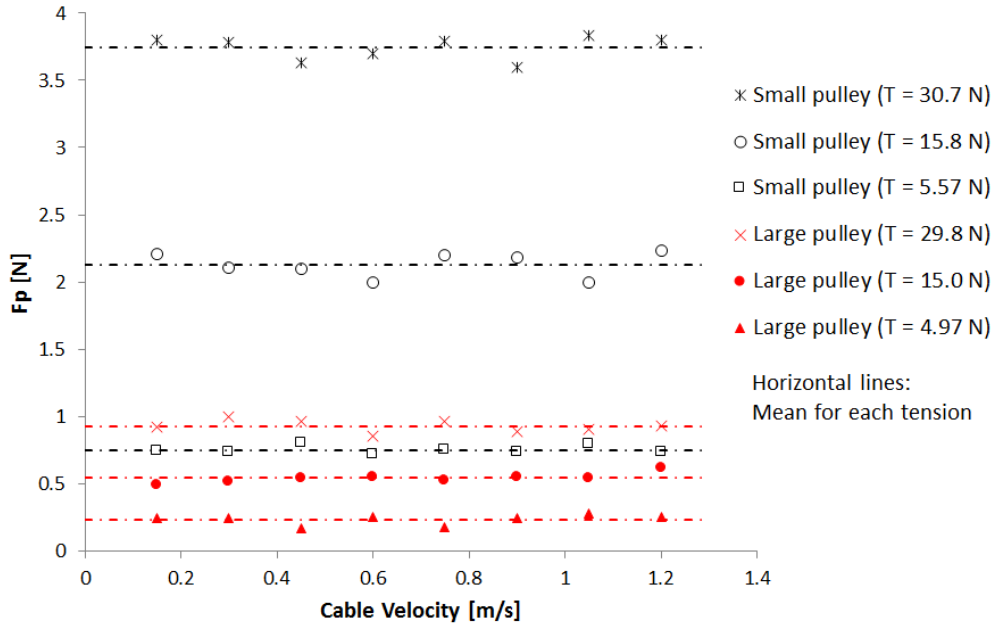


Figure 2.5: Cable-pulley friction against cable velocity for setups with 9 small and large pulleys at three different tensions. $\theta_{w,i,av}$ is roughly 85° for both pulleys.

Fig. 2.4 and 2.5, change in the frictional force as a function of velocity is not observed from the results with different number of pulley. Now that we are not able to observe the linear increase of cable-pulley friction as the cable velocity increases in all the experiments, it is concluded that the viscous term can be excluded from cable-pulley friction for all pulley sizes.

### *2.3.2 Gravity Driven System*

*Setup*

Coulomb friction due to cable-pulley interaction was measured using a gravity driven setup (Fig. 8) with a model fitting method. Due to absence of the motor and noise associated with it, the measured value was considered to be more accurate than the motor driven system. The system measures linear displacement of cable from angular displacement measured by

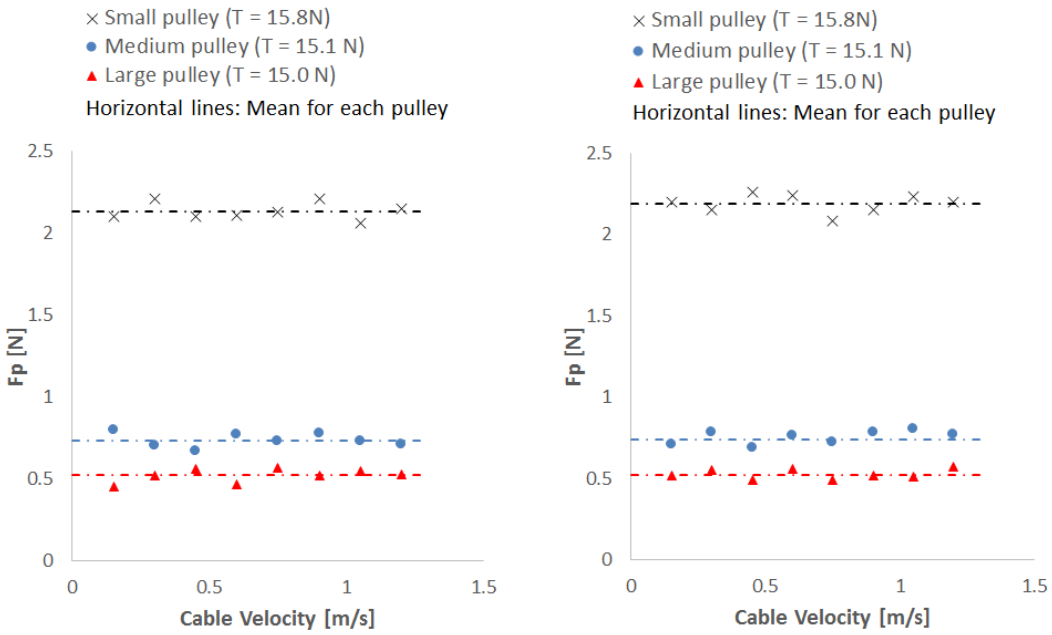


(a) $\theta_{w,i,av} = 50°$ (b) $\theta_{w,i,av} = 135°$

Figure 2.6: Cable-pulley friction against cable velocity for setups with 9 small, medium and large pulleys respectively when $\theta_{w,i,av}$ = (a)50° and (b)135°.

magnets placed radially on a pulley which pass by a Hall Effect sensor. Tension was dictated by identical loads on the ends of the cable. Motion was induced by a weight added to one side of the cable. An Arduino Uno chip was used for I/O, which enable sufficiently accurate measurement of the displacement of each mass by means of the Hall effect sensor on either end. The effective distance between the magnets was 9.8 mm. A time differential of the Hall effect data was used to estimate cable velocity at either end. To ensure the assumption of high stiffness in the cable, Hall Effect sensors were embedded on both ends of the setup and only the trials where the displacement graphs were identical were used.

*Model*

The system can be modeled as shown in Fig. 2.9 and with a mathematical expression in state space form in (3), which includes the cable stiffness, damping, and cable-pulley friction

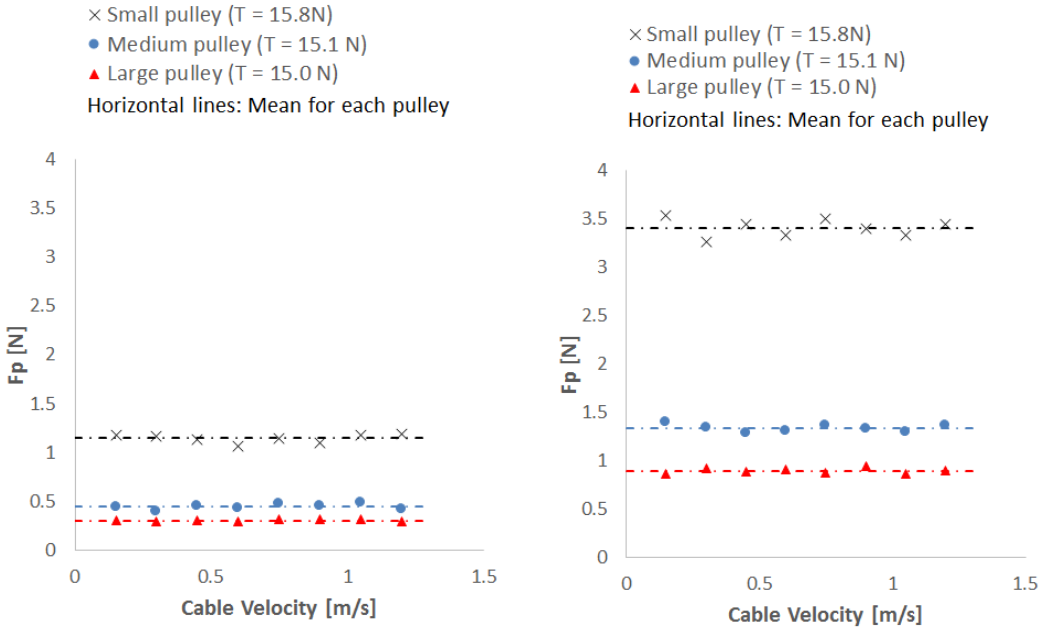


(a) $n_p = 5$ (b) $n_p = 15$

Figure 2.7: Cable-pulley friction against cable velocity for setups with (a)5 and (b)15 small, medium and large pulleys.

terms. Since the cable translates only in one direction and force applied on the cable is consistent, there is no effect of hysteresis, and the stiffness and damping forces used here are simply linear to the displacement and velocity, respectively, and are represented in the model by $k$ and $b$. The gravitational constant is represented by $g$.

$$\begin{bmatrix} \dot{x}_1 \\ \ddot{x}_1 \\ \dot{x}_2 \\ \ddot{x}_2 \end{bmatrix} = \begin{bmatrix} 0 & 1 & 0 & 0 \\ \frac{-k}{m_1} & \frac{-b-\frac{f_v}{4}}{m_1} & \frac{k}{m_1} & \frac{b-\frac{f_v}{4}}{m_1} \\ 0 & 0 & 0 & 1 \\ \frac{k}{m_2} & \frac{b-\frac{f_v}{4}}{m_2} & \frac{-k}{m_2} & \frac{-b-\frac{f_v}{4}}{m_2} \end{bmatrix} \begin{bmatrix} x_1 \\ \dot{x}_1 \\ x_2 \\ \dot{x}_2 \end{bmatrix} + \begin{bmatrix} 0 \\ m_2 g - \frac{f_c}{2} \\ 0 \\ -m_2 g - \frac{f_c}{2} \end{bmatrix} \tag{2.3}$$

The model is numerically solved using 4th order Runge Kutta method. In order to search for parameters that lead to the best correlation, a least square method is used and from the average of several trials, parameters which result in the highest correlations are calculated.

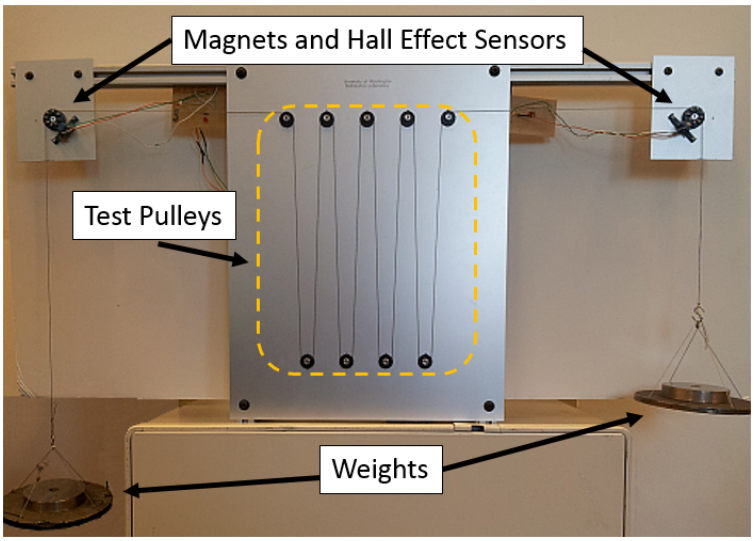


Figure 2.8: Gravity driven pulley board. Pulleys instrumented with magnets and Hall Effect sensors which are connected to Arduino microcontroller at the back of the board.

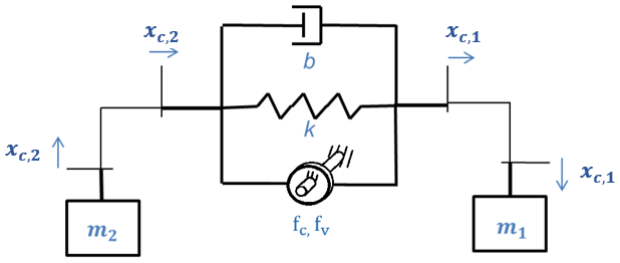


Figure 2.9: Schematic model of the gravity driven pulley board.

For most of the trials, data show very high correlation, often with an $R^2$ value of more than 0.95. The model can be simplified as in Fig. 2.10 and (4) due to the fact that the tension is held nearly constant because the masses applied are very similar and are given initial conditions so that the cable does not vibrate and the effect of cable stiffness and damping becomes negligible. This was confirmed by fitting the models in (3) and (4) to the data obtained from the pulley setup with 9 medium pulleys and $\theta_{w,i,av}$ of 85° at nominal cable tension of 15.5 N. The value for $f_c$ for the two different model formulations of equations (3)

and (4) are identified to be 0.816 and 0.818 N respectively. The plots of those models as well as the experimental data are shown in Fig. 2.11.

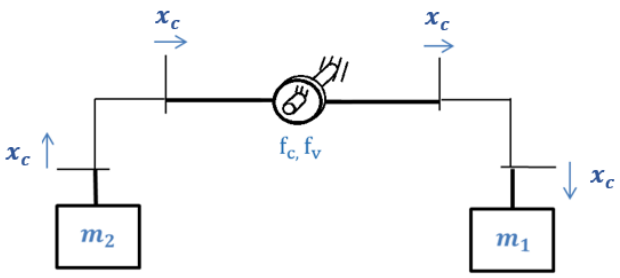


Figure 2.10: Simplified schematic model of the gravity driven pulley board.

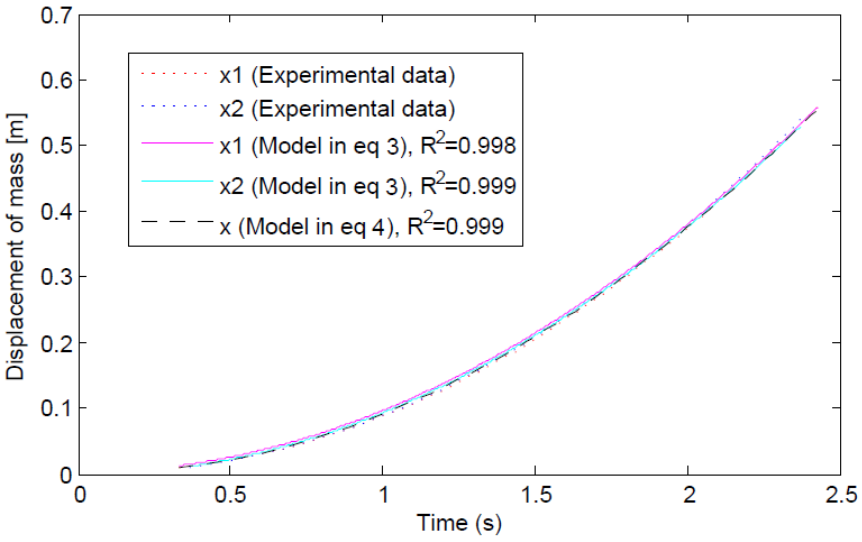


Figure 2.11: Comparison of original and simplified models of the gravity driven pulley board with experimental data.

$$\begin{bmatrix} \dot{x} \\ \ddot{x} \end{bmatrix} = \begin{bmatrix} 0 & 1 \\ 0 & -\frac{f_v}{m_1+m_2} \end{bmatrix} \begin{bmatrix} x \\ \dot{x} \end{bmatrix} + \begin{bmatrix} 0 \\ \frac{(m_1-m_2)g-f_c}{m_1+m_2} \end{bmatrix} \tag{2.4}$$

Furthermore, since the pulley friction is not a function of cable velocity per the previous

section, the pulley friction simply becomes Coulomb friction, and the model can be reduced to (5). This series of simplifications is just for the purpose of Coulomb friction identification and is not for characterizing the dynamics of cable driven systems.

$$\begin{bmatrix} \dot{x} \\ \ddot{x} \end{bmatrix} = \begin{bmatrix} 0 & 1 \\ 0 & 0 \end{bmatrix} \begin{bmatrix} x \\ \dot{x} \end{bmatrix} + \begin{bmatrix} 0 \\ \frac{(m_1 - m_2)g - f_c}{m_1 + m_2} \end{bmatrix} \tag{2.5}$$

*Measurements and results*

First, $\theta_{w,i,av}$ was set to be a constant value. Here, $\theta_{w,i,av}$ can be any constant as long as it is within the range of interest. We selected a value of 85° and tested the effect of tension for the $f_c$ value by conducting trials with system configurations consisting of 5, 9, 15, and 19 pulleys to simultaneously test if $f_c$ could be a function of number of pulleys in the system.

For each pulley size $f_c$ is plotted individually as a function of tension (Fig. 2.12). Each line in the plot represents data for a board setup with a different number of pulleys. Without exception, $f_c$ linearly correlates with cable tension with $R^2$ more than 0.99 and the slope and y-intercept become larger as the number of pulleys increases.

From this observation, the slope or $\partial f_c / \partial T$ when $\theta_{w,i,av} = 85°$ is plotted with respect to number of pulley in Fig. 2.13 as well as the y-intercepts (values of $f_c$ when $\theta_{w,i,av} = 85°$ and $T = 0$). As a result, we identified

$$\frac{\partial f_c(\theta_{w,i,av} = 85°)}{\partial T} = c_1 n_p \tag{2.6}$$

$$f_c(\theta_{w,i,av} = 85°, T = 0) = c_2 n_p \tag{2.7}$$

Integrating (6) with respect to T yields

$$f_c(\theta_{w,i,av} = 85°) = n_p(c_1 T + c_2) \tag{2.8}$$

The values of $c_1$ and $c_2$ are summarized in Table 2.1.

We then investigated how $\theta_{w,i,av}$ affects to $f_c$. To begin with, $f_c$ is plotted against $\theta_{w,i,av}$ with combinations of three different tensions and three number of pulleys, showing total of

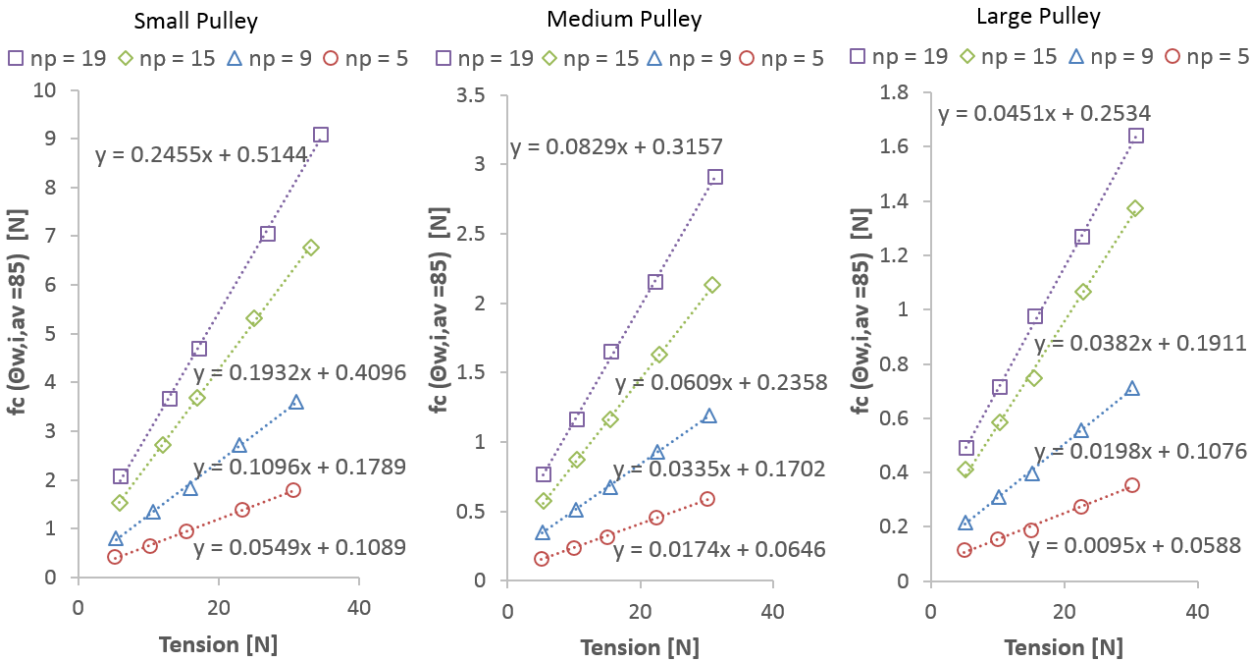


Figure 2.12: $f_c$ ($\theta_{w,i,av} = 85°$) against tension for small, medium, and large pulley (from left to right). Each line indicates the linear fit to the data for 5, 9, 15, and 19 pulleys respectively.

9 data sets for each pulley size (Fig. 2.14). Most of the data sets demonstrate high linearity and the slopes $\partial f_c/\partial\theta_{w,i,av}$ appear to increase for higher tension and more pulleys. Acting on that trend, $\partial f_c/\partial\theta_{w,i,av}$ was plotted with respect to $n_p$ (Fig. 2.15). Then, as linear functions represent the trends of data points with high correlation, the slopes $\partial^2 f_c/(\partial\theta_{w,i,av}\partial n_p)$ are plotted as a function of tension (Fig. 2.16).

From the trend lines in Fig. 2.16, we obtained

$$\frac{\partial^2 f_c}{\partial\theta_{w,i,av}\partial n_p} = c_3 T \tag{2.9}$$

and the trend lines in Fig. 2.15 give

$$\frac{\partial f_c(n_p = 0)}{\partial\theta_{w,i,av}} = 0 \tag{2.10}$$

Then, integration of (2.9) with respect to $n_p$ results

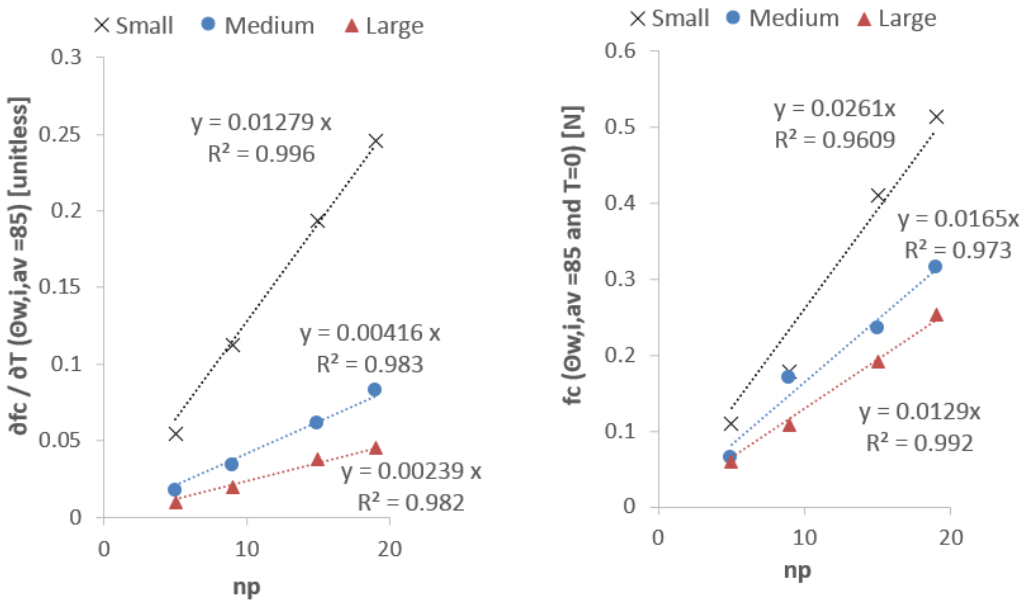


(a) (b)

Figure 2.13: (a) Partial derivative of $f_c$ ($\theta_{w,i,av} = 85°$) with respect to tension and (b) $f_c$ ($\theta_{w,i,av} = 85°$, $T = 0$) against number of pulley. Linear trend lines for each pulley size are shown.

$$\frac{\partial f_c}{\partial \theta_{w,i,av}} = c_3 T n_p \tag{2.11}$$

By integrating with respect to $\theta_{w,i,av}$, (2.11) becomes

$$f_c = c_3 T n_p \theta_{w,i,av} + f(n_p, T) \tag{2.12}$$

where $f(n_p, T)$ is the constant of integration which is a function of $n_p$ and $T$. When $\theta_{w,i,av} = 85°$, this equation becomes

$$f_c(\theta_{w,i,av} = 85°) = c_3 n_p T 85° + f(n_p, T) \tag{2.13}$$

Since (2.13) and (2.8) are equivalent, we get

$$f(n_p, T) = n_p(c_1 T + c_2) - c_3 n_p T 85° \tag{2.14}$$

By substituting (2.14) into (2.12), we obtain the expression of $f_c$ as a function of $T$, $\theta_{w,i,av}$, and $n_p$ as follows.

$$f_c = n_p((c_1 + c_3(\theta_{w,i,av} - 85^\circ))T + c_2) \tag{2.15}$$

In section 2.3.1, we concluded there is no viscous friction and hence (2.2) is written as

$$\begin{aligned} F_p &= f_c[T, n_p, \theta_{w,i,av}]sign(\dot{x}) \\ &= n_p((c_1+c_3(\theta_{w,i,av}-85^\circ))T+c_2)sign(\dot{x}) \end{aligned} \tag{2.16}$$

The values of $c_1$, $c_2$, and $c_3$ for each pulley are summarized in Table 2.1. Note that (2.16) with coefficients in Table 2.1 is valid under the range of variables we examined in the experiments which is shown in Table 2.2 with similar cable and pulleys employed for the RAVEN II system.

Table 2.1: Summary of coefficients

| Pulley size | Radius | $c_1$ | $c_2$ | $c_3$ |
|---|---|---|---|---|
| | $[mm]$ | $[unitless]$ | $[N]$ | $[1/degree]$ |
| Small | 3.80 | 0.0128 | 0.0261 | $2.79\times10^{-5}$ |
| Medium | 7.82 | 0.00416 | 0.0165 | $1.02\times10^{-5}$ |
| Large | 11.45 | 0.00239 | 0.0129 | $0.737\times10^{-5}$ |

## *2.4 Discussions*

Viscous friction, the dependency of the cable-pulley friction force on magnitude of cable velocity, was not observed for any of the pulleys and tensions tested. The fact that not only section 2.3.1 showed the velocity independence, but also the data from section 2.3.2

Table 2.2: Range of variables in which the model is valid

| Variable | Range |
|---|---|
| $\dot{x}$ | up to 1.3 [m/s] |
| $T$ | up to 33 [N] |
| $n_p$ | up to 19 |
| $\theta_{w,i}$ | 15° to 180° |
| $\theta_{w,i,av}$ | 45° to 150° |

demonstrated high correlation without viscous friction indicated the viscous term can be excluded from the cable-pulley friction model. The result might vary if the cable was running at a much higher velocity, but the range of velocities we studied was in the range of actual robot operation.

In the case of Coulomb friction, we confirmed that it was a function of $T$, $\theta_{w,i,av}$, and $n_p$. When the friction model is solely Coulomb friction, the mean values in the plots of the motor driven experiment in section 2.3.1 represents $f_c$ and those values should be equivalent to the results from the gravity driven experiments in section 2.3.2. Indeed, $f_c$ values calculated based on (2.16) were very close to those found in Fig. 2.4 to 2.7 with most within 5% and a maximum error of about 10%. The error can mainly be associated with the motor current reading since the signal needs to be filtered out due to presence of high noise which affects more for the larger load or tension. However, since we derived the model based on the gravity driven pulley board, the model was not affected by that uncertainty. One related source of error would be the approximation of tension using the nominal value. Furthermore, friction can vary depending on the degree of lubrication, wear and oxidation of each pulley and surrounding conditions such as temperature and humidity.

### *2.5 Conclusions*

We have determined the cable-pulley friction model as a function of cable tension, average individual wrap angle, and type and number of pulleys employed. The derived equation and coefficients can be applied to any cable-driven systems as long as they are operated within the presented conditions and parameters and use cable and pulleys similar to the ones employed for the RAVEN II system (e.g. cable: type 304 stainless steel, 7 strand and 19 wire construction, 0.61 mm diameter. pulley: 6061 Aluminum with hard anodized finish, rolling element bearing).

If the presented cable-pulley friction model is used with an accurate cable stretch model, the accuracy and robustness of the control can be potentially improved, which is necessary for automation of surgical tasks. This is under active pursuit.

The proposed model requires the knowledge of the real time cable tension. Although one can integrate force sensors into systems, it would be costly and complicate the systems. Another method is to calculate tension from a cable stretch model, but the initial tension needs to be known. Even though it is possible to measure initial tension using a tension gauge, measurement has to be taken every time the system is started. However, this step can be simplified with the cable tension estimation method presented in [40]. Hence, we plan on implementing the proposed cable pulley friction model with a cable stretch model and the initial tension estimation technique for the RAVEN II.

The characteristic of stretch and the bending radius are not the same for different cable types. How cables are constructed (number and diameter of fiber composition) and how materials (e.g. alloy and grade of steel) behave under certain stretch and bending conditions makes a difference in the interaction between the cable and pulley. Therefore, the cable-pulley friction model may depend on the type of the cable and further inspection is required.

The cables used in these experiments were new. As the cable experiences wear and creep over time and the condition of cable-pulley interaction changes, this could also affect the friction values. Knowing how the cables react to repeated use and aging could help better

predict how they respond to future operation, and one could adjust the friction model to account for this.

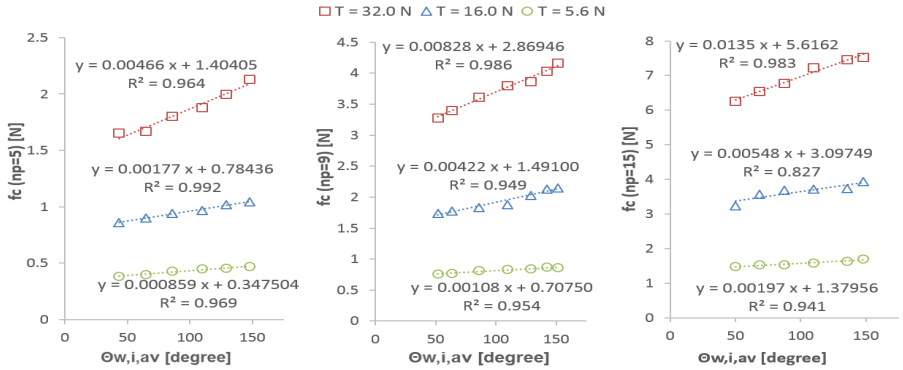


(a) Small Pulley

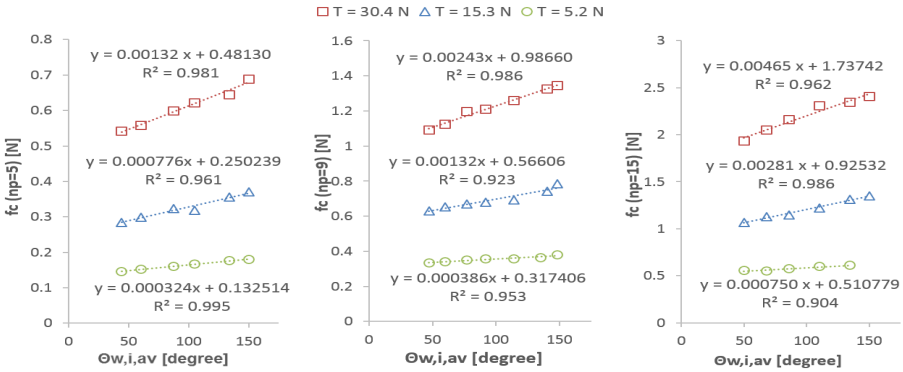


(b) Medium Pulley

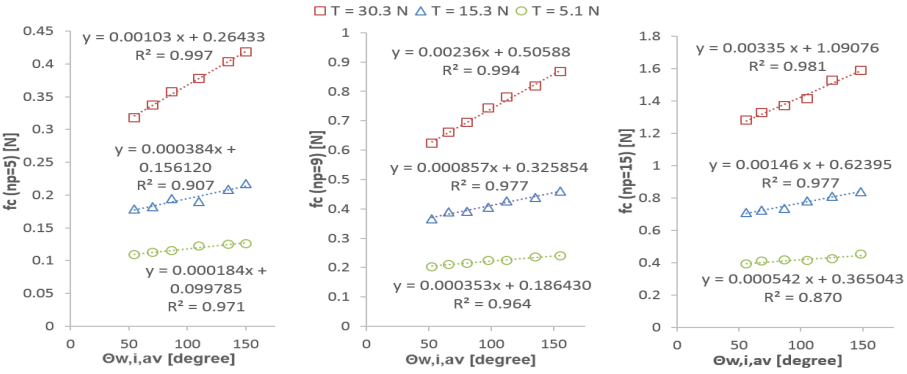


(c) Large Pulley

Figure 2.14: $f_c$ when $n_p = 5$, 9, and 15 (from left to right) against $\theta_{w,i,av}$ for (a) small, (b) medium, and (c) large pulley. Each line shows the linear fit to the data for different constant tension.

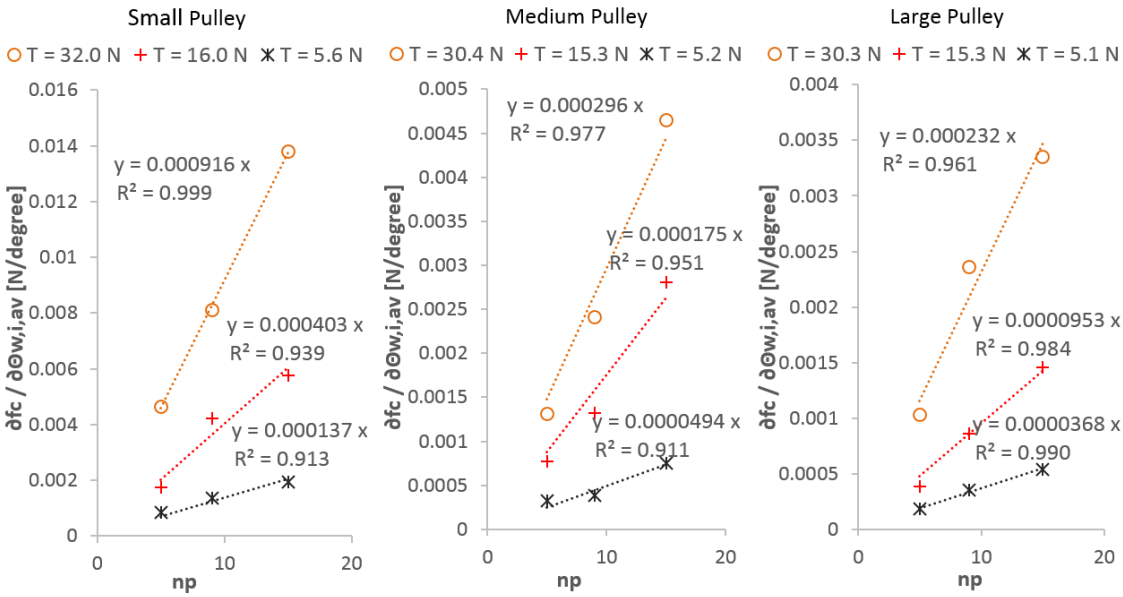


Figure 2.15: Partial derivative of $f_c$ with respect to $\theta_{w,i,av}$ against number of pulley for small, medium, and large pulley (from left to right). Linear trend lines for different tensions are shown.

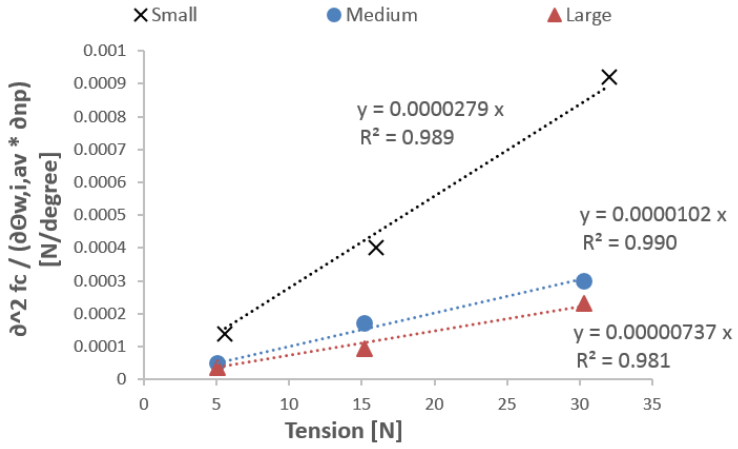


Figure 2.16: $\partial^2 f_c/(\partial\theta_{w,i,av}\partial n_p)$ against tension. Linear trend lines for different pulley size are shown.

# Chapter 3

# HYSTERETIC CABLE STRETCH

## *3.1 Introduction*

When actuating cable driven systems such as the RAVEN II surgical robotic research platform [29] consisting of serial links, cable is repeatedly stretched and relaxed longitudinally. Automation of such systems with high accuracy is not easily achieved due to the complicated response of cable. One approach to improve automation accuracy of such system is development of better control systems often with feedback of system's state using external observation. However, for design and control analysis, development of an accurate model becomes quite important.

The significance of using a hysteresis model for modeling cable is that it eliminates the discrepancy of cable stretch force between loading and unloading phases which could introduce control inaccuracy. Moreover, a hysteresis model is able to capture the rate independent energy loss due to inter-wire sliding friction and plastic deformation of material, and the information of the energy loss can be used for fatigue life prediction.

Spak et al. [77] review past and recent development of helically twisted cable models which can be categorized into thin rod models, semicontinuous models, and beam models. They also investigate three major categories of internal damping mechanisms; damping due to friction between the individual wires, changes in the cable geometry and properties, and internal friction within the wires and they are modeled as interwire friction, variable bending stiffness, and internal damping or hysteretic terms respectively. Sauter [71] uses the Masing model [53] and modeled the cable as a whole instead of considering the individual wires to capture hysteretic behavior of stockbridge dampers.

The Bouc-Wen hysteresis model [7] [85], a special form of the Duhem model [19], treats

the cable from a macro level and is used to describe various non-linear hysteretic systems because it is capable of generating various shapes of hysteretic loops in analytical form [76]. The Bouc-Wen model has been applied to systems with the hysteresis behaviors such as the tendon-sheath mechanism and wire rope vibration isolators [17], [60], [72]. Even though those models are not directly used for the RAVEN II system in which cables are longitudinally stretched, those researches indicate that the Bouc-Wen model can be applicable.

The contribution of this chapter is development of a longitudinally stretched cable model consisting of a rate independent hysteresis model and linear damper that can be applied for control of cable driven mechanisms. The rate independent hysteresis model was developed based on quasi-static cyclic loading tests in section 3.2 and the rate dependent term was obtained from longitudinal vibration tests in section 3.3. The hysteresis model parameters for the cables employed for the RAVEN II system are optimized using the genetic algorithm.

## *3.2 Cyclic Loading Test*

A cyclic loading test was performed in order to obtain the rate independent hysteresis loop. We plot the results with applied load instead of stress as y-axis because the test result is unique for the type of cable construction (i.e. number of strands and number of wires in each strand) and it cannot be generalized based on total cross sectional area. Strain was used as x-axis since the result can be extended to characterize cables with different lengths. We employed two sizes of cables, thin and thick, which are actually used in the RAVEN II system. Both cables consist of 7 twisted strands and each strand is formed by 19 individual wires made out of type 304 stainless steel. The diameter of thin and thick cables are 0.61 mm and 1.19 mm and the breaking strengths are approximately 200 N and 1100 N respectively. All the tested cables were 0.8 m long. The test setup and cable used are shown in Fig. 3.1. The load applied was decided based on the loading condition for the RAVEN II system which is roughly up to 160 N.

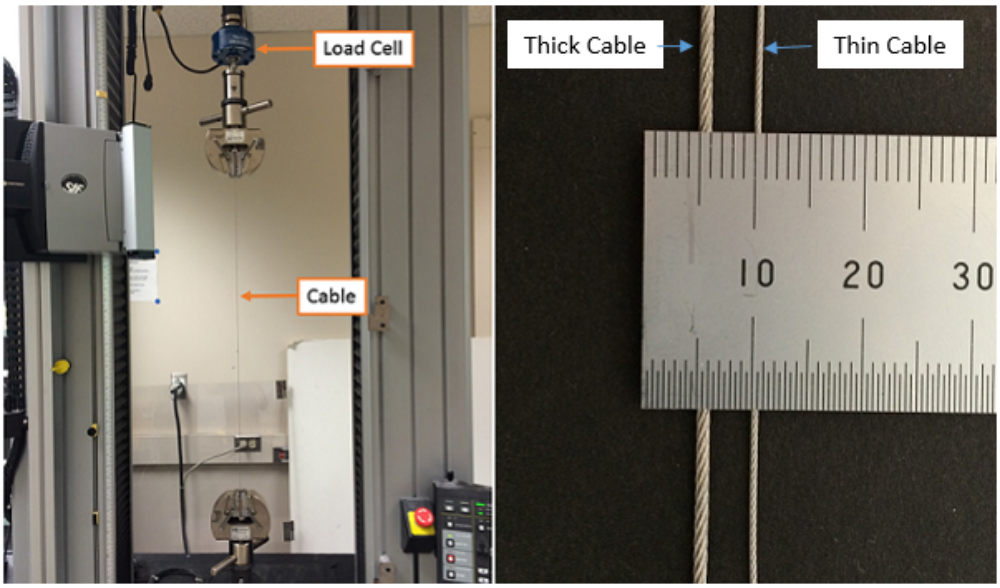


Figure 3.1: Instron cyclic loading test bench and the thin and thick cables used for the experiments.

### *3.2.1 Preconditioning*

For the initial cyclic loading test, force controlled cycles of 0 to 200 N were applied 25 times continuously to the samples of fresh cable. This process is necessary for avoiding permanent stretch that occurs when cables are loaded for the first time. The load was applied slowly at the rate of 0.15 mm/s (strain rate of $1.875\times10^{-4}$). Fig. 3.2 shows that strain does not return to where the cycle started and the curve keeps shifting to the right. The amount of the shift for each cycle becomes smaller as the cable undergoes more cycles and the it is observed to be converging. The shift is more obvious for the thin cable than thick cable most likely due to the fact the load applied is close to the breaking strength for the thin cable.

### *3.2.2 Quasi-Static Hysteresis Loop*

The cable was quasi-statically stretched at the rate of 0.05 to 0.1 mm/s (strain rate of $0.625\times10^{-4}$ to $1.25\times10^{-4}$) to identify the response that is independent of the magnitude of

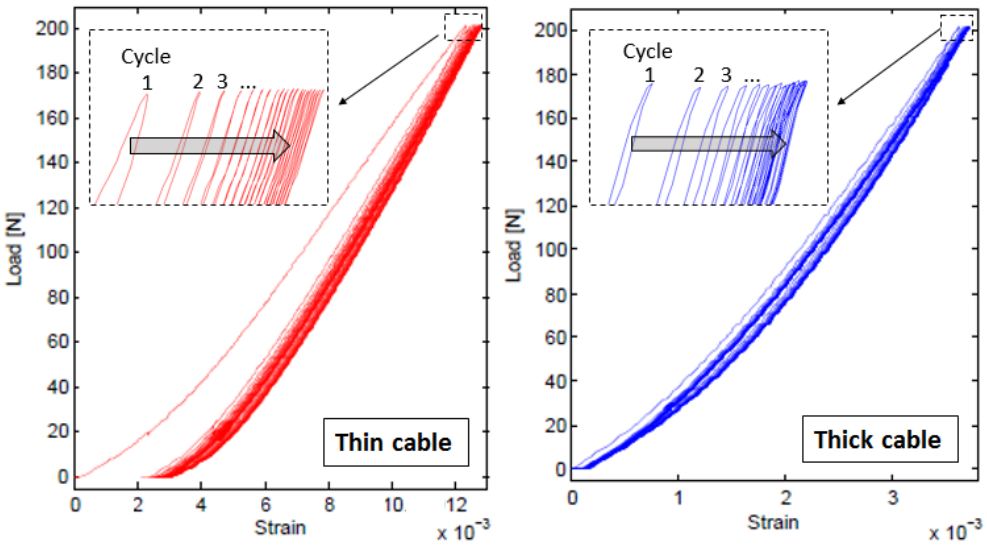


Figure 3.2: Cyclic loading for prestretching. (Force controlled, 25 cycles of 0-200[N])

velocity. The cycle was position controlled and strain cycles of 0 to $3.75\times10^{-3}$, $6.35\times10^{-3}$, $8.75\times10^{-3}$ were applied for thin cable and cycles of 0 to $1.25\times10^{-3}$, $2.5\times10^{-3}$, $3.75\times10^{-3}$ were applied for thick cable (Fig. 3.3). The unloading path is always under the loading path which means energy is dissipated in every cycle.

### *3.2.3 Proposed Model*

The original Bouc-Wen model is modified to make it follow the trend of experimental data. We propose shape control functions (6.6) which represents a non-linear elastic stiffness and (6.26) which modulates the symmetric hysteretic loop. When developing a model, only positive longitudinal stretch is considered because cable becomes slack and cannot be compressed as negative displacement is applied. Then, the proposed hysteresis model $F_h$ which consists of 9 parameters is represented as follows.

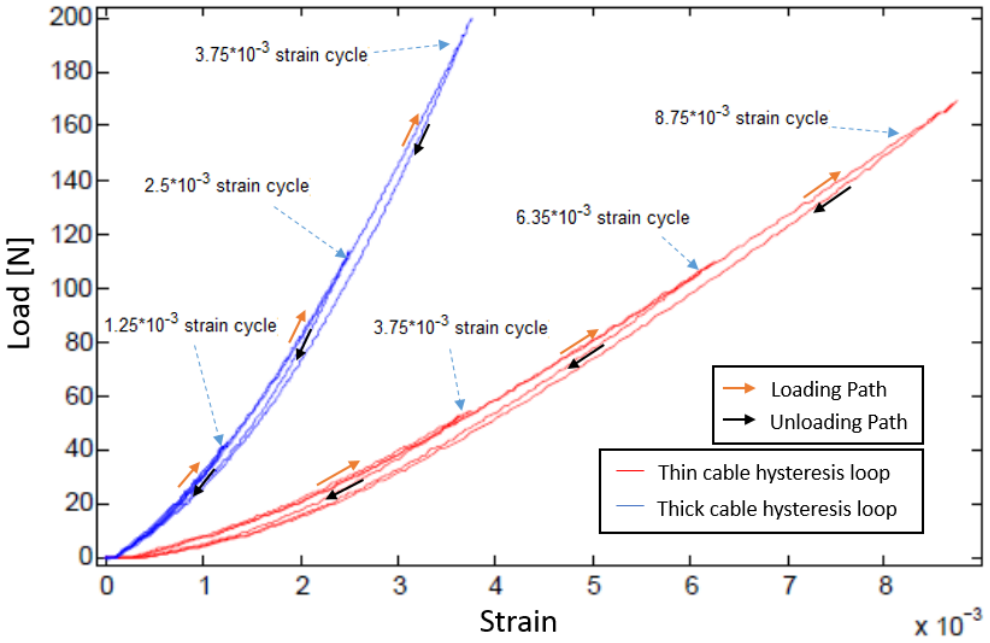


Figure 3.3: Hysteresis loops for the thin and thick cables. (Position controlled, applied strain cycles are 0 to $3.75\times10^{-3}$, $6.35\times10^{-3}$, $8.75\times10^{-3}$ for thin cable and cycle of 0 to $1.25\times10^{-3}$, $2.5\times10^{-3}$, $3.75\times10^{-3}$ for thick cable)

$$F_h(x_s(t), \dot{x}_s(t), z(t)) = \begin{cases} 0 & : x_s(t) < 0 \\ f_1(x_s(t)) + f_2(x_s(t))z(t) & : x_s(t) \geq 0 \end{cases} \tag{3.1}$$

$$f_1(x_s(t)) = k_1 x_s(t) - \frac{k_2 x_s(t)}{k_3 x_s(t)^2 + 1} \tag{3.2}$$

$$f_2(x_s(t)) = k_4 x_s(t)^m \tag{3.3}$$

$$\dot{z}(t) = \dot{x}_s(t)[\alpha - [\gamma + \beta sgn(\dot{x}_s(t)z(t))]\,|z(t)|^n] \tag{3.4}$$

where $x_s(t)$ is the cable strain and $z(t)$ is the hysteretic variable. Parameters to be identified are $k_1$, $k_2$, $k_3$, $k_4$, $\alpha$, $\beta$, $\gamma$, $m$, and $n$. Since the proposed model is a modified version of the

Bouc-Wen model, the proposed model should be derivable from the Duhem operator [83] which possesses the two criteria of hysteresis; rate independence and memory effect. The Duhem operator forms a Cauchy problem with the output function $F_h$ with any differentiable input function $x_s$ and any initial value $F_h^0$.

$$\begin{cases} \dot{F}_h = g_1(x_s, F_h)\dot{x}_s^+ - g_2(x_s, F_h)\dot{x}_s^- \\ F_h(t=0) = F_h^0 \end{cases} \tag{3.5}$$

where $\dot{x}_s^+ := (|\dot{x}_s| + \dot{x}_s)/2$, $\dot{x}_s^- := (|\dot{x}_s| - \dot{x}_s)/2$, and $g_1(x_s, F_h)$ and $g_2(x_s, F_h)$ are the functions describing ascending and descending part of the hysteresis loop respectively. This equation (3.5) only holds for positive time increment in order to assure irreversibility, one of the important features of hysteresis.

For $x_s \geq 0$, differentiating (3.1) with respect to time yields

$$\dot{F}_h = k_1\dot{x}_s + \frac{k_2\dot{x}_s}{k_3x_s^2+1} - \frac{2k_2k_3x_s^2\dot{x}_s}{(k_3x_s^2+1)^2} + k_4mx_s^{m-1}\dot{x}_s z + k_4x_s^m\dot{z} \tag{3.6}$$

Here, $\dot{z} = dz/dx_s\ \dot{x}$. $z$ and $dz/dx_s$ are substituted by the equations obtained from rearranging (3.1) and (3.4) respectively. Then, the proposed equation can be written as

$$\dot{F}_h = \left\{ f_3 + k_4x_s^m\left[\alpha - \left[\gamma + \beta sgn\left(\frac{\dot{x}_s(F_h - f_1)}{f_2}\right)\right]\left|\frac{F_h - f_1}{f_2}\right|^n\right]\right\}\dot{x}_s \tag{3.7}$$

where

$$f_3 = k_1 + \frac{k_2}{k_3x_s^2+1} - \frac{2k_2k_3x_s^2}{(k_3x_s^2+1)^2} + k_4mx_s^{m-1}\frac{F_h - f_1}{f_2}$$

We now select $g_1(x_s, F_h)$ and $g_2(x_s, F_h)$ as

$$g_1(x_s, F_h) = f_3 + k_4x_s^m\left[\alpha - \left[\gamma + \beta sgn\left(\frac{F_h - f_1}{f_2}\right)\right]\left|\frac{F_h - f_1}{f_2}\right|^n\right] \tag{3.8}$$

$$g_2(x_s, F_h) = f_3 + k_4x_s^m\left[\alpha - \left[\gamma - \beta sgn\left(\frac{F_h - f_1}{f_2}\right)\right]\left|\frac{F_h - f_1}{f_2}\right|^n\right] \tag{3.9}$$

Then,

$$
\begin{aligned}
& g_1(x_s, F_h)\dot{x}_s^+ - g_2(x_s, F_h)\dot{x}_s^- = \\
& \qquad |\dot{x}_s|\left[k_4 x_s^m \beta sgn\left(\frac{F_h - f_1}{f_2}\right)\left|\frac{F_h - f_1}{f_2}\right|^n\right] \\
& \qquad\qquad +\dot{x}_s\left[f_3 + k_4 x_s^m\left(\alpha - \gamma\left|\frac{F_h - f_1}{f_2}\right|^n\right)\right] \\
& = \left\{f_3 + k_4 x_s^m\left[\alpha - \left[\gamma + \beta sgn\left(\frac{\dot{x}_s(F_h - f_1)}{f_2}\right)\right]\left|\frac{F_h - f_1}{f_2}\right|^n\right]\right\}\dot{x}_s
\end{aligned}
\tag{3.10}
$$

Hence, the proposed model can be represented in a form of the Duhem operator with prescribing functions $g_1(x_s, F_h)$ and $g_2(x_s, F_h)$ as in (3.8) and (3.9).

### *3.2.4 Parameter Identification with Genetic Algorithm*

The genetic algorithm (GA) [31] was employed for identification of the parameters of the proposed hysteresis model. The GA stocastically generates sets of parameters (population) from a pre-defined solution domain. Each set of parameters (individual) is evaluated based on a specified fitness function. The more fit individuals are used to form the population for the next generation based on selection methods such as crossover, mutation, and reproduction. This process is repeated until the generation reaches a pre-set number or an ideal fitness value is achieved. Because of its evaluation method, the GA is suitable for identification of the proposed hysteresis model having a large number of parameters and possibly possessing multiple local optima. We used the crossover selection method and the evaluation was continued until a pre-set number of generations were produced. The objective is to find model parameters which minimize the fitness function defined below.

$$
F_{fitness} = \sum_{j=1}^{N_d}(F_{model,j} - F_{exp,j})^2 \tag{3.11}
$$

where $N_d$ is the total number of data points and j is the index of data point. $F_{model}$ is the hysteresis model solved with different input strain cycles and $F_{exp}$ is the corresponding cyclic loading test data from experiments. We ran the algorithm several times and selected the

Table 3.1: Bouc-Wen model coefficients for thin and thick cables

| Cable Dia. | $\alpha$ | $\beta$ | $\gamma$ | $n$ | $m$ | $k_1$ | $k_2$ | $k_3$ | $k_4$ |
|---|---|---|---|---|---|---|---|---|---|
| Thin (0.61 mm) | 1.13 | 58.0 | 193 | 0.766 | 0.380 | 21400 | 14300 | 57000 | 38600 |
| Thick (1.19 mm) | 1.80 | 113 | 101 | 0.718 | 0.460 | 70100 | 44000 | 97000 | 82000 |

best fit result. The identified parameters are summarized in Table 3.1. The hysteresis model with optimized parameters are plotted with the experimental results in Fig. 3.4.

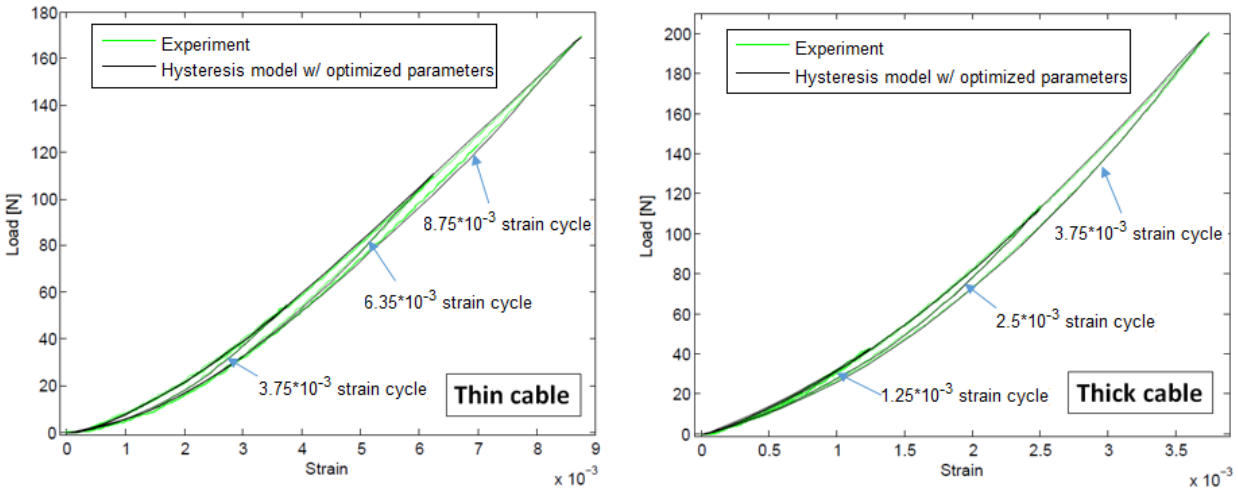


Figure 3.4: Cable hysteresis model with GA identified parameters vs. experimental data. Results with three different strain cycles are shown.

### *3.3 Longitudinal Vibration Test*

The motivation of this test is to investigate the dynamic response of the proposed hysteresis model and further develop the cable model which possibly lacks a rate dependent term. The setup is shown in Fig. 3.5. Cables were preconditioned by applying cycles of load higher than the maximum load applied during the vibration test. The guide pole and pulleys were placed to avoid excitation of non-longitudinal vibration modes. Positions of the guide pulleys were

adjusted so that their surfaces stay without pressing against the guide pole and minimize frictional interference. The Keyence IL-030 and Arduino UNO were used for displacement measurements and data acquisition. The IL-030 has measurement range of 25 mm and repeatability of 1 $\mu m$. We applied 3.99 kg weight for the thin cable and 19.35 kg for the thick cable. The weights were chosen so that the vibration amplitude becomes large enough for consistent data acquisition. To start longitudinal vibration, the weight was lifted up from the equilibrium position and released with zero initial velocity. The data were collected at 1000 Hz.

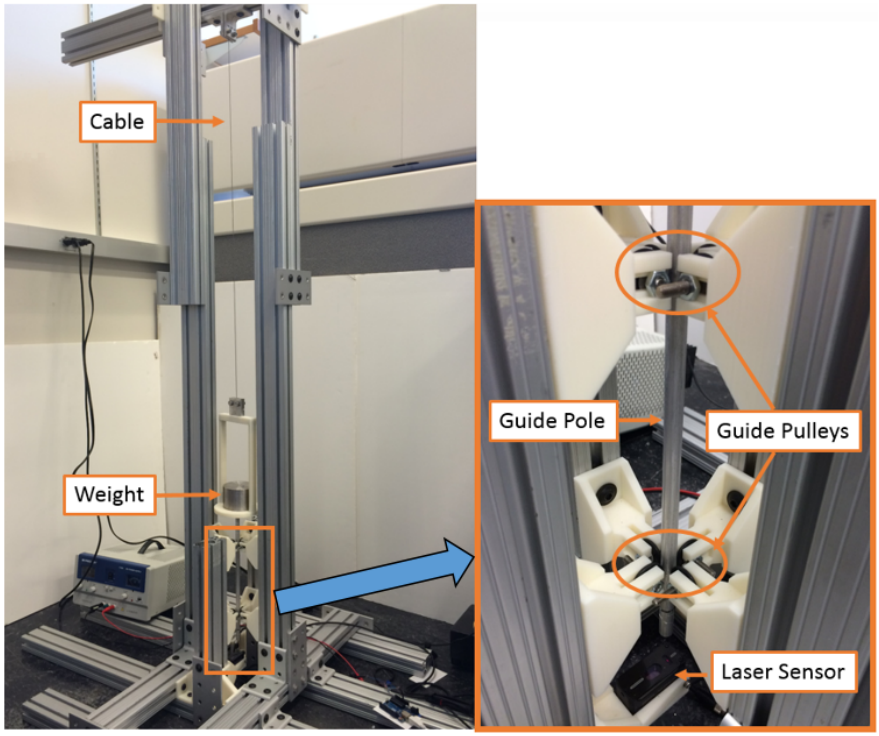


Figure 3.5: Longitudinal vibration test setup.

### *3.3.1 Hysteresis Model vs Non-hysteresis Model*

The equation of motion of the system with the hysteresis model is represented in state space form (3.12). The state variables are $x_1 = x(t)$, $x_2 = \dot{x}(t)$, and $x_3 = z(t)$. $x(t)$ is the cable

stretch and $\dot{x}(t)$ is the rate of cable stretch.

$$\begin{bmatrix} \dot{x}_1 \\ \dot{x}_2 \\ \dot{x}_3 \end{bmatrix} = \begin{bmatrix} x_2 \\ \frac{1}{M}(Mg - F_h(x_{s1}, x_{s2}, x_3)) \\ x_{s2}[\alpha - [\gamma + \beta sgn(x_{s2}x_3)]\,|x_3|^n] \end{bmatrix} \tag{3.12}$$

where $x_{s1} = \frac{x_1}{l_0}$, $x_{s2} = \frac{x_2}{l_0}$, $l_0$ is the free length of the cable, $M$ is the mass of the weight, $g$ is the gravitational constant. Although the vibration was constrained, the cable still vibrated laterally. However, only negligibly small longitudinal vibration (less than 1% of the longitudinal displacement during the experiment) was observed when the cable was plucked and lateral vibration was introduced. Therefore, the effect of the lateral vibration was ignored.

For comparison with the hysteresis model, we developed a non-hysteresis model ($F_{nh}$) which is the non-linear elastic stiffness term $f_1$ 6.6 with different set of parameters $k_{1,nh}$, $k_{2,nh}$, and $k_{3,nh}$.

$$F_{nh}(x_s(t)) = k_{1,nh}x_s(t) - \frac{k_{2,nh}x_s(t)}{k_{3,nh}x_s(t)^2 + 1} \tag{3.13}$$

The parameters were adjusted by trial and error so that the function passed through the middle of the loading and unloading paths of the hysteresis loop. The parameters found were $k_{1,nh}$=24720, $k_{2,nh}$=19380, and $k_{3,nh}$=57000 for the thin cable and are $k_{1,nh}$=71500, $k_{2,nh}$=55000, and $k_{3,nh}$=126100 for the thick cables. The state space form of the non-hysteresis model is in (3.14). All models were solved numerically and the time step size was set to be roughly $10^{-6}$ [s] in order to reduce numerical error.

$$\begin{bmatrix} \dot{x}_1 \\ \dot{x}_2 \end{bmatrix} = \begin{bmatrix} x_2 \\ \frac{1}{M}(Mg - F_{nh}(x_{s1})) \end{bmatrix} \tag{3.14}$$

The experimental measurements of longitudinal vibration and the hysteresis and non-hysteresis models for thin and thick cables are shown in Fig. 3.6. The vibration of the

hysteresis model decays due to hysteretic energy loss whereas the non-hysteresis model exhibits no energy loss as expected. However, both models require additional non-conservative force models in order to capture the decay of the experimental data.

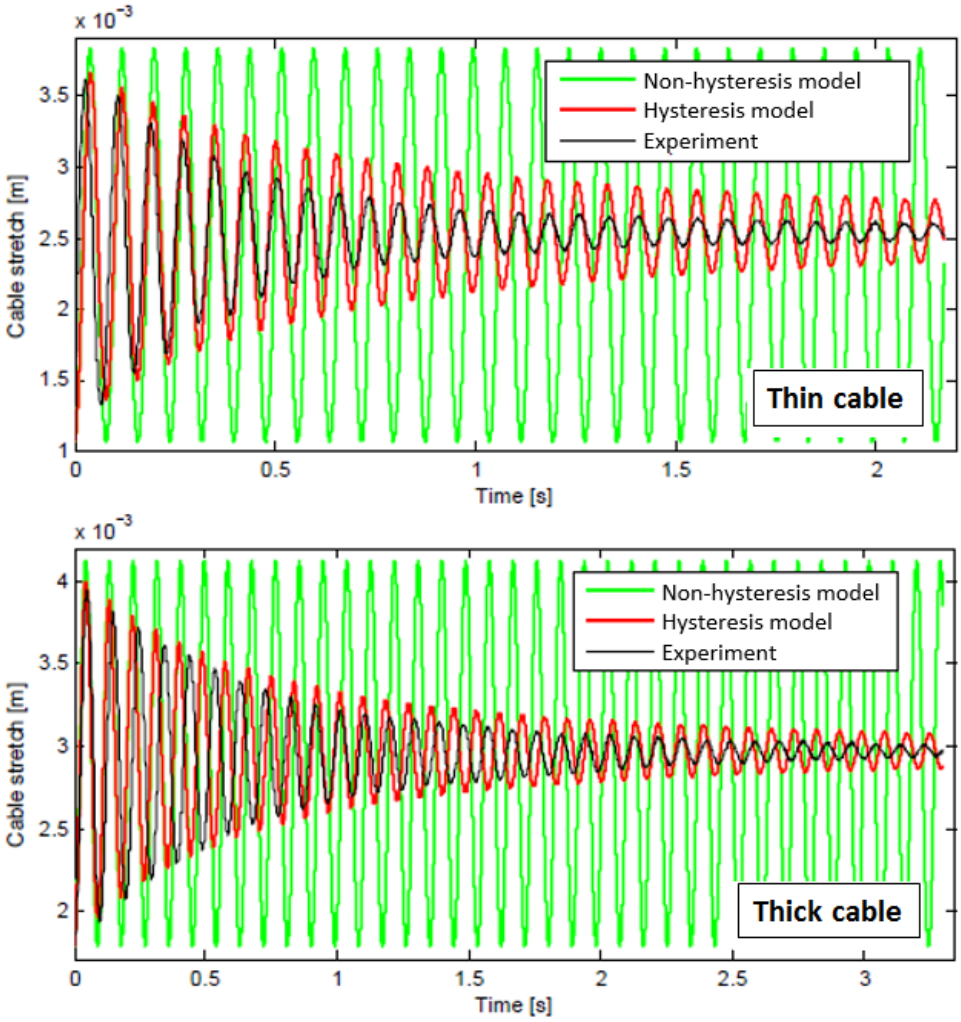


Figure 3.6: Hysteresis and non-hysteresis models for thin and thick cables and experimental data during the longitudinal vibration test.

### *3.3.2 A Model with Linear Damper*

Linear damper was added to both hysteresis and non-hysteresis models and their coefficients are denoted $c_{d,h}$ and $c_{d,nh}$ respectively (3.15, 3.16). The coefficients that minimize root mean square at peaks and troughs are identified and the values are shown in Table 3.2. When calculating peak and trough errors, all data are aligned vertically to eliminate bias from different steady state values. Then, the new equations of motions become (3.12) with $F_h$ replaced by $F_H$ for the hysteresis model and (3.14) with $F_{nh}$ replaced by $F_{NH}$ for the non-hysteresis model.

$$F_H(x_s(t), \dot{x}_s(t), z(t)) = F_h(x_s(t), \dot{x}_s(t), z(t)) + c_{d,h}\dot{x}_s(t) \tag{3.15}$$

$$F_{NH}(x_s(t), \dot{x}_s(t)) = F_{nh}(x_s(t)) + c_{d,nh}\dot{x}_s(t) \tag{3.16}$$

Those coefficients found are specifically for 0.8 m long cable. In order to generalize the coefficient for any length of cable, the relation between the value of coefficient and the cable length needs to be checked.

Table 3.2: Optimized linear damping coefficients for 0.8 m cables.

| | Thin cable | Thick cable |
|---|---|---|
| $c_{d,h}[Ns]$ | 7.06 | 15.72 |
| $c_{d,nh}[Ns]$ | 12.20 | 38.81 |

For both cable sizes, longitudinal vibration test results for both hysteresis and non-hysteresis models with linear damper showed that the lack of energy dissipation is corrected (Fig. 3.7). Decay of the amplitudes for both models and the experimental data (Fig. 3.8)

shows that the hysteresis model correlates with the experimental data better. The performances of the models were compared to the experimental data based on three values; frequency, steady state (SS) stretch, and logarithmic decrement. Logarithmic decrement ($\delta$) is defined as

$$\delta = \frac{1}{n_p} ln \frac{x_{p,k}}{x_{p,k+n_p}} \tag{3.17}$$

where $n_p$ is the number of successive peaks and $x_{p,k}$ is the amplitude at $k$th peak. Here, we chose $k$=1 and $n_p$ is the number of the total peaks observed during the experiment. Frequency, SS stretch, and log decrement and each percent error with respect to the experimental data for thin and thick cables are summarized in Table 3.3 and Table 3.4. For the thin cable, the frequency of the hysteresis model was closer to the experimentally obtained value but the non-hysteresis model had only 2.5 % error. As for the SS stretch, both models were very close to the experimental result. The hysteresis model had about 6 % logarithmic decrement error whereas the non-hysteresis model showed about 30 % error. The thick cable exhibited 0.3 % SS stretch and logarithmic decrement error was smaller for the hysteresis model. Although the frequency error for the hysteresis model was larger compared to the non-hysteresis model, both errors were less than 10 %. The experiments for both cable sizes showed that the vibration attenuated quickly when the amplitude was large but as the amplitude became smaller, the rate of attenuation became smaller. This behavior was well captured by the hysteresis model with linear damper.

### *3.3.3 Energy Dissipation*

There are two main mechanisms of energy dissipation when stretching cable; inter-wire sliding friction and internal material solid friction, and both frictions have components of Coulomb and viscous friction. The Coulomb portion of inter-wire sliding friction and internal solid friction is included in the hysteresis term and the viscous portion is represented by the linear damping term. Energy dissipation due to non-conservative linear damping force is simply

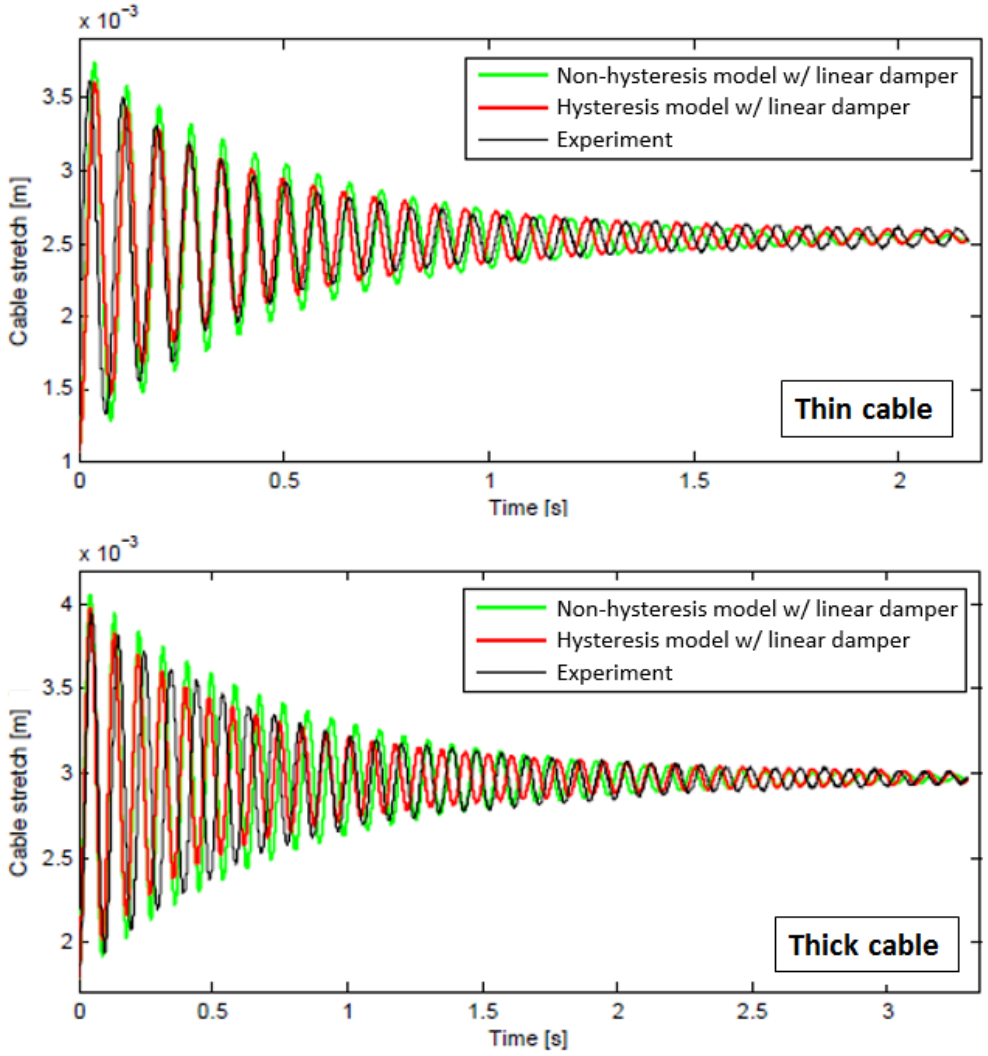


Figure 3.7: Hysteresis and non-hysteresis models with linear damper for thin and thick cables and experimental data during the longitudinal vibration test.

integration of the force over the distance the force is applied.

$$W_d = \int_{x_{start}}^{x_{end}} F_d dx \tag{3.18}$$

where $F_d$ is $c_{d,h}\dot{x}$ for the hysteresis model and $c_{d,nh}\dot{x}$ for the non-hysteresis model, and $x_{start}$ and $x_{end}$ are the start and end position of the vibration. The damping force $F_d$ for both models and cable types were plotted against the cable stretch (Fig. 3.9). As the system

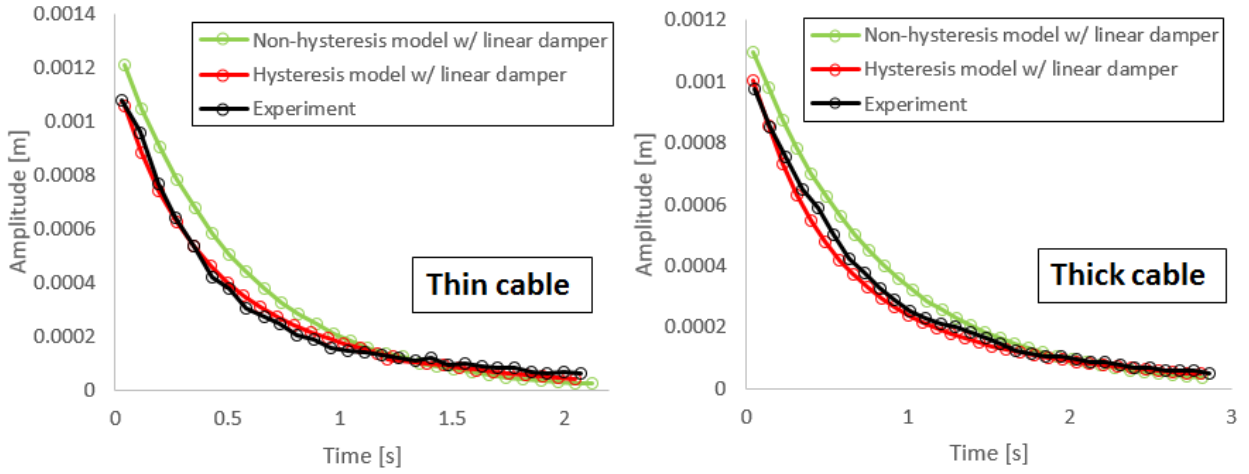


Figure 3.8: Amplitude of hysteresis and non-hysteresis models with linear damper and experimental data during the longitudinal vibration test.

oscillates up and down while attenuating, the damping forces draw spirals and it is clear that the area enclosed by the damping model for non-hysteresis model is more than that for hysteresis model.

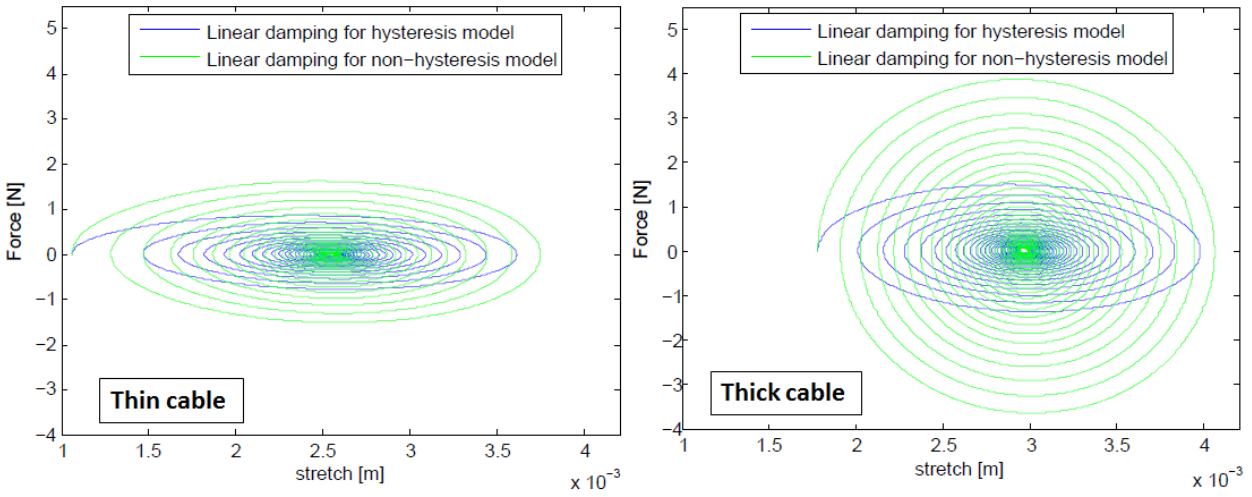


Figure 3.9: Linear damping force during the longitudinal vibration test plotted against cable stretch.

Table 3.3: Performance of hysteresis and non-hysteresis models during the longitudinal vibration test. (Thin cable)

| | Experiment | Hysteresis model | Non-hysteresis model |
|---|---|---|---|
| Frequency [Hz] | 13.281 | 13.448 | 12.940 |
| SS stretch [m] | $2.544\times10^{-3}$ | $2.549\times10^{-3}$ | $2.536\times10^{-3}$ |
| Log decrement, $\delta$ | 0.115 | 0.118 | 0.145 |
| Frequency % err | - | 1.263 | 2.566 |
| SS stretch % err | - | 0.177 | 0.314 |
| Log decrement % err | - | 6.046 | 30.145 |

The hysteretic force model is partially elastic (conservative) and partially non-conservative. If cycles make completed loops, energy loss is

$$W_h = \oint_{x_{start}}^{x_{end}} F_h dx \tag{3.19}$$

which is the enclosed area inside the hysteresis loop. However, when cable is randomly loaded and the cycles are not closed, which is the case for robot actuation cables, the energy loss is calculated by the summation of partially enclosed area for all the cycles as shown in Fig. 3.10 and 3.11. The integration of each cycle starts at a point on the loading path ($x_{start,i}$ where $i$ is the index of cycle) which has the same stretch as the point of next trough. Then, the point of next trough is the ending point of integration ($x_{trough,i}$). $N$ is the total number of cycles. As the amplitude of the cycle becomes smaller, the hysteresis loop becomes narrower and the energy loss gets smaller.

$$W_h = \sum_{i=1}^{N} W_{h,i}, \quad W_{h,i} = \int_{x_{start,i}}^{x_{trough,i}} F_h dx \tag{3.20}$$

Table 3.4: Performance of hysteresis and non-hysteresis models during the longitudinal vibration test. (Thick cable)

| | Experiment | Hysteresis model | Non-hysteresis model |
|---|---|---|---|
| Frequency [Hz] | 10.658 | 11.584 | 11.188 |
| SS stretch [m] | $2.969\times10^{-3}$ | $2.973\times10^{-3}$ | $2.966\times10^{-3}$ |
| Log decrement, $\delta$ | 0.100 | 0.097 | 0.111 |
| Frequency % err | - | 8.692 | 4.969 |
| SS stretch % err | - | 0.135 | 0.101 |
| Log decrement % err | - | 2.938 | 10.750 |

To confirm numerical simulation accuracy, the change in the energy between initial and last states of the vibration was calculated. The change in the gravitational potential energy, elastic potential energy, and kinetic energy are denoted $\Delta PE_G$, $\Delta PE_E$, and $\Delta KE$ respectively. The gravitational potential energy and kinetic energy can be calculated accurately from the initial and last conditions of the system. However, to calculate the elastic potential energy for the hysteresis model, the unplotted portion of the unloading path needs to be integrated with respect to stretch. Since figuring out the path requires extra calculation, this step was simplified by approximating the unplotted unloading path using the non-hysteresis model $F_{nh}$.

The energy dissipation due to the hysteresis and linear damping terms and the change in the system's potential and kinetic energies are summarized in Table 3.5. Energy dissipation by the non-hysteresis model's linear damping terms agrees very well with the change in the system's total energy for both cable sizes. Theoretically, the total energy dissipation should completely be equal to the change in the system's total energy. However, numerical error from the differential equation solver causes a slight disagreement. For the hysteresis model

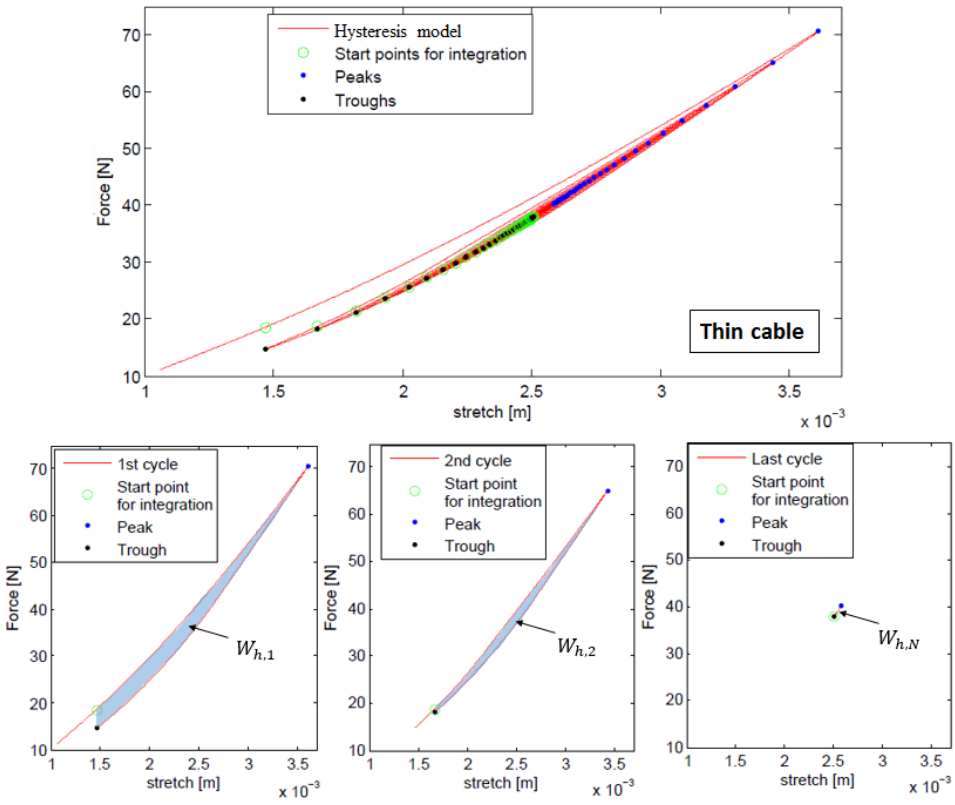


Figure 3.10: Hysteretic force during the longitudinal vibration test for thin cable. Energy loss for the 1st, 2nd, and the last cycles are shown.

of thin cable, about 57% of energy was lost by the hysteresis term and for the thick cable, the hysteretic energy loss was roughly 71%. Although the agreement between the calculated total energy dissipation and the change in the system's energy was worse for hysteresis models for both cables, the largest error was about 1%. One possible source of error is the approximation of elastic potential energy mentioned earlier. Also, looking into the fact that the energy dissipation captured by the hysteresis term is caused by the Coulomb portion of inter-cable and internal cable frictions, energy should be dissipated in both loading and unloading phases. Thus, the employed calculation method of energy dissipation for the hysteresis term could cause additional error.

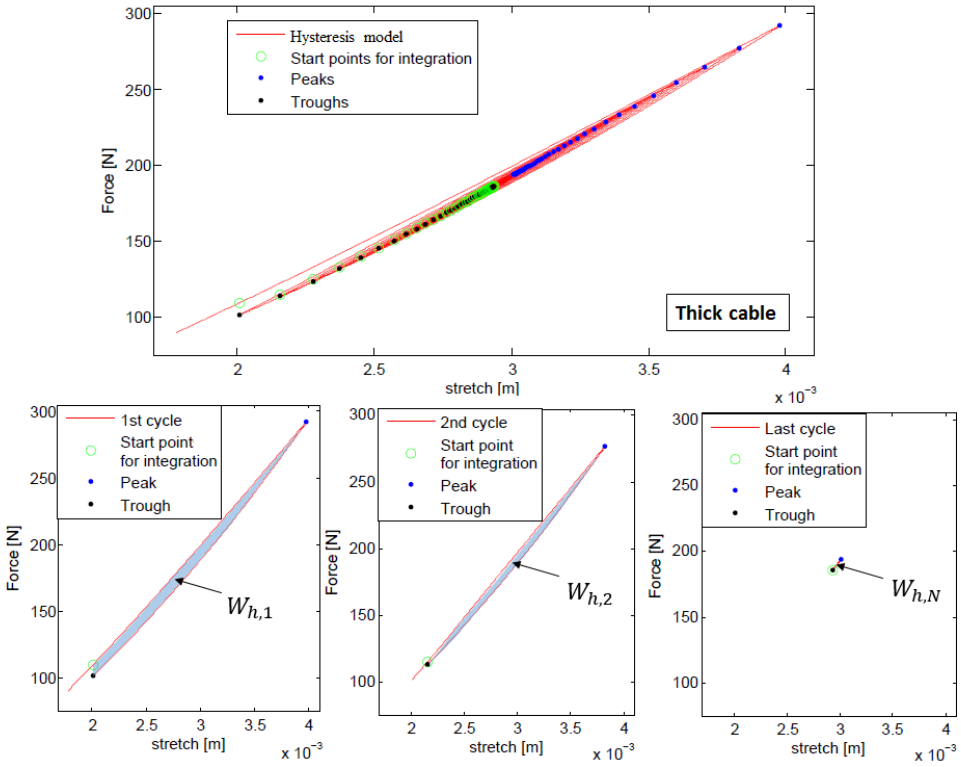


Figure 3.11: Hysteretic force during the longitudinal vibration test for thick cable. Energy loss for the 1st, 2nd, and the last cycles are shown

## *3.4 Conclusions*

We developed the hysteresis model for longitudinally loaded cables that can be applied for control of cable driven mechanisms. The model consists of a rate independent hysteresis term and rate dependent linear damper. Using the proposed hysteresis model, parameters for two cables with different diameters employed in the RAVEN II system were identified. The cables used are type 304 stainless cable with construction of 7 strands and 19 wires. However, the model can potentially represent cables with different construction and diameter. Even though the linear damping coefficients were only proved to work for the length of the cable tested in the experiments, the coefficients can be generalizable by performing further experiments and finding relationships between the coefficient and the cable geometry.

Table 3.5: Energy dissipation and change in the system's energy

| | Thin cable | | Thick cable | |
|---|---|---|---|---|
| | Hysteresis model | Non-hysteresis model | Hysteresis model | Non-hysteresis model |
| $W_h$ $[J]$ | 0.01381 | - | 0.04579 | - |
| $W_d$ $[J]$ | 0.01040 | 0.02447 | 0.01898 | 0.06494 |
| $W_{total}$ $[J]$ | **0.02421** | **0.02447** | **0.06477** | **0.06494** |
| $\Delta PE_G$ $[J]$ | -0.05751 | -0.05695 | -0.22539 | -0.22205 |
| $\Delta PE_E$ $[J]$ | 0.03303 | 0.03248 | 0.16043 | 0.15710 |
| $\Delta KE$ $[J]$ | 0.00002 | 0 | 0.00006 | 0 |
| $\lvert\Delta E_{total}\rvert$ $[J]$ | **0.02446** | **0.02447** | **0.06490** | **0.06495** |
| Difference $[J]$ | **0.00025** | **0** | **0.00013** | **0.00001** |
| % error | **1.022** | **0** | **0.200** | **0.015** |

One unique feature of the hysteresis model is that it captures energy dissipation that is independent of the cable stretch rate. The hysteresis model, together with a linear damper demonstrated high correlation to experimentally obtained data in terms of vibration frequency, steady state stretch, and logarithmic decrement. The attenuation of amplitude with time was captured better compared to non-hysteresis model.

The dynamic model of the RAVEN II system is planned to be developed by combining the proposed cable stretch model and the cable pulley interaction friction model developed in [57]. Besides, the developed RAVEN II model will be used with state estimation technique as described in [26] for added control accuracy and robustness. Furthermore, the energy loss calculated from integration of the hysteresis model can be utilized for prediction of fatigue life if a proper computational algorithm is employed.

The cables used for both quasi-static cyclic loading test and longitudinal vibration test were originally fresh before they were preconditioned. Since the model parameters were optimized for that cable condition, the parameters may require to be adjusted after long time use. Besides, as the performance of the cable could also be affected by temperature and humidity of the surrounding environment as well as corrosion, further experiment needs to be carried out for fine tuning of the parameters.

# Chapter 4

# MODELING THE RAVEN II

## *4.1 Introduction*

Cable or wire rope is a mechanical transmission method often employed due to advantages such as transmission of power over some distance and limited space, adaptability to mechanical geometries with use of guide pulleys, zero backlash, compliance, and low inertia for serial link robots because motors can be mounted off the joints. However, when it is applied to robotic systems, a kinematic model is not sufficient for accurate control because the cable has some elasticity and internal friction and the friction from cable and pulley interaction varies dynamically.

Generally, cables consist of multiple strands of wires helically surrounding a center core strand. Under stress, each strand and wire slide while overcoming inter strand and wire friction and as a result, exhibits complex hysteretic response. The discrepancy of cable stretch force between loading and unloading phases caused by the hysteresis could introduce control inaccuracy. The motion or sliding of the pulley occurs inside the pulley bearing rather than at the contact surface of cable and pulley. This is because the bearing is generally well lubricated and the coefficient of friction at the bearing is lower than that of cable and pulley interface. Slippage at the cable and pulley interface can be ignored especially when the speed of cable translation is not high (i.e. for robot arm actuation) and the inertia of pulley is low. The effect from the pulley bearing friction could be significant for robot control since the friction could be very high as cable tension increases. The cable pulley friction is also complex since multiple variables could affect the amount of friction including cable tension, wrap angle of cable around pulley, number of pulley employed, and cable velocity.

To improve the accuracy, one can employ extra sensors and track position, velocity, and

acceleration of the end-effector or force transmitted by cable. However, adding sensors is costly and mounting sensors and extra wiring complicates the system. For some systems like surgical robots and instruments, adding sensors is not possible space-wise and not practical due to the sterilization requirement.

Townsend [79] analyzes tension element (cable, belt, etc.) drives using a linear stiffness model and investigate open-loop bandwidth of a manipulator. Mitsantisuk et al. [55] propose a control method for a wire-based twin direct-drive motor system with variable tension based on a linear spring model. The control requires encoders on both motors and accelerator at the moving platform. Caverly et al. [10] present state estimation of a similar single Degree of Freedom (DOF) system with a linear stiffness model. The algorithm uses the Extended Kalman Filter (EKF) and Unscented Kalman Filter (UKF) based on the information from an accelerator on the payload and encoders from one or both winches. Reiter et al. [67] fuse robot kinematics and 3D visual observations using the EKF to detect and track a surgical tools of the da Vinci Surgical robot. Abdollahi et al. [2] present control method that use no a priori knowledge of the system dynamics by utilizing a neural network with motor position and velocity measurements.

Another approach to solve the accuracy problem is using a simple and inaccurate model and estimate the model parameters. Chen et al. [14] present a calibration method using a kinematic model with flexibility compensation and improve the track accuracy of a humanoid-arm manipulator. The algorithm uses an error model between the measured state and the model output. Wernholt et al. [86] estimate parameters of a non-linear model based on frequency response functions which is linearized and evaluated at a set of operation points. There are some previous researches performed to improve the accuracy of the RAVEN II surgical robotic system. Edward et al. [59] develop a dynamic model of a single DOF cable drive test bench and apply the UKF to estimate the state and model parameters. The parameter estimation is performed offline using information from motor and joint encoder. In that research, a simple exponential cable stiffness model and Coulomb and viscous friction model are used. Ramadurai et al. [65] perform a simulation of one of the actual RAVEN II

joint using the same cable model. Haghighipanah et al. [26] extend the work and apply the technique for the first 3 joints of the RAVEN II. Mahler et al. [51] use a kinematic model and estimated the model parameters with Gaussian Process Regression. The pose and velocity of the RAVEN II which are necessary for the estimation are tracked using a motion capture system that uses LED markers.

Our approach is to accurately model the dynamics of the cable system so that the model can be applied in replacement of the model used in our prior work and some aforementioned simple models. This approach is lower cost and the system will be less complicated because it requires no extra sensors. Moreover, this method has potential to realize more accurate and robust control compared to using a simple model. In addition, this method is able to capture information of how much and where force/torque are used and the input energy is dissipated by the inter-wire sliding friction and plastic deformation of material. Such information can be used for system analysis such as contact and grasping force estimation and cable fatigue life prediction. Hence, development of an accurate dynamic model has such potential and can be quite meaningful.

We employ the RAVEN II surgical robotic research platform developed by the University of Washington's BioRobotics Lab for the proposed model verification. The system uses cable drives for all 7 DOFs in order to realize easy sterilization and eliminate dynamic effect from the motor weight and has a workspace with two rotational and one prismatic joints. The remaining 4 DOF are used for driving surgical instruments. The system currently incorporates a kinematic model and the inputs are the joint positions measured by optical encoders embedded in the motors. A kinematic model is sufficient when the robot is primarily used for tele-operation where the operator can visually adjust the robot position. However, when it comes to automation/semi-automation, the kinematic model is not accurate enough because of the issues with cable drives.

The major contribution of this chapter is development of a detailed model of cable driven mechanisms with closed circuit cable/pulley transmissions [75]. The model consists of the previously developed models in chapters 3 and 2 and the details of the model are described

in section 4.2. The model performance is evaluated and discussed in section **??**. Even though the model in section 4.2 is developed based on the RAVEN II, the model can be transferred to any closed circuit cable/pulley transmission systems that have structure, load, cable tension, and cable and pulley parameters similar to the RAVEN II.

## *4.2 Raven II System Dynamics*

### *4.2.1 Previous Dynamic Model*

The entire picture of the RAVEN II is shown in Fig. 4.1. Each DOF uses a closed circuit cable configuration as in Fig.4.2. Previously, the dynamic model of the RAVEN II was constructed follows.

$$\ddot{q}_j = I_j^{-1}(\Gamma - F_L(q_j, \dot{q}_j)) \tag{4.1}$$

$$F_L = F_C + F_G + F_l + J^T F_{en} \tag{4.2}$$

$$F_l = f_{c,j} sgn(\dot{q}_j) + f_{v,j}\dot{q}_j \tag{4.3}$$

$$\Gamma = (T_{j,1} - T_{j,2}) r_j \tag{4.4}$$

where $q_j$, $\dot{q}_j$, $\ddot{q}_j$ are the angular position, velocity, and acceleration of joint respectively. The radius of motor capstan and joint are denoted $r_{mc}$ and $r_j$. $I_j$ is joint inertia matrix, $F_C$ and $F_G$ are the torques from Coriolis and gravitational effect, $J$ and $F_{en}$ are Jacobian and external torque, $f_{c,j}$ and $f_{v,j}$ are coefficients of Coulomb and viscous friction for the joints, and $T_{mc,1}$, $T_{mc,2}$, $T_{j,1}$, and $T_{j,2}$ are the lower and upper cable tensions for the motor capstan side and robot joint side. $F_C$ and $F_G$ are calculated from inverse dynamics of the linkages. The formulation and descriptions for the joint dynamics (eq. (4.1) to (4.4)) are for rotational joints. Therefore, for prismatic joints, all the corresponding terms should be changed accordingly. Also, there exist an effect called cable coupling which is the interdependence of different joint angles [26].

Also, the exponential cable stretch and linear damper were used for modeling the cable

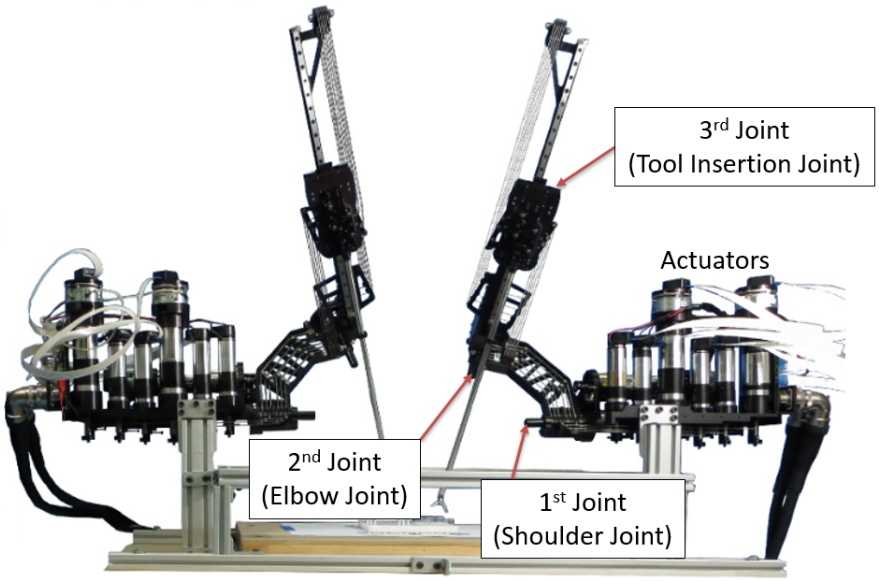


Figure 4.1: The RAVEN II surgical robotic research platform

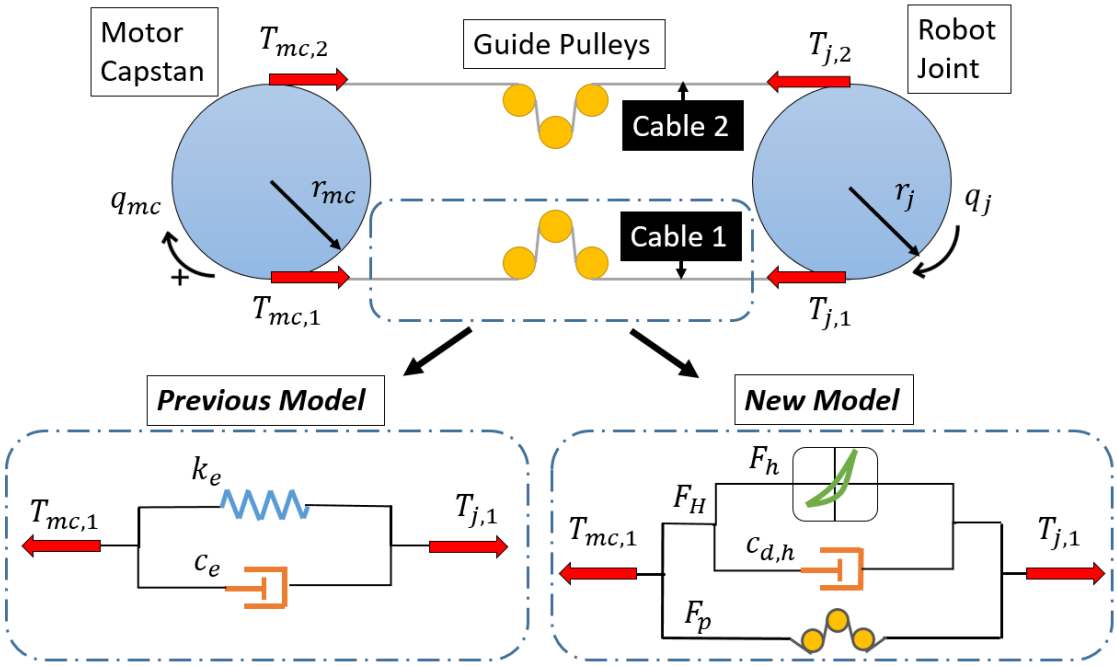


Figure 4.2: Schematic drawing of 1 DOF Raven II cable drive system with guide pulleys.

tension.

$$T_{j,1} = k_e(e^{q_{mc}r_{mc}-q_j r_j}) + c_e(\dot{q}_{mc}r_{mc} - \dot{q}_j r_j) \tag{4.5}$$

$$T_{j,2} = k_e(e^{q_j r_j - q_{mc}r_{mc}}) - c_e(\dot{q}_{mc}r_{mc} - \dot{q}_j r_j) \tag{4.6}$$

where $q_{mc}$, $\dot{q}_{mc}$ are the angular position and velocity of motor capstan. $k_e$ and $c_e$ are the stiffness and damping coefficients for the stiffness and damping respectively. For the previous model, $T_{mc,i} = T_{j,i}$ (i = 1, 2) because the cable pulley friction was lumped into the joint friction.

### *4.2.2 New Dynamic Model*

The fundamental robot's dynamics (eq. (4.1) to (4.4) with cable coupling) remains the same. The exponential cable stretch model is replaced with the hysteresis model $F_H$ (eq. (3.15)) proposed in chapter 3. Moreover, the cable pulley friction model $F_p$ (eq. (2.16)) developed in chapter 2 is added. Now, because of the existence of the cable pulley friction, $T_{mc,i} \neq T_{j,i}$ (i = 1, 2). When the motion of the cable is in the positive direction as defined in Fig.4.2 (i.e. the average cable translation rate $\dot{x}_{c,av} = (\dot{q}_{mc}r_{mc} + \dot{q}_j r_j)/2 \geq 0$), the cable tensions $T_{mc,1}$ and $T_{j,2}$ are larger than the tensions on other side of the cable over the pulleys by the amount of the cable pulley friction. To be exact, $F_H$ for $T_{mc,i}$ and $T_{j,i}$ should be calculated separately because the cable stretch is not equally distributed throughout the cable due to the cable-pulley friction. However, since the cable stretch is obtained based on the difference between the motor encoder and the joint position obtained from numerically solving the dynamics, it is not possible to know the stretch of each cable segment. Therefore, it is assumed the cable stretch is uniform thorough the cable. If the direction of the cable motion is reversed, the frictional force acts on $T_{mc,2}$ and $T_{j,1}$ as below..

$$T_{mc,1} = F_H(x_{s,1}, \dot{x}_{s,1}, z_1) + \frac{F_p(T_1, n_{p,1}, \theta_{w,i,av,1}, \dot{x}_{c,av})}{2}(sign(\dot{x}_{c,av}) + 1) \tag{4.7}$$

$$T_{mc,2} = F_H(x_{s,2}, \dot{x}_{s,2}, z_2) + \frac{F_p(T_2, n_{p,2}, \theta_{w,i,av,2}, \dot{x}_{c,av})}{2}(sign(-\dot{x}_{c,av}) + 1) \tag{4.8}$$

$$T_{j,1} = F_H(x_{s,1}, \dot{x}_{s,1}, z_1) + \frac{F_p(T_1, n_{p,1}, \theta_{w,i,av,1}, \dot{x}_{c,av})}{2}(sign(-\dot{x}_{c,av}) + 1) \tag{4.9}$$

$$T_{j,2} = F_H(x_{s,2}, \dot{x}_{s,2}, z_2) + \frac{F_p(T_2, n_{p,2}, \theta_{w,i,av,2}, \dot{x}_{c,av})}{2}(sign(\dot{x}_{c,av}) + 1) \tag{4.10}$$

$$x_{s,1} = x_{s,0} + (q_{mc} r_{mc} - q_j r_j)/l_0 \tag{4.11}$$

$$\dot{x}_{s,1} = (\dot{q}_{mc} r_{mc} - \dot{q}_j r_j)/l_0 \tag{4.12}$$

$$x_{s,2} = x_{s,0} - (q_{mc} r_{mc} - q_j r_j)/l_0 \tag{4.13}$$

$$\dot{x}_{s,2} = -(\dot{q}_{mc} r_{mc} - \dot{q}_j r_j)/l_0 \tag{4.14}$$

$$T_1 = (T_{mc,1} + T_{j,1})/2 \tag{4.15}$$

$$T_2 = (T_{mc,2} + T_{j,2})/2 \tag{4.16}$$

where $x_{s,0}$ is the strain of cable due to initial tensioning. $x_{s,1}$, $\dot{x}_{s,1}$, $x_{s,2}$,and $\dot{x}_{s,2}$ are the cable strain and strain rate, $z_1$ and $z_2$ are the hysteretic variables, $n_{p,1}$, $n_{p,2}$, $\theta_{w,i,av,1}$, and $\theta_{w,i,av,2}$ are the number of pulleys and average individual wrap angles, and $T_1$ and $T_2$ are the average tensions for the each side of the cable loop (the subscript "1" represents lower and "2" represents upper cables in Fig. 4.2) respectively. The model parameters for the $F_H$ are the same as the ones in Table 3.1 and 3.2 because the function is generalized for different cable lengths by using strain. Part of the model parameters ($c_1$, $c_2$, and $c_3$) for the $F_p$ comes from Table 2.1 and the rest are summarized in Table 4.1.

## *4.3 Model Evaluation*

### *4.3.1 Method*

The tracking accuracy of the new dynamic model was investigated by injecting pre-recorded motor trajectories instead of torque as the input. The reason is that input torque needs to be calculated from the input current and it can be inaccurate. Besides, solving the motor dynamics may cause additional error because of uncertainty of model parameters. However,

Table 4.1: Cable-pulley network friction model parameters (number of small, medium, and large pulley employed $n_p$ and average individual wrap angle $\theta_{w,i,av}$) for the RAVEN II. The subscripts indicate two different cable segments of the cable loop (See Fig. 4.2)

| **Joint** | Small | | Medium | | Large | | Small | | Medium | | Large | |
|---|---|---|---|---|---|---|---|---|---|---|---|---|
| | $n_{p,1}$ | $n_{p,2}$ | $n_{p,1}$ | $n_{p,2}$ | $n_{p,1}$ | $n_{p,2}$ | $\theta_{w,i,av,1}$ | $\theta_{w,i,av,2}$ | $\theta_{w,i,av,1}$ | $\theta_{w,i,av,2}$ | $\theta_{w,i,av,1}$ | $\theta_{w,i,av,2}$ |
| **1** | 0 | 0 | 0 | 0 | 0 | 0 | - | - | - | - | - | - |
| **2** | 3 | 4 | 2 | 2 | 0 | 0 | 56.7 | 65 | 60 | 120 | - | - |
| **3** | 6 | 7 | 5 | 5 | 1 | 1 | 68.3 | 75.7 | 56 | 92 | 180 | 180 |

the motor state tracing is very accurate due to the highly accurate encoder (4000 count per revolution) on each motor. Thus, we disregard the motor dynamics and use the motor states from the encoder. 80000 counts per revolution encoder was attached to the 1st and 2nd joints and 5 $\mu$m linear optical encoder was used for the 3rd joint for ground-truth joint motion data. We injected four different input trajectories as follows.

(1) Sinusoidal wave with frequency of 0.5 Hz.

(2) Sinusoidal wave with frequency of 0.1 Hz.

(3) Sinusoidal wave with frequency of 0.01 Hz.

(4) Actual Fundamentals of Laparoscopic Surgery (FLS) task trajectory recorded using the RAVEN II [21].

For all the tests, the trajectory was injected to the first three joints, two rotational and one translational, used for positioning the end effector simultaneously and we investigated the performances of each joint individually. The new dynamic model was compared against the original kinematic model [39], old dynamic model with optimized parameters [26], and ground truth joint encoder values.

### *4.3.2 Result and Discussion*

The position plots of experiment (1)-(4) are shown in Fig. 4.3-4.6. For all the experiments, the position of the 1st joint of all the models are very close together while there is a gap between all the models and the joint encoder. The results are similar for the 2nd joint but the kinematic model is slightly off of the dynamic models at the peaks. For the 3rd joint, the two dynamic models are relatively close together and correlate with the encoder value better than the kinematic model. For the 1st and 2nd joints, the errors between all the models and encoder value at the peak or trough can be explained by the uncertainty of the transmission ratio. The transmission ratio used in this work is calculated directly from the CAD model. However, due to the thickness of cables and the slight gap between two transmission pulleys, there exists some uncertainties. If the parameter is properly adjusted the offset can be reduced and performance can be improved as described in [27].

The joint encoder reading of the 3rd joint for the sinusoidal input with 0.01 Hz frequency showed non-smooth trajectory. This could be due to the effect of stick-slip friction. Since no stick-slip effect was observed from the experiment of the cable-pulley interaction friction, the stick-slip friction is most likely caused by the linear rail.

The error histogram of the new dynamic model for each experiment is compared side by side against the kinematic model and the old dynamic model (Fig. 4.7-4.10). The error histograms clearly show that all the models are almost identical for the joint 1. For the joint 2, some improvement can be observed over the kinematic model but not much compared to the old dynamic model. The joint 3 error histogram shows that the error bars for the new dynamic model are shifted to left compared to both the kinematic and old dynamic models. Fig. 4.11 summarizes the percentile improvement of the average error and maximum error for each joint and each input trajectory. The improvements of the average and maximum errors are close to zero for all the input trajectories for the joint 1. For the joint 2, the average error is improved by 20-50% and the maximum error is improved only for the 0.01 Hz sine input (about 5% improvement) and FLS input (about

40% improvement). However, no improvement was observed when compared to the old dynamic model. Meanwhile, for the joint 3, both average error and maximum error are smaller for the new dynamic model than the kinematic and old dynamic models. Compared to the kinematic model, the average error was improved by 40-70% and the maximum error was improved by 20-40%. The improvements of the average error and maximum errors were about 10-20% and 5-10% respectively over the old dynamic model.

There is a slight trend of increase of the percentile improvement for the smaller frequency inputs. This can be due to the effect of hysteresis. When the speed is very low or quasi-static, the damping term becomes very small and the old model is not able to capture the energy loss. On the other hand, the new model with hysteresis is capable of capturing the very low speed energy loss and the difference between the loading and unloading phases.

Higher percentile improvement was observed for the FLS input trajectory. The Fast Fourier Transformation of the input trajectory indicated that the frequency ranges up to 0.5 Hz and the distribution was very even throughout. Thus, the reason of the improvement is not simply because the frequency is very low. One unique characteristic of the FLS input is that trajectory is random and the load on the cable varies more frequently compared to the sinusoidal inputs. This could make the results of the new dynamic model and old dynamic model distinct. The effectiveness of hystersis could become more significant if the mass of each link is larger and the difference in the loading and unloading paths is bigger (the hysteresis loop becomes wider in this case). Therefore, cable driven systems with very low speed, frequent change in the loading condition, and large inertia will benefit from the hysteresis model more. The cables used for those joints have larger diameter (diameter and stiffness are close to twice of the thin cable) and shorter length (7 cm for the 1st joint and 40 cm for the 2nd joint compared to 140 cm for the 3rd joint). Therefore, the transmission is very stiff for the 1st joint and it becomes less stiffer for the 2nd and 3rd joints (the cable strain becomes lower). Besides, there is no guide pulley for the 1st joint and there are only 11 pulleys (7 small and 4 medium size) for the 2nd joint while 25 pulleys (13 small, 10 medium, 2 large size) are employed for the 3rd joint. Therefore, the 3rd joint benefited from the new

dynamic model more compared to the other joints and the dynamic models performed very similar to the kinematic model especially for the 1st joint.

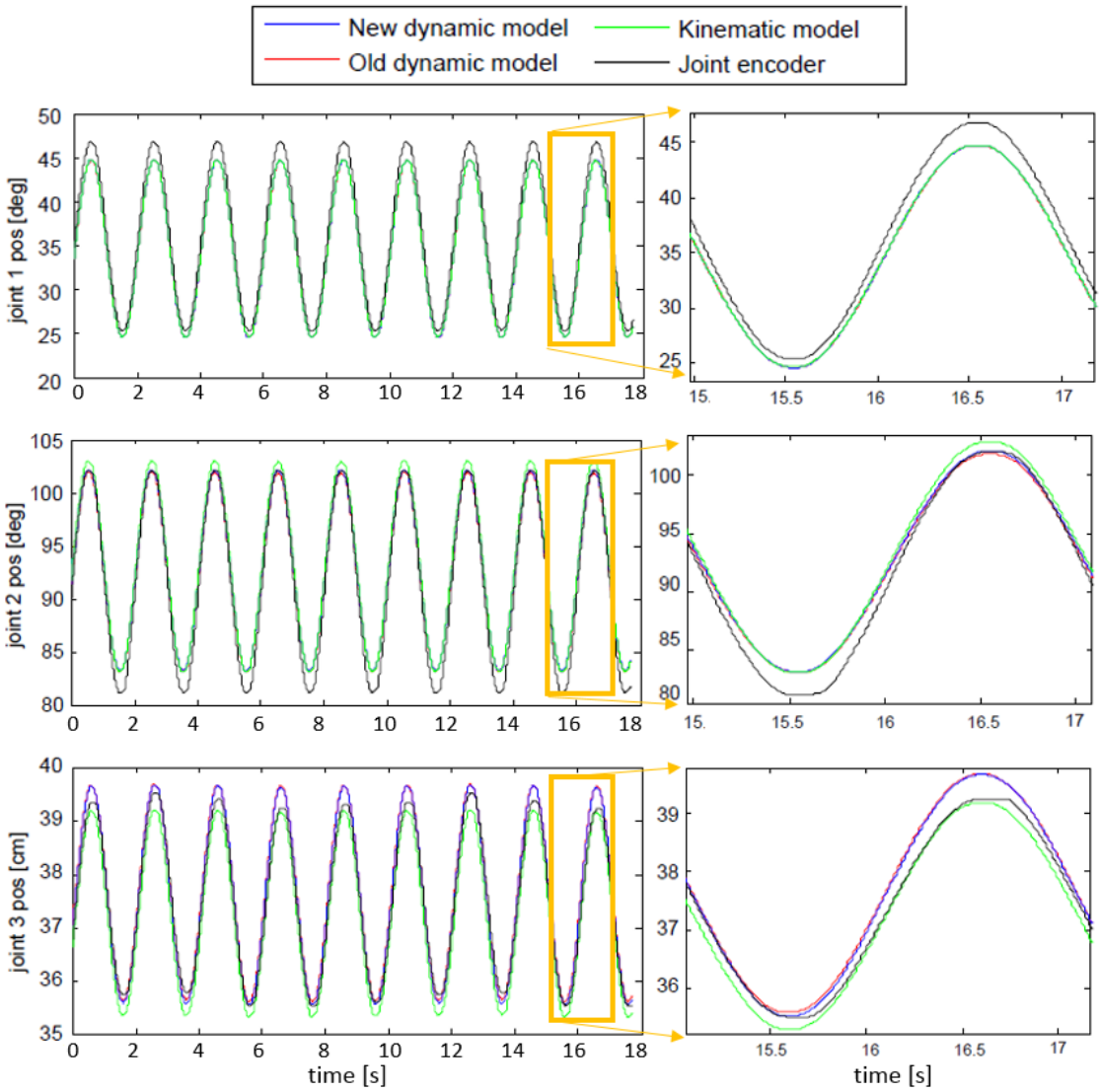


Figure 4.3: Position plot with 0.5 Hz sinusoidal input trajectory.

## *4.4 Conclusion and Future Work*

We developed a dynamic model for the Raven II cable driven surgical robot based on experimental inspection of the actual parts used for the system. The model captures the true

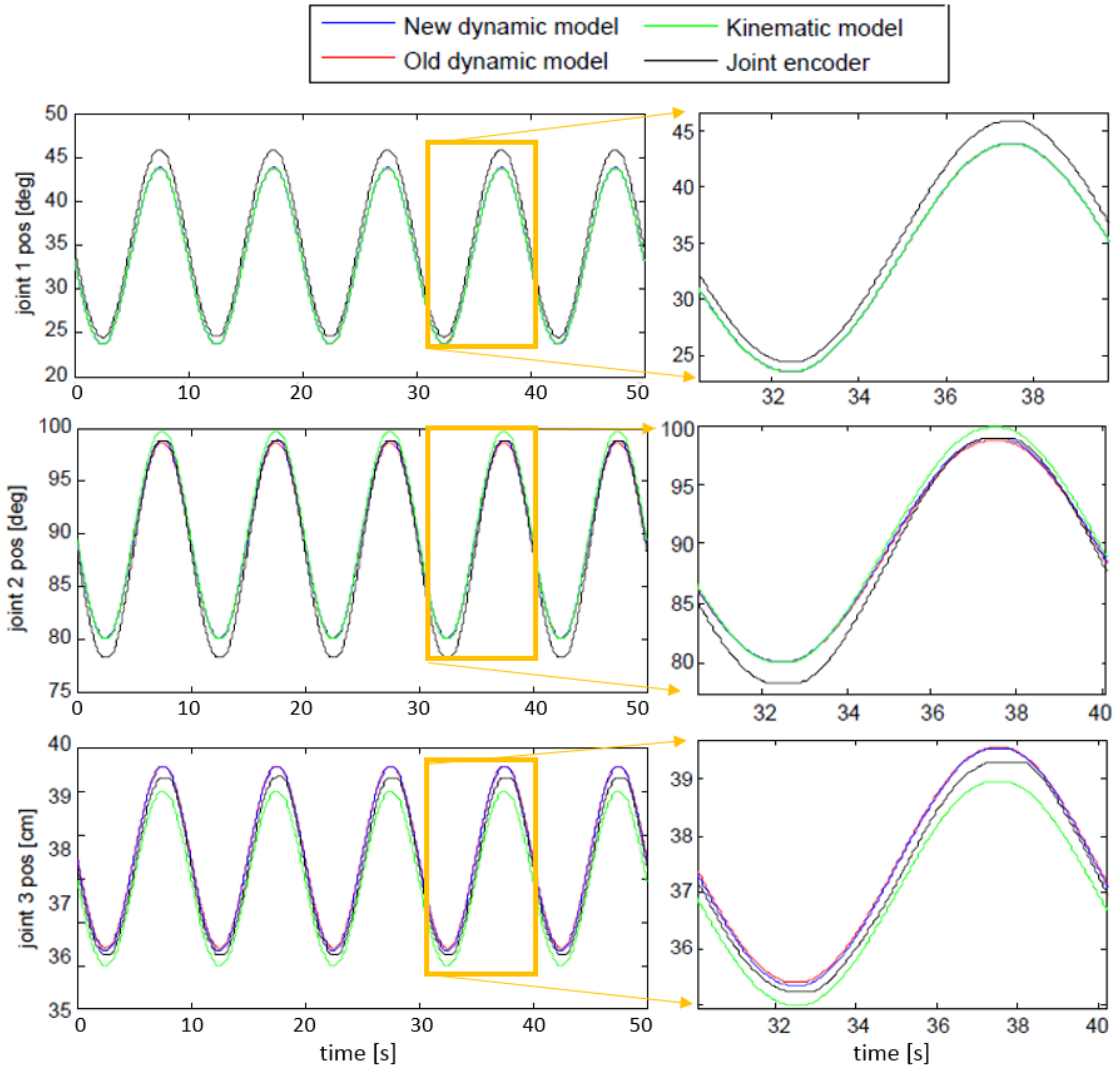


Figure 4.4: Position plot with 0.1 Hz sinusoidal input trajectory.

response of the cable (elasticity, internal friction, material damping, and hysteresis) as well as the guide pulley friction which is formulated as a function of cable tension, number of pulley employed, and wrap angle. Experimentally evaluating the model of the first 3 joints (used for positioning of the end effector) showed the accuracy of the insertion joint (joint 3) was improved (the average error and maximum error were improved by about 10-20% and 5-10% respectively compared to the old dynamic model.). However, the joint 1 and 2

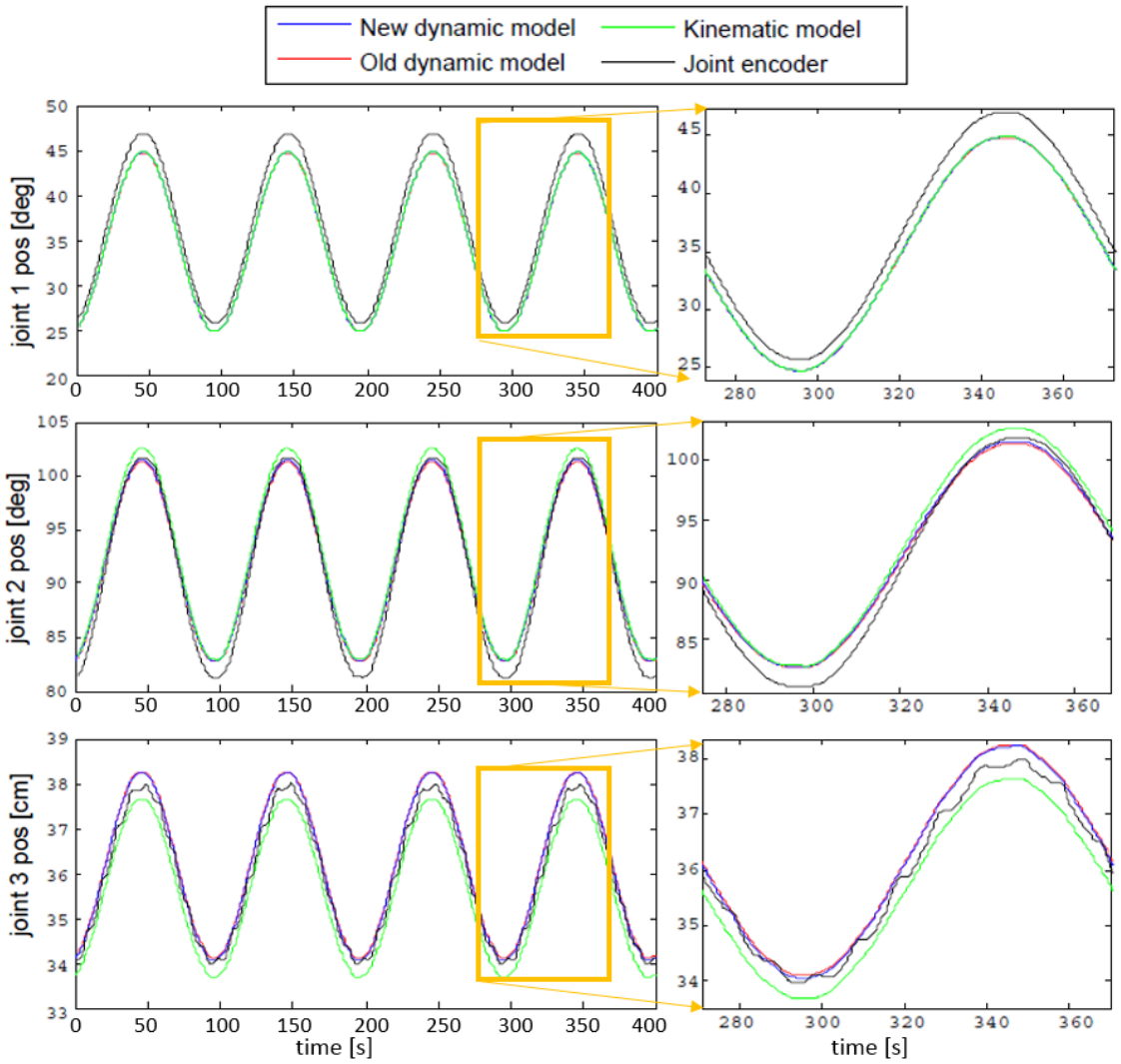


Figure 4.5: Position plot with 0.01 Hz sinusoidal input trajectory.

which use stiffer cable and fewer guide pulleys did not gain any benefit from our method. Since the uncertainty of transmission ratio is not resolved in this work, we need to investigate whether optimizing the transmission ratio improves the performance. Besides, the joint state estimation technique using the UKF as described in [26] can be applied to further improve the accuracy. Moreover, for the joint 3, the experiment with very low frequency sinusoidal input showed stick-slip friction like behavior. Therefore, modeling the stick-slip friction will

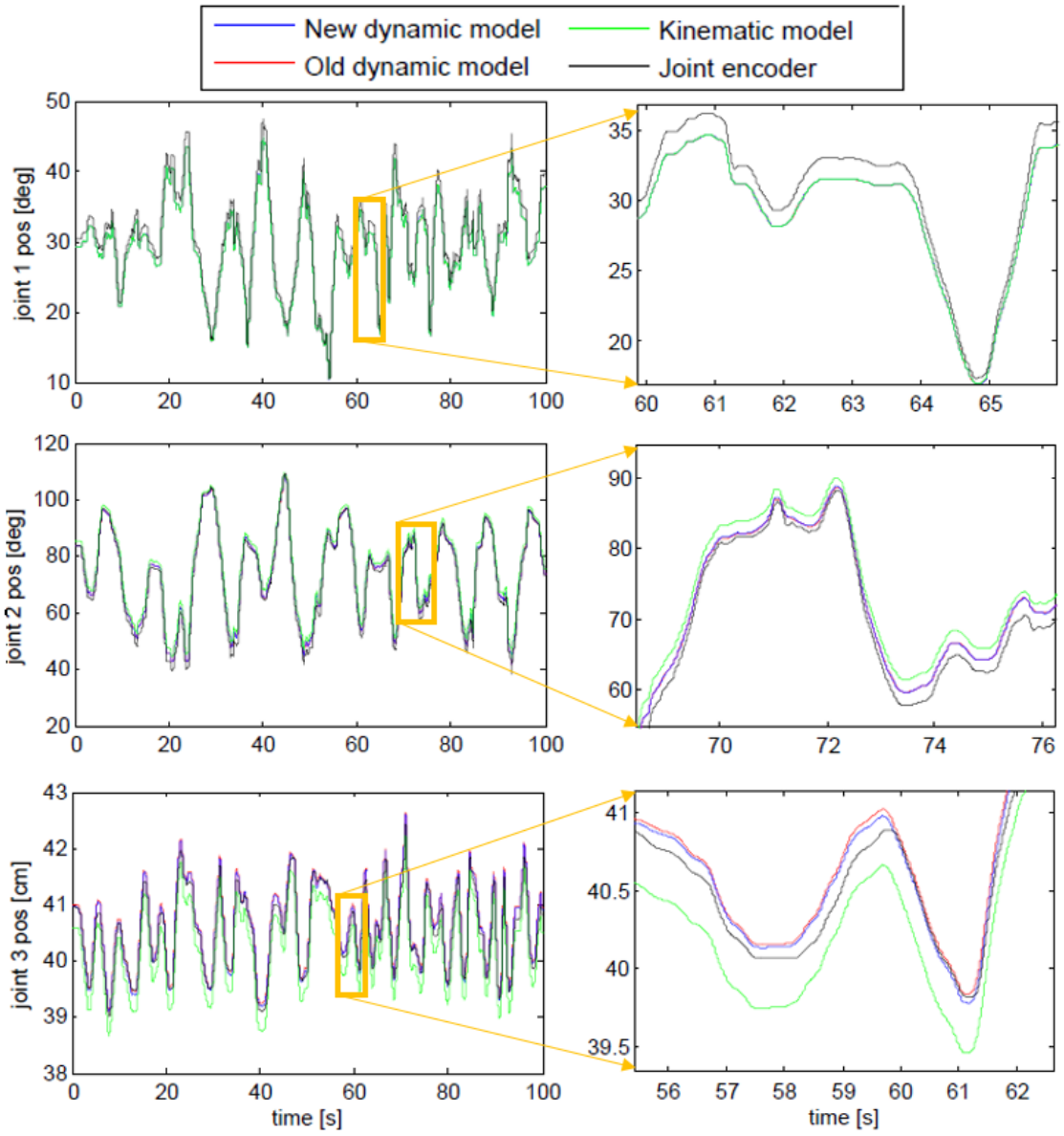


Figure 4.6: Position plot with FLS input trajectory.

improve the low speed regime accuracy of the joint 3. Also, simulation results with different input trajectories indicated that cable driven systems will benefit from the hysteresis model more if the systems have very low speed, frequent change in the loading condition, and large inertia.

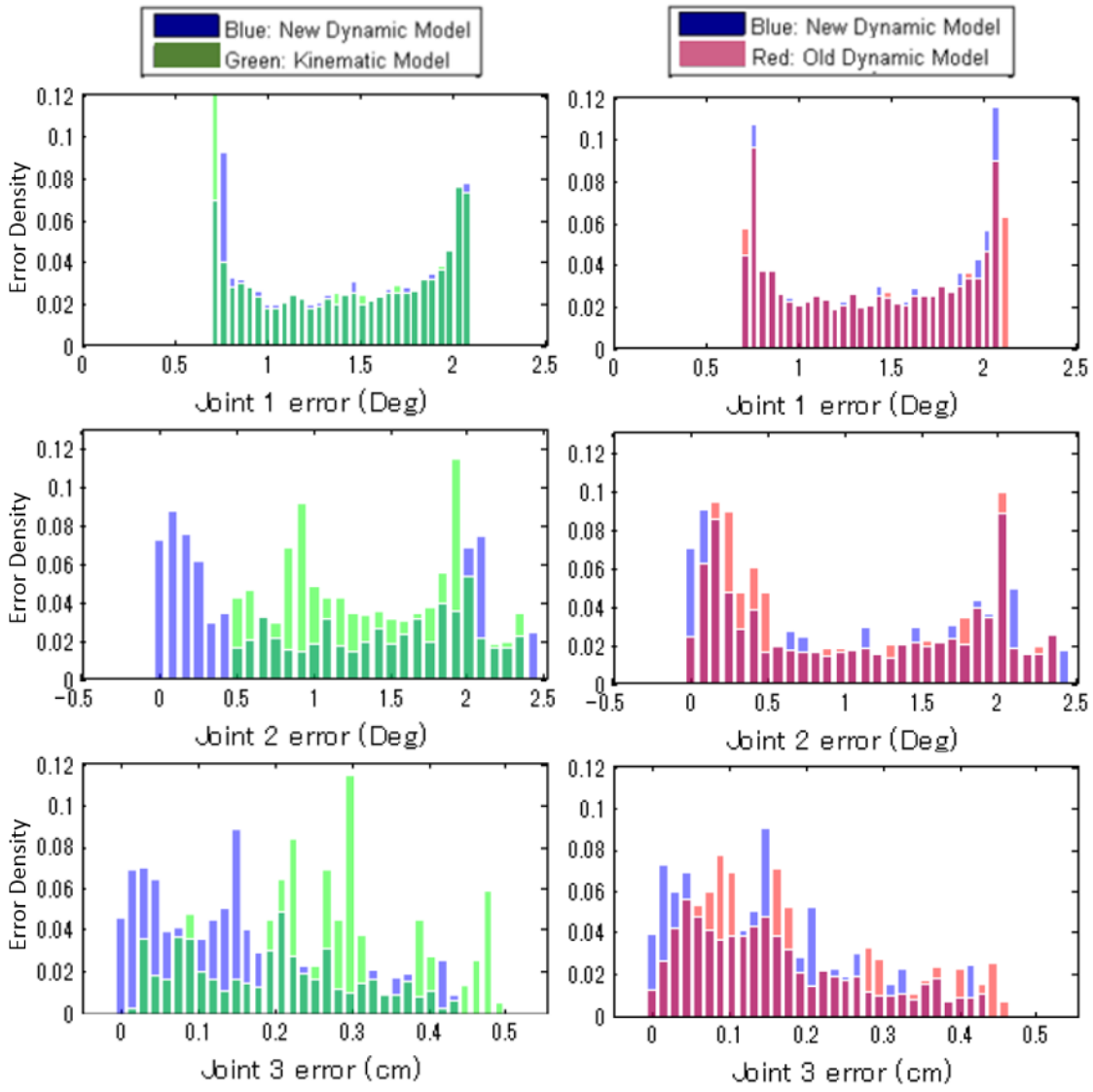


Figure 4.7: Comparison of error distributions for 0.5 Hz sinusoidal input trajectory. The new dynamic model is compared side by side with kinematic model and old dynamic model.

Our method is capable of acquiring force/torque information and energy dissipation happening inside the cable. These information can be used for estimating contact and grasping force and predicting cable fatigue life. Some related work are presented by Kosari et al. [40] and Li et al. [48]. The model parameters were optimized based on the experimental results using fresh cables. After long time use, cable will degrade and parameters might need to

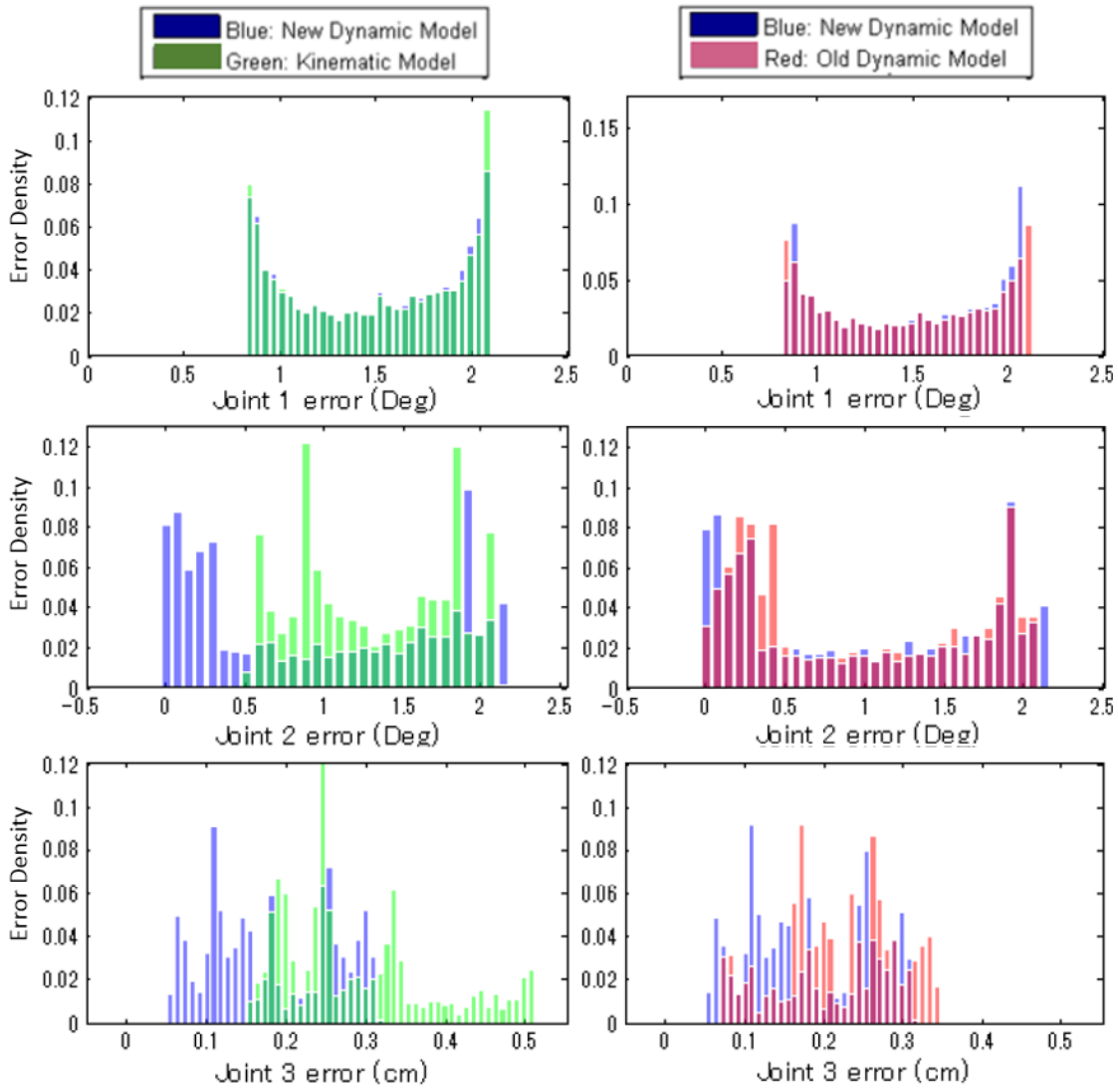


Figure 4.8: Comparison of error distributions for 0.1 Hz sinusoidal input trajectory. The new dynamic model is compared side by side with kinematic model and old dynamic model.

be re-adjusted. Since the fatigue of the cable and the parameter change can be related, the parameters can be predicted using the information of the energy dissipation of the cable combining with other cable fatigue modes such as repeated bending over the sheave.

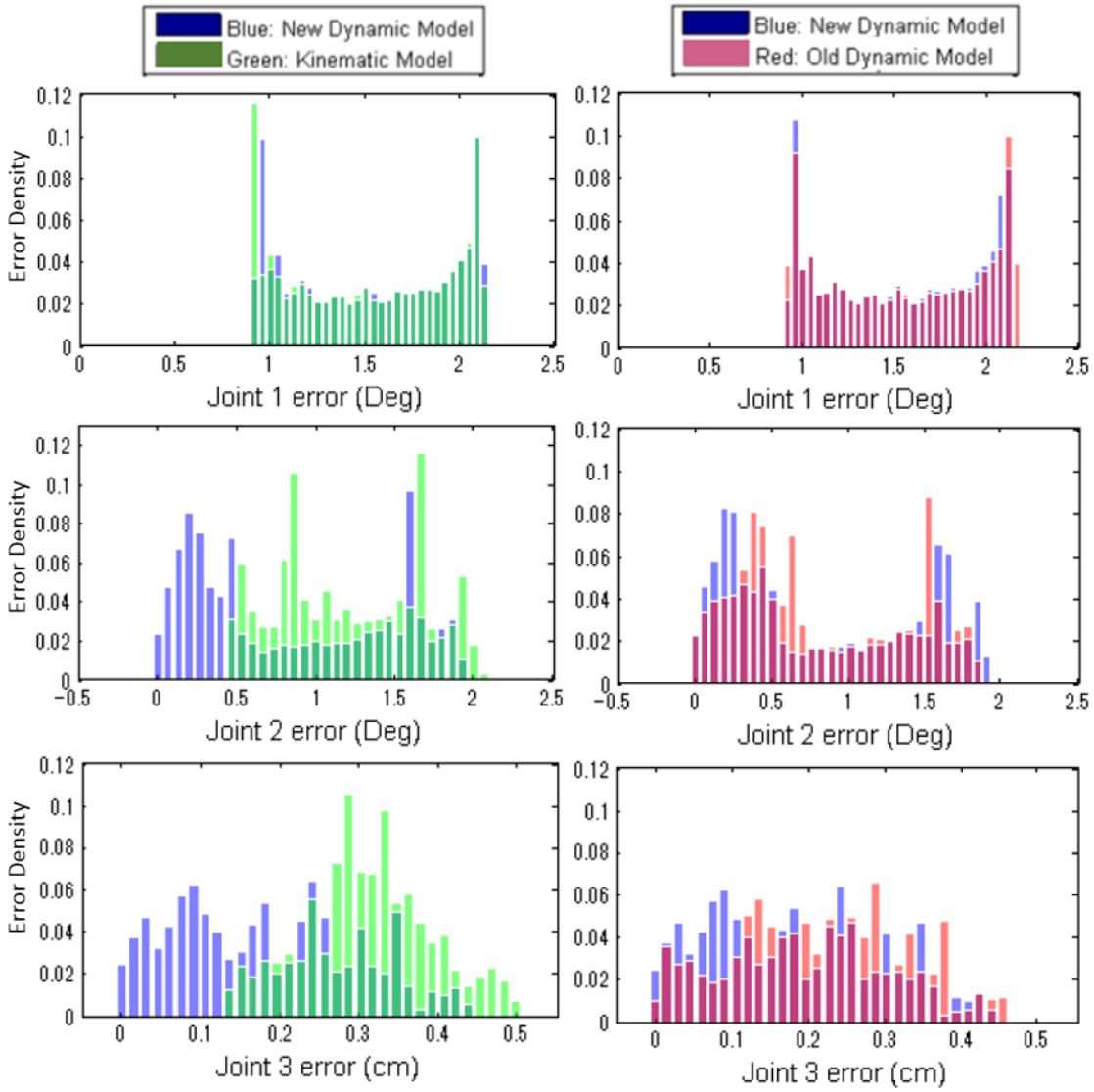


Figure 4.9: Comparison of error distributions for 0.01 Hz sinusoidal input trajectory. The new dynamic model is compared side by side with kinematic model and old dynamic model.

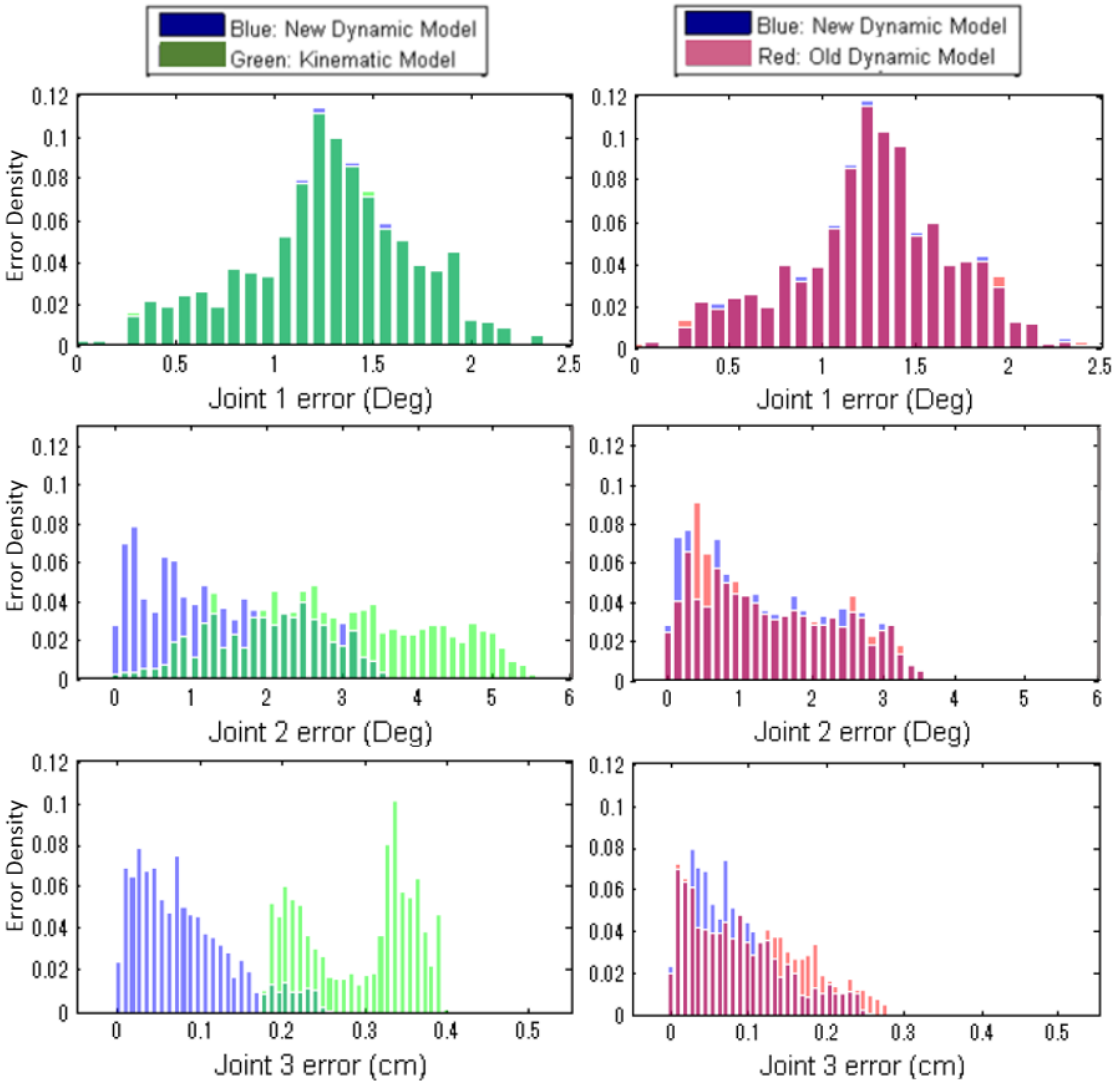


Figure 4.10: Comparison of error distributions for FLS input trajectory. The new dynamic model is compared side by side with kinematic model and old dynamic model.

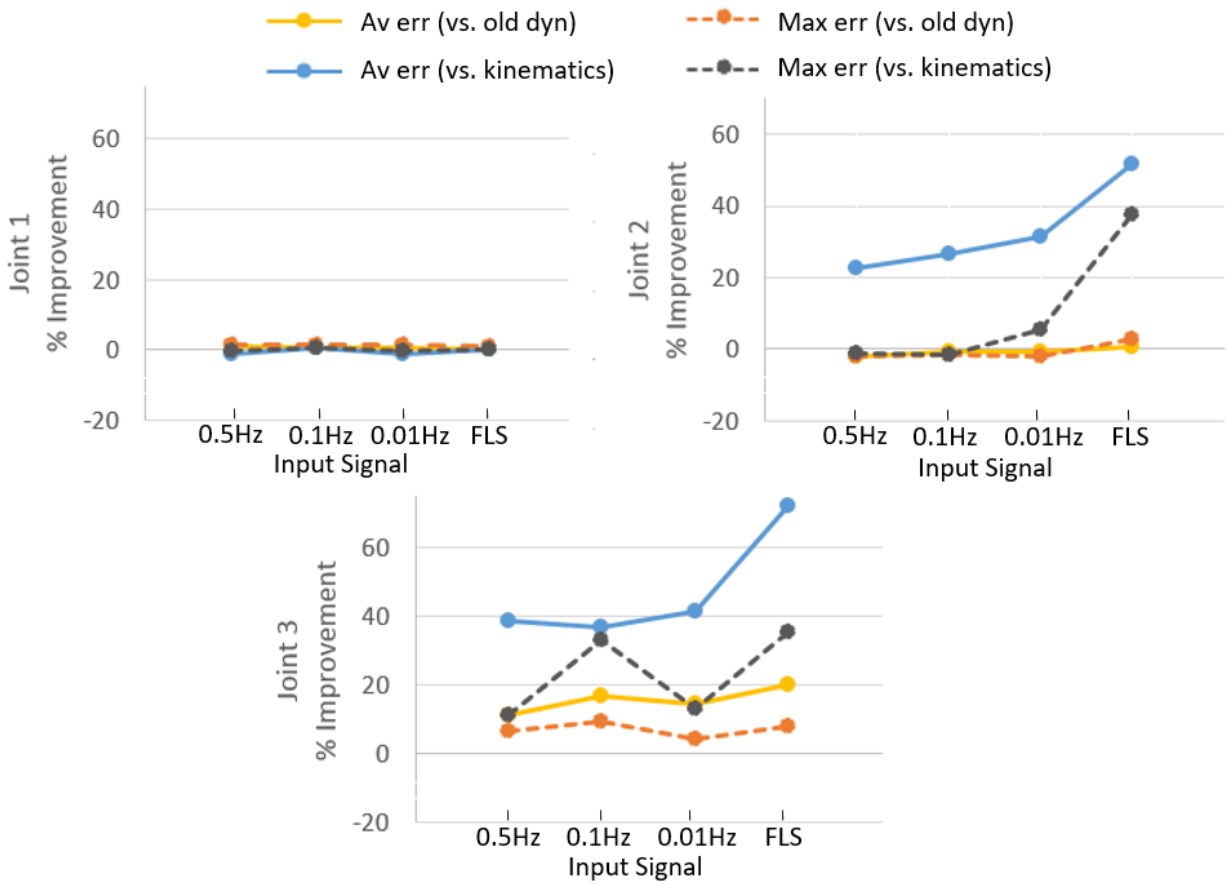


Figure 4.11: Percentile improvement of the new dynamic model (average and maximum error) compared to the old dynamic model and kinematic model. The x axis indicates types of the input (0.5, 0.1, and 0.01 Hz sinusoidal input and FLS trajectory input). Results of each joint are shown in the separate plots.

# Chapter 5

# FATIGUE LIFE OF WIRE ROPES USED FOR ROBOTIC ACTUATION

## *5.1 Introduction*

The types of wire rope fatigue can be classified into 4 categories; tension-tension fatigue (T-T), bending over sheaves (BoS) fatigue, free bending fatigue, and torsion fatigue. Different fatigue mechanisms could co-exist in a fatigue process. For a typical robotic application, wire rope experiences BoS fatigue since wire rope connecting actuator and robot's joint is often guided by idler pulleys. Also, T-T fatigue appears because wire rope is repeatedly loaded and unloaded to actuate robot's joint back and forth.

In this work, the specifications for the experimental setup are determined based on the RAVEN II surgical robotic research platform [29] which uses 0.61 and 1.19 mm diameter wire ropes. Even though wire rope is repeatedly stretched and relaxed when actuating the RAVEN II, we only focus on the BoS fatigue because BoS fatigue is expected to be dominant regarding the fact the fluctuation of the tension is not considerable (empirical RMS tension goes only as high as 10% of wire rope's braking strength).

Plentiful of literatures regarding BoS fatigue life of large scale wire ropes are available. The main applications of those wire ropes include cranes, elevators, aircraft rescue hoisting, mine hoisting, cableways, and deep water offshore mooring [11,23,24,63,68,81,92]. However, the investigation of a small scale wire rope (diameter of less than a few millimeter) has not been active. Even though the results from large wire ropes could be estimated by extrapolation, there is no literature that verifies they could provide a good estimate of wire rope life for a small scale robotic application.

The parameters that affect BoS fatigue are:

- $D/d$ ratio ($D$: diameter of sheave, $d$: diameter of wire rope)
- Tension
- Wrap angle
- Number of reverse bending
- Relaxation length (length between sheaves)
- Angle between sheaves
- Fleet angle
- Groove geometry
- Wire rope construction, grade, and quality
- Wire rope lubrication
- Wire rope speed

Generally, the first two terms have the most influences on the fatigue life. Fatigue life is shortened as $D/d$ ratio decreases or tension, wrap angle, number of reverse bending, and angle between sheaves increase. The details of the effect of the other parameters can be found in [12, 20].

The organization of this chapter is as follows. Section 5.2 presents a well-known wire rope fatigue life prediction model with additional correction factors that is used to compare the experimental results with. Section 5.3 introduces the experimental setup and specifications. Section 5.4 shows the experimentally measured BoS fatigue life. Finally, section 5.5 gives conclusions and discusses work left out in this study.

### *5.2 BoS Fatigue Life Prediction Model*

In this section, we present a prediction model for wire rope's BoS fatigue life cycle developed by Feyrer [20] which will be compared against experimentally obtained fatigue life cycle in section 5.4.

$$\begin{aligned} logN = b_0 + (b_1 + b_3 log\frac{D}{d})(log\frac{S}{d^2} - 0.4log\frac{R_0}{1770}) \\ + b_2 log\frac{D}{d} + logf_d + logf_L + logf_C \end{aligned} \tag{5.1}$$

where $N$ is the fatigue cycle till failure (there exist different definitions of failure), $d$ is nominal rope diameter in $mm$, $D$ is sheave diameter in $mm$, $S$ is tension in $N$, and $R_0$ is nominal tensile strength in $N/mm^2$. The constants $b_1$, $b_2$, $b_3$, are determined depending on the construction of wire rope and $b_0$ is based on both the wire rope construction and the definition of failure. Feyrer presented 4 different failure criteria as follows:

- $\overline{N}$: Mean breaking number of bending cycles.
- $N_{10}$: With 95 % certainty, not more than 10 % of the wire ropes break.
- $\overline{N_A}$: Mean discarding number of bending cycles.
- $N_{A10}$: With 95 % certainty, not more than 10 % of the wire ropes are in the discarding condition.

Breaking number of bending cycle is defined as the cycle when at least one strand is broken. The discarding number is based on the number of wire rope break found at 80 % of the breaking number of bending cycle. In this work, experiments were continued until wire ropes reach the condition of $N_{10}$. In the case of wire rope we test, 10 % of wire rope is equivalent to 0.7 strands or 13.3 wires.

The endurance factors $f_d$, $f_L$, $f_C$ are defined based on rope diameter, bending length, and number of rope strands . To take account of the rope lubrication, fleet angle, and groove geometry, $N$ needs to be multiplied by correction factors $f_{N1}$-$f_{N4}$.

$$N_{cor} = N f_{N1} f_{N2} f_{N3} f_{N4} \tag{5.2}$$

The tested angles between sheave axis are 0° so no correction factor is required. Deviation of the fatigue life due to reverse bending was experimentally derived.

$$N_{rev,cor} = a_0 N_{sim,cor}^{a_1} \left(\frac{D}{d}\right)^{a_2} \tag{5.3}$$

$N_{rev,cor}$ and $N_{sim,cor}$ stand for number of fatigue life cycles due to reverse bending and simple bending after correction in eq. (5.2) ($N_{sim,cor} = N_{cor}$). Values of $a_0$, $a_1$, and $a_2$ varies depending on the definition of failure.

The full cycle includes 2 simple bending and 2 reverse bending. To calculate the total bending life cycle, the Palmgren-Miner-Rule is employed.

$$N_{total} = \frac{N_{sim,cor} N_{rev,cor}}{2N_{sim,cor} + 2N_{rev,cor}} \tag{5.4}$$

One problem with the Feyrer's model is that the endurance factor for the rope diameter $f_d$ is not well defined for small rope diameters (less than 6 mm). The suggested formula is

$$f_d = \frac{0.52}{-0.48 + (d/16)^{0.3}} \tag{5.5}$$

However, when 0.61 mm and 1.19 mm are used for $d$, $f_d$ becomes negative and it eventually causes error when calculating $log f_d$ in eq. (5.1). Since there is no other reference for what value should be used for 0.61 mm and 1.19 mm diameter ropes, we used the following alternative expression in [20] when calculating $f_d$.

$$f_d = \left(\frac{d}{16}\right)^{-0.63} \tag{5.6}$$

The basic form of this equation was found by Shitkow and Pospechow in 1957. It was originally

$$f_d = \left(\frac{d}{16}\right)^{-0.32} \tag{5.7}$$

but the exponent was adjusted by Feyrer later.

Similar problem arises for the bending length endurance factor $f_L$. The formula developed by Feyrer is valid when the nominal bending length $l \geq 10d$ (the bending lengths tested in the experiments are 2.985 mm and 5.970 mm while $10d$ are 6.1 and 11.9 mm.).

$$f_L = \frac{1.54}{2.54 - (\frac{l/d-2.5}{57.5})^{-0.14}} \tag{5.8}$$

Although we still rely on this formula, when $d = 1.19$, $f_L$ grows to infinity as $l$ approaches to 3.063 and it becomes negative or complex conjugate for $l < 3.063$. For this case, $f_L$ is selected such that the model matches the experimental results (see section 5.3 for more details).

Another problem of the Feyrer's formula is that the effect of relaxation length is not included. Optimal rope life can be achieved if the relaxation length (distant between the sheaves) is at least 3 to 4 rope lay lengths to allow the wires and stands relax and realign [87]. Raoof et al. performed in depth investigation of recovery length of large diameter wire rope (more than 16.4 mm diameter strand (strand diameter is sub-millimeter in our study)). They formulated recovery length of any layer of wire rope strand with any constructions [66]. However, how the length between sheaves affect the BoS fatigue life is not discussed. In practice, if the relaxation length is less than the circumference of sheave, the bending cycle is counted as double [1]. Since our experimental setup has relaxation length of less than the sheave's circumference, the calculated fatigue life cycle in eq. (5.4) is reduced by a factor of 2.

### *5.3 Experimental Setup and Specifications*

The experimental conditions are determined based on the RAVEN II. We selected the portion of the pulley arrangement which causes the most severe fatigue. In this work, the discarding number of bending cycles $N_A$ is investigated. Detailed information of each parameter is as follows (the parameters in bold are investigated and the rest is kept unchanged):

- $D/d$ **ratio**: See Table 5.1.

Table 5.1: $D/d$ ratio tested in the experiments

| Pulley Dir. \ Rope Dir. | 0.61 [mm] | 1.19 [mm] |
|---|---|---|
| 7.6 [mm] | 12.46 | 6.39 |

- **Tension**: 10, 15, 20, 25, 30, and 35 N. These values are chosen based on the empirical RMS tension of 33 N.

- **Wrap angle**: 45° and 90°. The bending lengths are 2.985 and 5.970 mm respectively. These are the major wrap angles used for the RAVEN II (Fig. 5.1).

- Number of reverse bending: 2 (in one fatigue cycle).

- Relaxation length (length between sheaves): 10 mm. This value is less than 3 lay lengths of the wire rope and circumference of the sheave. (The lay length of the 0.61 mm wire rope is 5.5 mm and 1.19 mm wire rope is 9 mm. The sheave's circumference is 23.88 mm.)

- Angle between sheave axis: 0°. It ranges from 0° to 90° but it's mostly 0° for the RAVEN II.

- Fleet angle: 0°. Fleet angles of all pulleys are 0° for the RAVEN II.

- Groove geometry: As shown in Fig. 5.2. Pulleys are made out of 6061 aluminum with hard anodized finish.

- Wire rope construction, grade, and quality: The construction of both ropes is regular lay 7 x 19 IWRC (6 strands are helically twisting around a core strand and each strand consists of 19 wires). Both ropes are manufactured by Carl Stahl Sava Indstries, Inc and made out of type 304 stainless steel. 1.19 mm wire rope has braking strength ($F_B$) of 1112 N and 0.61 mm has $F_B$ of 222 N (Fig. 5.3).

- Wire rope lubrication: Lubricated.

- Wire rope speed: 1.3 m/s (empirical RMS value).

The experimental setup is shown in Fig. 5.4. The wire rope is driven using the same motor used for the RAVEN II (Maxon RE 30 brushed motor). An Arduino (Mega 2560) was used for the motor control. The travel distance, denoted as "$s$" was determined to achieve "straight - bend - straight - bend - straight" for a half cycle which results 2 simple bending and 2 reverse bending for 1 full cycle (Fig. 5.5). Wire rope's tension was set by hanging two equal weights onto the two bottom idler pulleys which are connected with a rigid bar in the back of the board. The weights were kept hung during the experiments to hold constant tension.

In order to detect frays of wire ropes, we made a device shown in Fig. 5.6. The device is mounted at the end of travel range and wire rope goes through a hole on the stainless steel sheet on the device. The distance between the outer surface of the wire rope and the stainless steel sheet is set to become one half of wire rope's radius. The thickness of the sheet is 0.2 mm. When frays or broken wires make contact with the sheet, an electrical circuit connected to the device is closed and a counter is incremented.

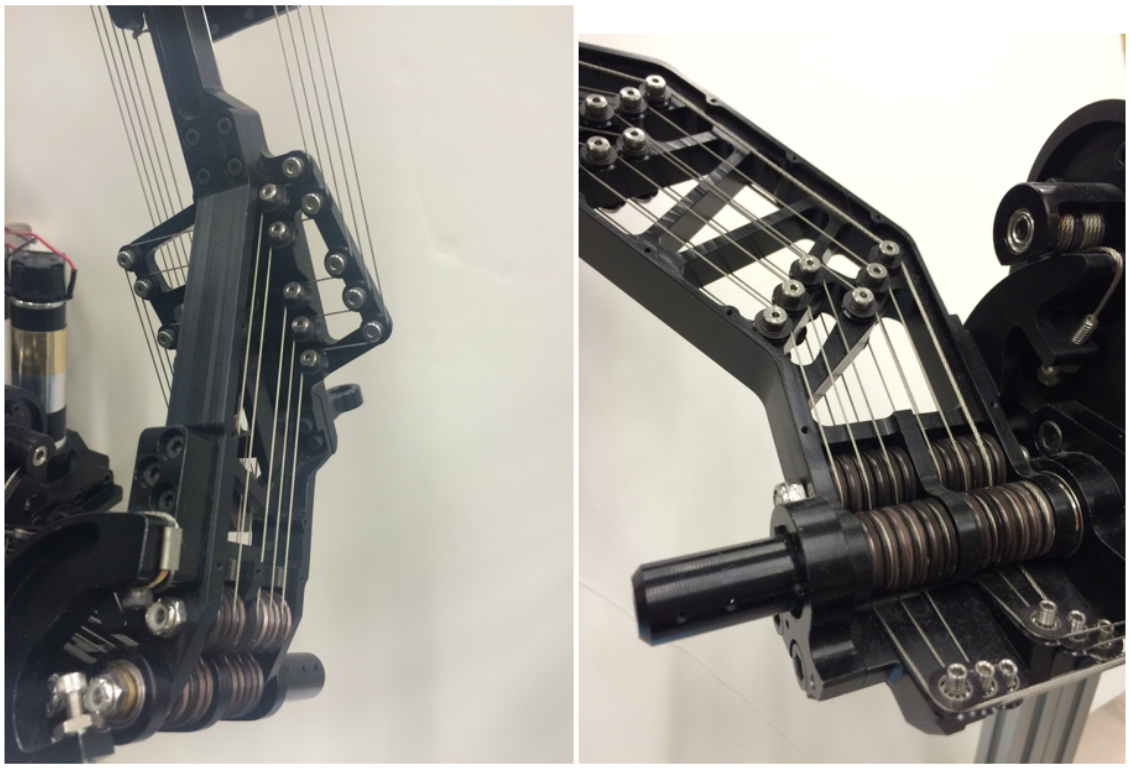

Figure 5.1: Pulley and wire rope configuration of the RAVEN II.

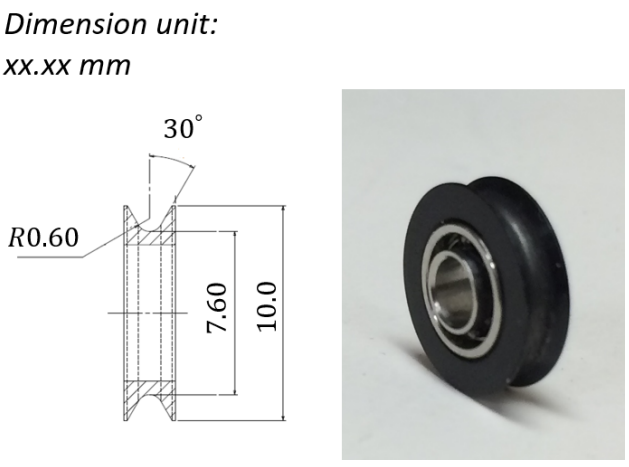


Figure 5.2: Small pulley used for the RAVEN II.

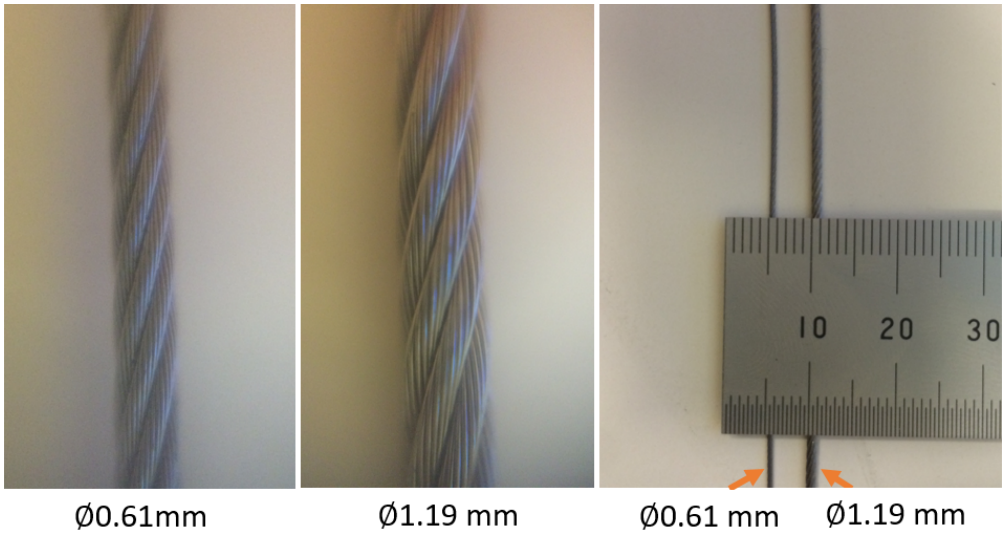


Figure 5.3: Actuation wire ropes used for the RAVEN II (regular lay, 7x19 IWRC, type 304 stainless steel).

Experiments were continued until the fray counter reaches 150 for 0.61 mm wire rope and 100 for 1.19 mm wire rope. These values were determined experimentally. We observed that wire ropes reach the the discarding number of bending cycles when the counter hits these values. We also inspected the wire rope visually in order to ensure the condition of the wire ropes.

Since the friction coefficient of pulley bearing is lower and the inertia of the pulley is small, fatigue caused by the sliding between the wire rope and pulley is excluded.

## *5.4 Experimental Results and Discussions*

The BoS fatigue life cycle is plotted as a function of tension. The types of the experimental conditions are shown as below.

1. 0.61 mm diameter rope with 45° wrap angle (Fig. 5.8)
2. 0.61 mm diameter rope with 90° wrap angle (Fig. 5.9)
3. 1.19 mm diameter rope with 45° wrap angle (Fig. 5.10)
4. 1.19 mm diameter rope with 90° wrap angle (Fig. 5.11)

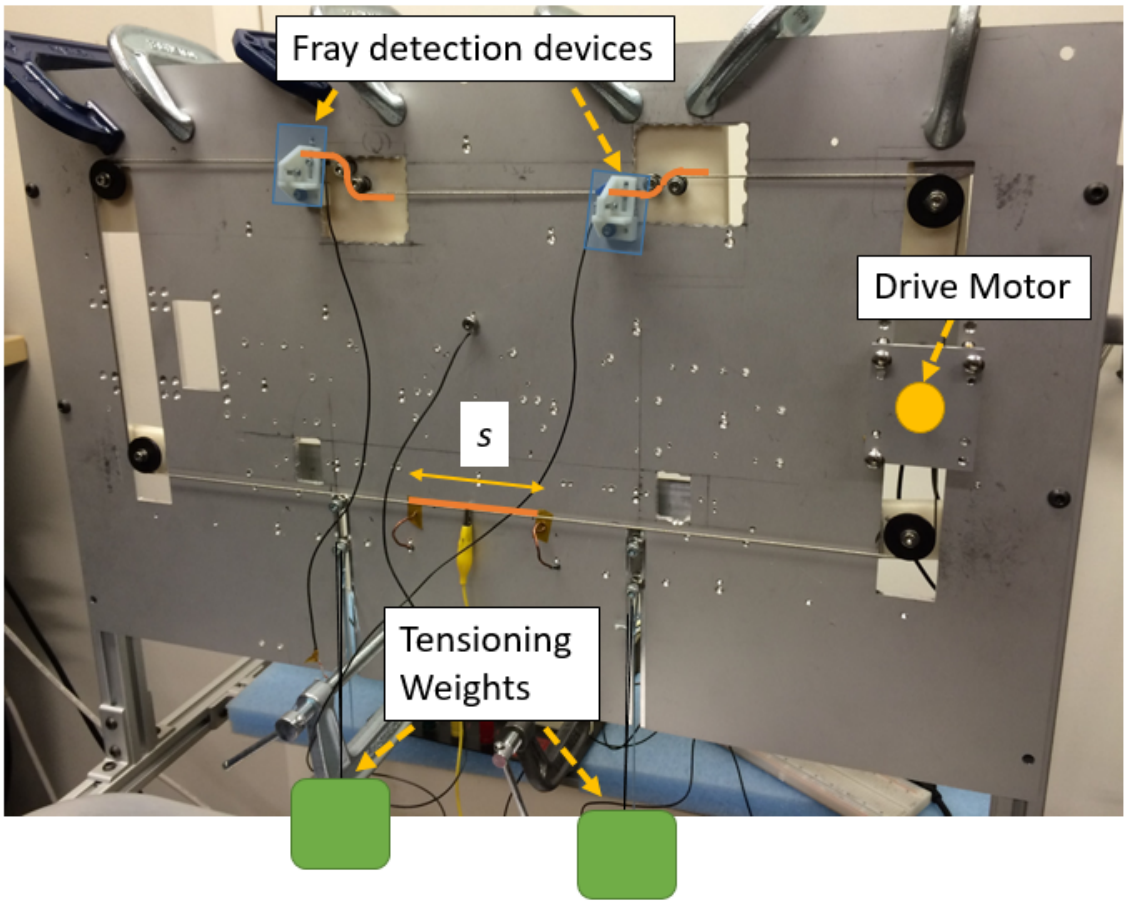


Figure 5.4: BoS fatigue life measurement setup. The travel distance of wire rope for a half cycle is highlighted in orange.

The experimental results are compared against the Feyrer's model. Even though all the constants for the Feyrer's prediction model are summarized in [20], not all the values that suit for our experimental setup are presented. Therefore, proper values are selected either by interpolation/extrapolation or based on the closest condition. The values of the coefficient are summarized in Table 5.2 and 5.3.

As described in section 5.2, there is a limitation in eq. (5.5) when wire rope diameter is very small. Therefore, the model calculated life cycle is plotted with two different $F_d$'s, the original one in eq. (5.7) and the one adjusted by Feyrer in eq. (5.6) (Table 5.4). The bending

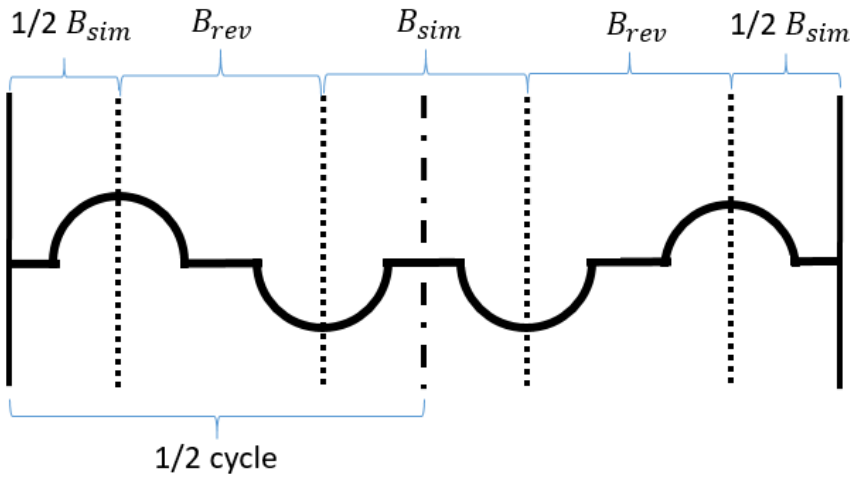


Figure 5.5: 1 fatigue cycle achieved in the experimental setup. $B_{sim}$ and $B_{rev}$ stand for the simple and reverse bending respectively.

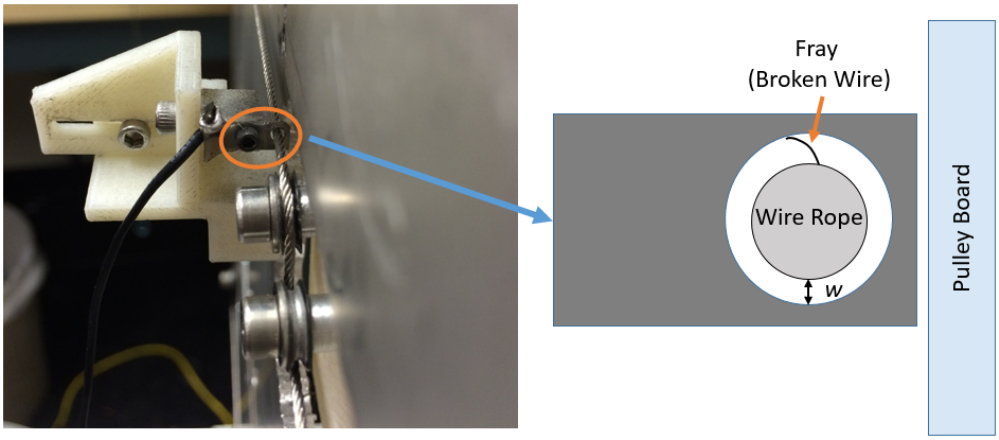


Figure 5.6: Wire rope fray detector setup. The distance between the wire rope's outer surface to the detector $w$ was set to be one half of wire rope's radius. The thickness of the stainless steel sheet is 0.2 mm.

length endurance factors $f_L$ are calculated based on the eq. (5.8) for all the experiments except for the experiment 3 because $log f_L$ cannot be evaluated.

The results of experiment 1, 2, and 4 indicate that the actual BoS fatigue life cycles are longer than the models predicted. Acting on this result, the exponent of the formula

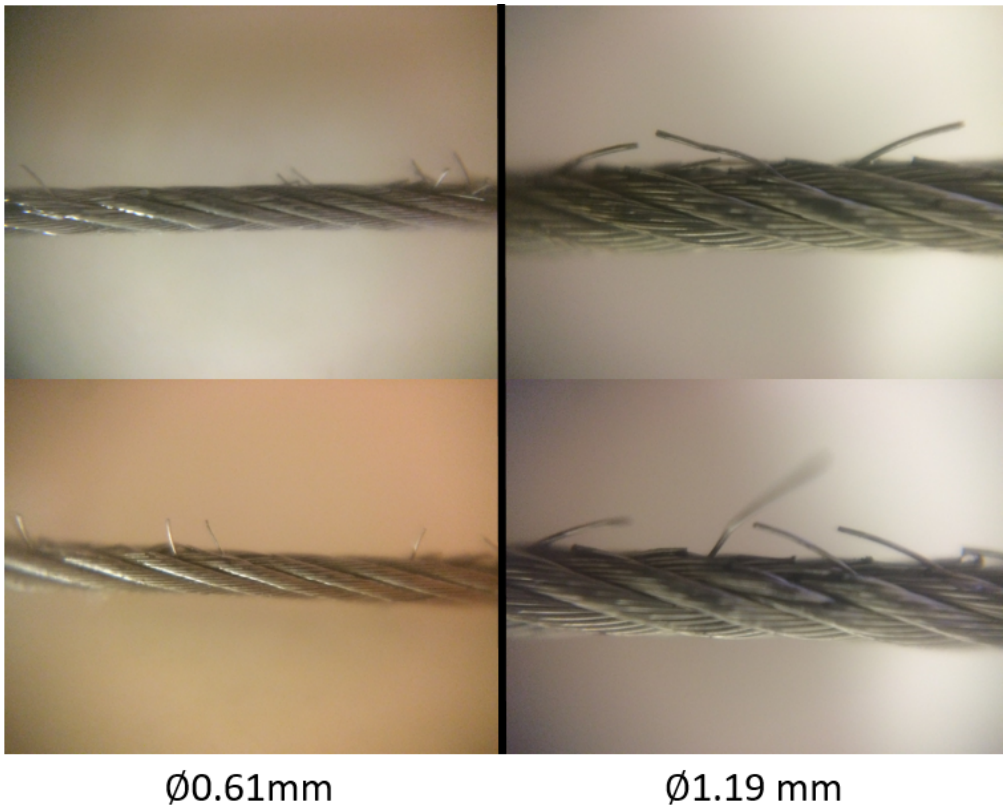


Figure 5.7: Wire ropes reached at the failure threshold of our definition.

of $F_d$ was adjusted such that the model approaches to the experimental result (denoted as modified $F_d$). The value of the exponent was -0.98 and the values of $F_d$ are shown in Table 5.4.

In the case of experiment 3, $f_L$ was selected after adjusting $F_d$. All the values of $f_L$ are presented in Table 5.5. The value of $f_L$ is much higher than the ones from the other experiments. This makes sense because even though the original value becomes negative causes error, it is supposed to increase toward an asymptote and grow very rapidly.

Other than the experiment 3, the decrease of the curves is not as rapid as what the models predict. The trend of the curve is determined by the coefficients $b_1$ and $b_3$ whose values are based on Warrington 8x19 wire rope. Even though there exists a correction factor for the rope core type the number of strands ($f_C$), this factor only can shift the entire curve

Table 5.2: Constants for the Feyrer's model (eq. (5.1))

| Parameters | 0.61 mm rope | 1.19 mm rope |
|---|---|---|
| $b_0$ | -2.064 | -2.064 |
| $b_1$ | 1.588 | 1.588 |
| $b_2$ | 8.056 | 8.056 |
| $b_3$ | -2.577 | -2.577 |
| $R_0$ | 760 | 1000 |
| $f_C$ | 0.905 | 0.905 |

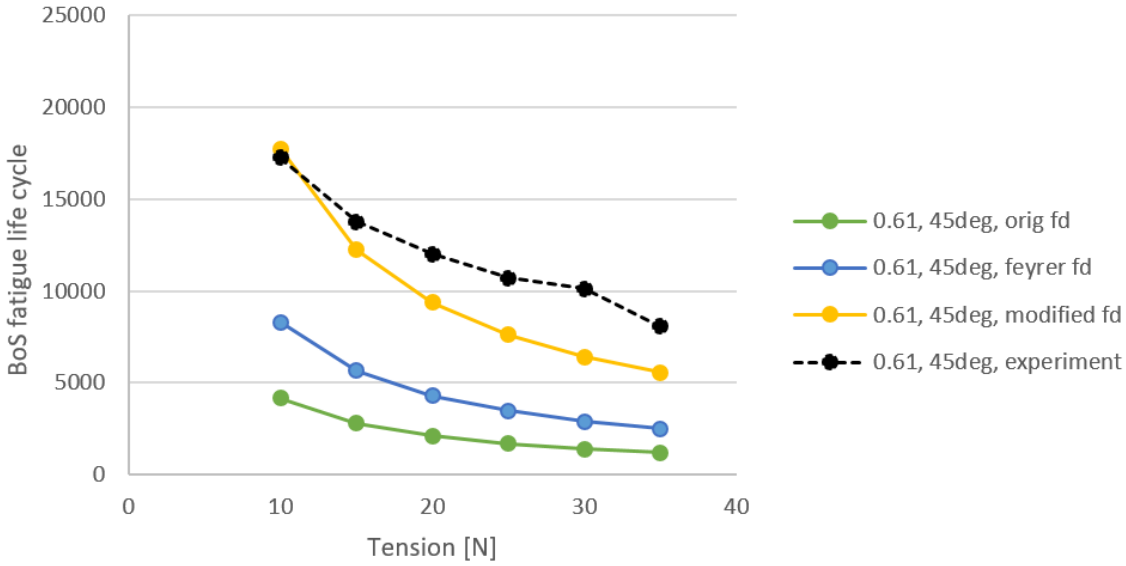


Figure 5.8: BoS fatigue life for the experiment 1.

up or down. Therefore, additional correction factor might be required in order to capture the actual trend of the BoS fatigue life of small scale wire ropes.

The reason the experiment 3 does not have moderate decrease compared to the other experiment might be because of the small $l/d$ ratio ($l$ is about 1/4 of $10d$ in comparison with 1/2 to 1 for the other experiments).

Table 5.3: Endurance Factors for eq. (5.2) and coefficients for reverse bending for eq. (5.3)

| Parameters | 0.61 mm rope | 1.19 mm rope |
|---|---|---|
| $f_{N1}$ | 0.9 | 0.9 |
| $f_{N2}$ | 1 | 1 |
| $f_{N3}$ | 0.481 | 1.0 |
| $f_{N4}$ | 0.901 | 0.864 |
| $a_0$ | 3.635 | 3.635 |
| $a_1$ | 0.671 | 0.671 |
| $a_2$ | 0.449 | 0.449 |

Table 5.4: Endurance Factor for Wire Rope Diameter

| Parameters | 0.61 mm rope | 1.19 mm rope |
|---|---|---|
| Feyrer $f_d$ | 7.831 | 5.140 |
| Orig $f_d$ | 2.845 | 2.297 |
| Modified $f_d$ | 24.571 | 12.764 |

Normalized errors of the models with different $f_d$'s with respect to the experimental data are summarized in Fig. 5.12. It is shown that the the average error of the Feyrer model with the modified $f_d$ is less than 20% for all the experiments whereas the average errors of the model with the Feyrer $f_d$ and original $f_d$ range up to 65% and 80%.

### *5.5 Conclusions*

We experimentally investigated fatigue life of the type 304 stainless steel wire rope with construction of 7 x 19 which is used for the actuation of the RAVEN II surgical robot. In the experiments, how $D/d$ ratio, tension, and wrap angle affect the fatigue life was tested while

Table 5.5: Endurance Factor for Bending Length

| Parameters | 0.61 mm rope | 1.19 mm rope |
|---|---|---|
| $f_L$ | 1.572 (for 45°) | 19 (for 45°) |
| | 1.278 (for 90°) | 1.555 (for 90°) |

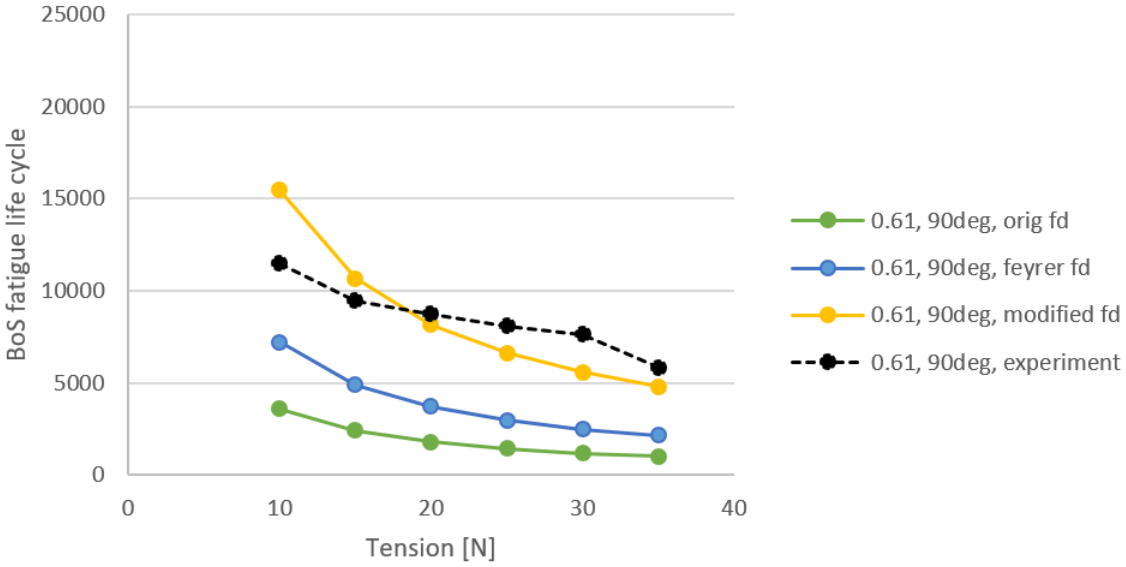


Figure 5.9: BoS fatigue life for the experiment 2.

keeping the other parameters unchanged (i.e. Number of reverse bending in one cycle: 2, Relaxation length: 1-2 rope lay length or less than circumference of sheave, Angle between sheave axis: 0°, Fleet angle: 0°, Wire rope's speed: 1.3 $m/s$).

The BoS fatigue life obtained from the experiments showed that the experimental results correlate with the Feyrer model better if the exponent of the formula of the wire rope diameter endurance factor is changed to -0.89. Also, when the bending length is about 1/4 or less than 10 times of wire rope diameter, the bending length endurance factor needs to be big. In this study, we only performed one experiment with very small $l/d$ ratio. In order to generalize the trend for that range, more experiments need to be performed.

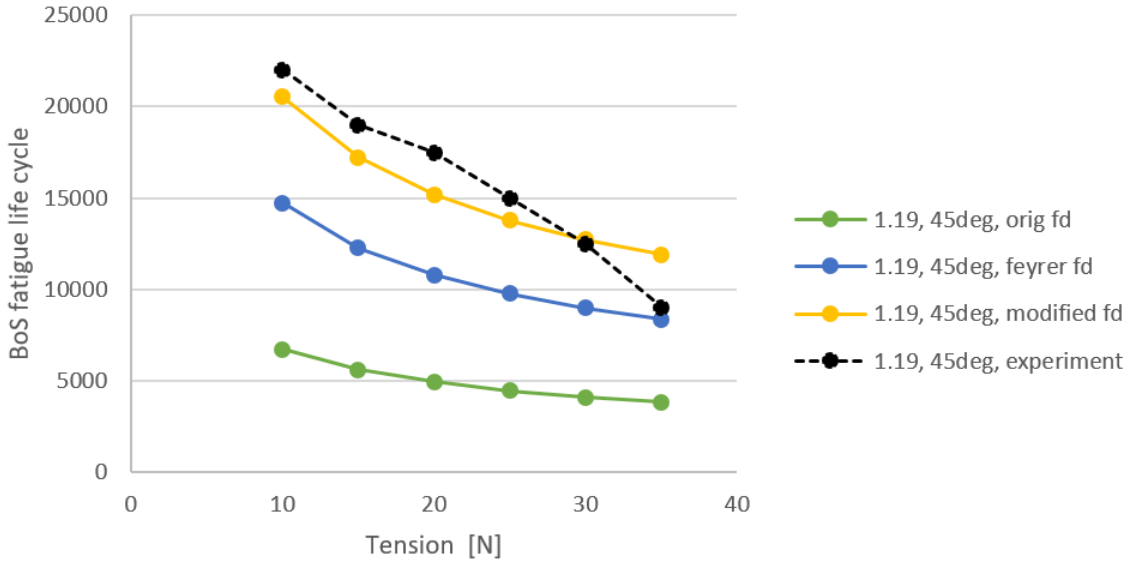


Figure 5.10: BoS fatigue life for the experiment 3.

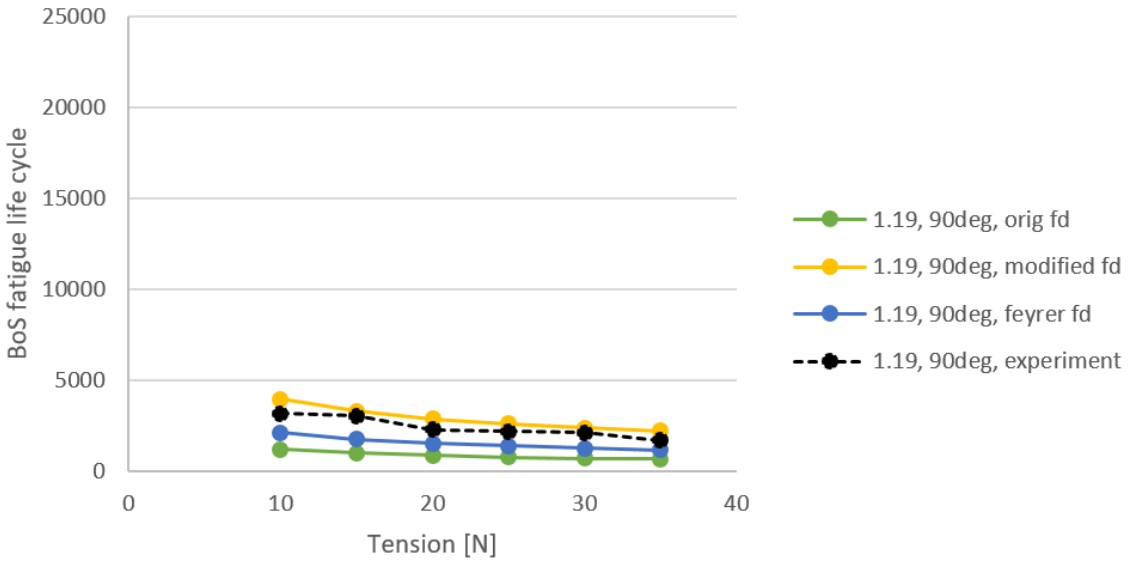


Figure 5.11: BoS fatigue life for the experiment 4.

Even though modifying the wire rope diameter endurance factor improves the performance of the Feyrer model, it could correlate with the experimental results better in terms of the speed of decay. Therefore, to fine tune the Feyrer's model, more various combinations

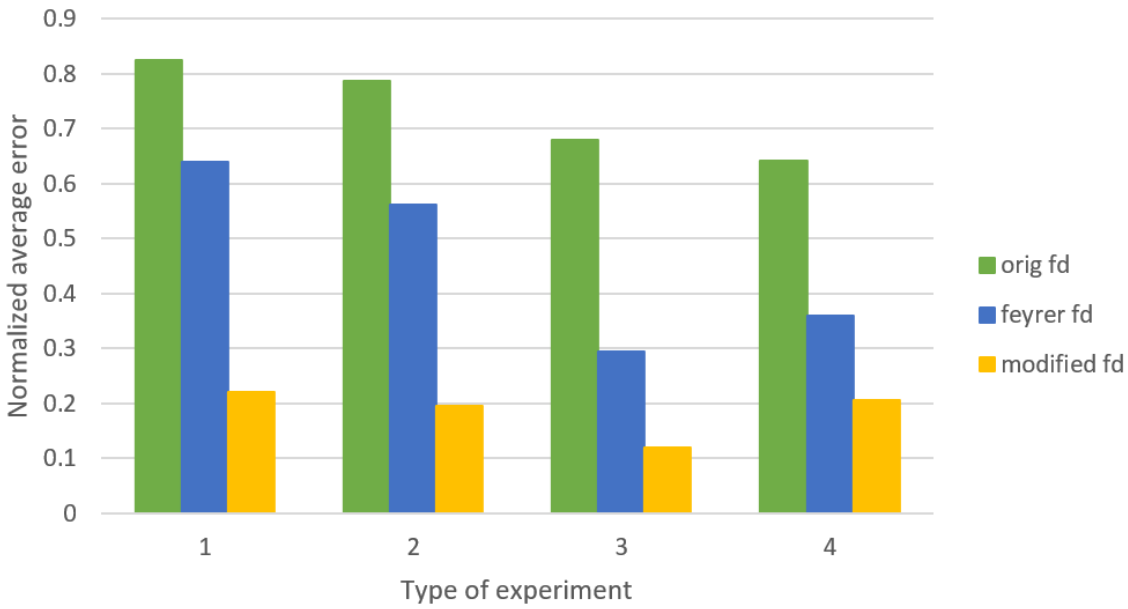


Figure 5.12: Normalized error.

of the wire rope diameter and pulley diameter need to be investigated.

As it can be seen in the Fig. 5.1, some pulleys on the RAVEN II has non-parallel axis. This could be investigated to further understand the BoS fatigue of wire rope.

Even though we only investigated the effect of BoS, the tension-tension fatigue might add extra wear and shorten the wire rope's life in the real robot application.

# Chapter 6

# KINEMATICS OF ROBOSCOPE

## *6.1 Introduction*

Minimally invasive surgery (MIS) provides benefits such as safety (less bleeding and trauma), smaller scars, and faster recovery. The use of a flexible manipulator could extend MIS to more surgical tasks because it can be guided through a limited and non-straight pathway and more sites can be reached without damaging surrounding organs or used for natural orifice transluminal endoscopic surgery (NOTES) which requires no incision.

Many studies of design, analysis, and evaluation of new flexible manipulators with a single instrument (sometimes with endoscope) for NOTES (or MIS in general) have been done [8, 15, 52, 73, 74, 89]. However, a single manipulator is not adequate to perform complex surgical tasks. Research on two arm, high degree of freedom (DOF) flexible manipulators is still limited. Bardou et al. [6] present a two flexible arm (4 mm each) system connected on the sides of a 12 mm diameter classical endoscope. Inaccuracy of the kinematic model was compensated using an external sensor. Lee et al. [45] introduce a single-port robotic surgical platform with 30 mm diameter guide tube. They observed nonlinear backlash and removed it using a feedforward term with backlash inverse. Traeger et al. [80] developed a two arm spine-inspired flexible manipulator. Simulation of the workspace is shown but the kinematic model and its accuracy were not presented. Mechanical problems arising from cable stretch are often discussed but issues with the coupling are not specifically mentioned.

Roboscope (Fig. 6.1) is a two-arm, 12 DOF, fully motorized robot with flexible manipulator designed for skullbase surgery and neurosurgery [69]. It has three major joints and because of the structure, the joints experience strong coupling which could severely affect the kinematics. Therefore, it is important to analyze the geometry and kinematics of the joints

and how they affect each other in order to accurately predict the manipulator's orientation and position from the motor position.

The organization of this chapter is as follows. Section 6.2 introduces the design and structure of the flexible joint. Section 6.3 describes in-depth analysis of the geometry of the joints and the transformation from the actuator space to the Roboscope's task space is presented. Section 6.4 compares the kinematic model obtained in section 6.3 to the experimental data. In section 6.6, conclusions are drawn.

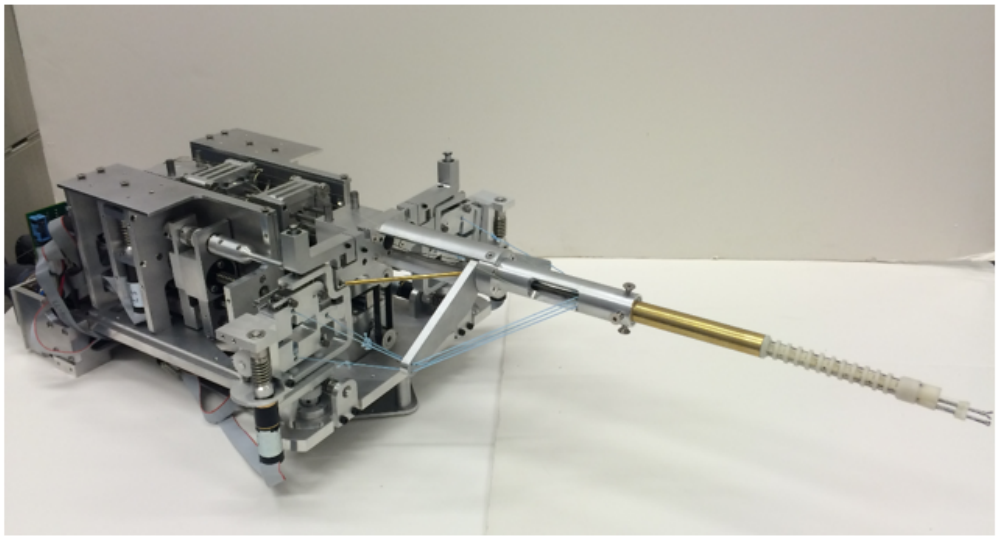

Figure 6.1: Roboscope; fully motorized 12 DOF surgical robot with two arm cable-driven flexible manipulator.

## *6.2 Structure of the Flexible Joint*

The flexible joint consists of three major joints: main directional joint (2 DOFs), tool directional joints ($2 \times 2\ tools = 4$ DOFs) and tool (insertion and rotation) joints ($2 \times 2\ tools = 4$ DOFs). Including the tool open and close for each tool, the roboscope has 12 DOFs in total (Fig. 6.2). Two tool direction joints and two flexible endoscope ports are located at the end of the main directional joint and the tool insertion and rotational joints start at the tip of the tool directional joint. The main directional joint is controlled by the liner displacement

of cable $l_{Dx}$ and $l_{Dy}$. The tool directional joint is actuated by two rotations of the gimbal $\theta_{Gx}$ and $\theta_{Gx}$, and the tool insertion and rotation are controlled by $l_T$ and $\phi_T$ (Fig. 6.3).

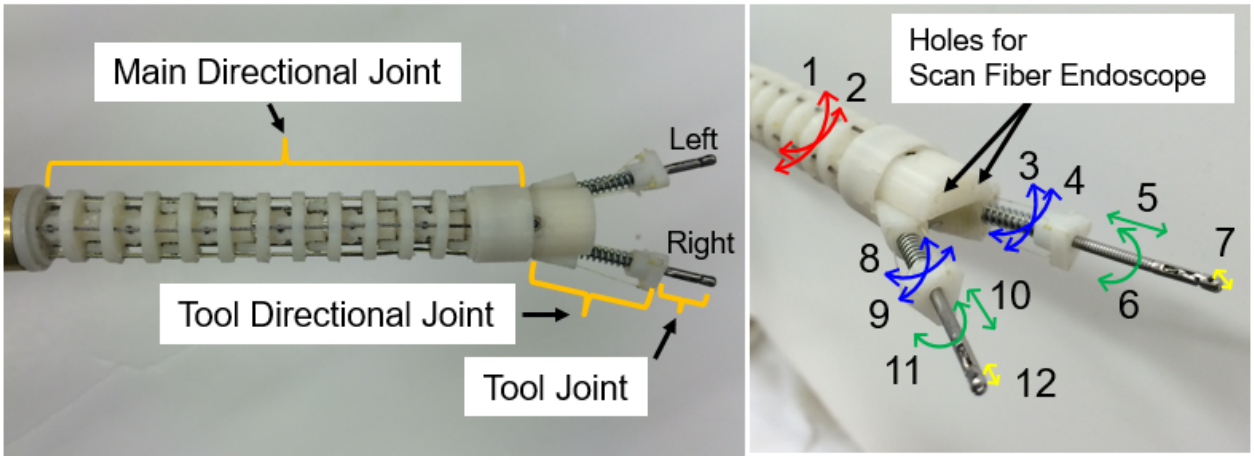


Figure 6.2: Roboscope's flexible joint has 12 DOFs in total. Main directional joint: 1, 2. Tool directional joint: 3, 4 (Left tool) and 8, 9 (Right tool). Tool insertion and rotation: 5, 6 (Left tool) and 10, 11 (Right tool). Tool open and close: 7 (Left tool) and 12 (Right tool).

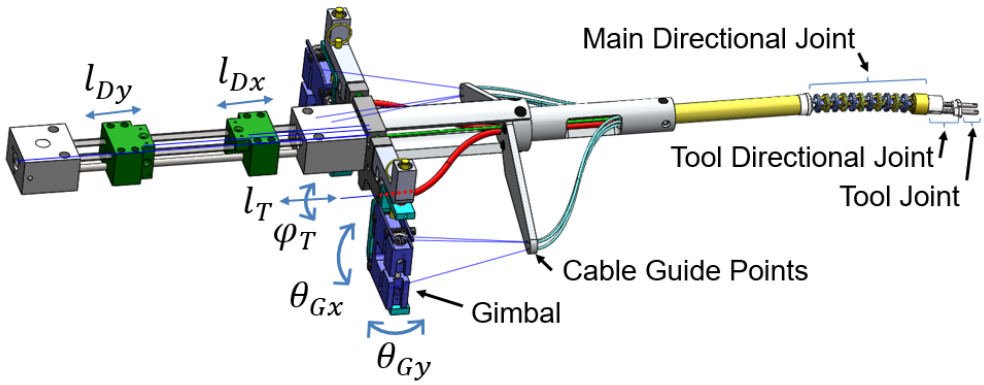


Figure 6.3: Tool assembly. $l_{Dx}$ and $l_{Dy}$ control the main directional joint, $\theta_{Gx}$ and $\theta_{Gx}$ control the tool directional joint and $l_T$ and $\phi_T$ are for the tool insertion and rotation.

The main directional joint is constructed out of serially connected multiple bending segments. Each bending segment has holes allocated for all actuation cables, tools, and scanning

fiber endoscopes (SFE) [44, 90] (Fig. 6.4). This is to avoid high friction and wear that could be caused by tangling and inter-sliding of cables and instruments while the joint is being bent. Moreover, the coupling effect becomes more predictable compared to the case everything goes through a single hole without being constrained. Another reason this design is chosen is that the main directional joint needs to have some rigidity to avoid buckling when it is loaded off-axially (as happens when the tool directional joint is actuated). Currently, the parts for the joints were 3D printed with ABS plastic and the main diameter is 12 mm in order to avoid failure during manipulation. An earlier prototype was built at diameter of 8 mm from segments w/ stamped metal joints. Having such small diameter is necessary for natural orifice trans-nasal and trans-orbital surgeries.

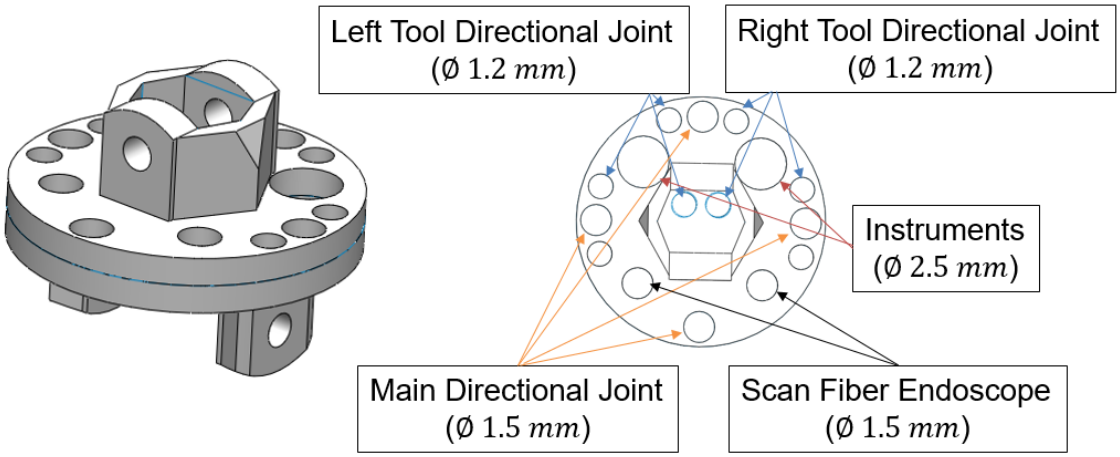


Figure 6.4: Left: One bending segment of main directional joint. Right: Top view of a bending segment. Each segment has holes for all actuation cables, instruments, and scan fiber endoscopes to avoid unpredictable friction caused by tangling and inter wire sliding. The diameter of the segment is 12 mm.

The main component of the tool directional joint is a helical spring covered by a sheath (not shown in the figure) when inserting the flexible joint into patient's body. When operating, the sheath is removed and two tools are separated by a tool separation spring (Fig. 6.5). Triangulation can be achieved by bending both tool directional joints inward (it is necessary to perform surgical tasks). Each of the tool directional joints are driven by three

cables separated by 120 degrees, in order to provide pitch and yaw control (Fig. 6.11).

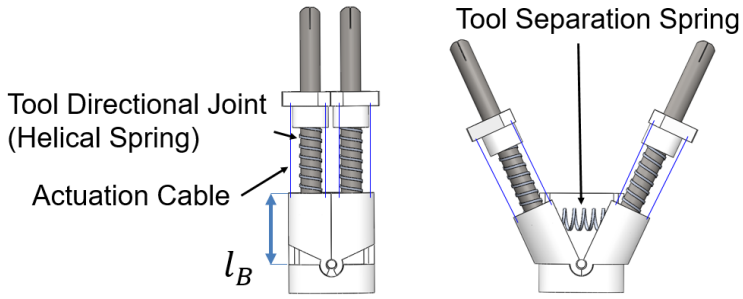


Figure 6.5: Roboscope's tool directional joint. Left: insertion phase with sheath on. Right: operation phase with sheath removed.

## *6.3 Kinematics*

The kinematics of the flexible Roboscope manipulator is represented by mappings between three spaces; actuator, configuration, and task spaces (Fig. 6.6) (there is no configuration space for the tool insertion and rotation because motors with gear reduction directly drive those DOFs). The task space of each joint is calculated individually and all three joint's task spaces are combined to obtain the Roboscope's task space. The motions of the main directional joint, tool directional joint, and tool joint begin with the actuator angles represented as $\theta_{mDx}$ and $\theta_{mDy}$, $\theta_{mGx}$ and $\theta_{mGy}$, and $\theta_{mT}$ and $\theta_{mTR}$ respectively. Based on those angles, the displacement of two main directional joint's actuation cables $l_{Dx}$ and $l_{Dy}$, the gimbal angles $\theta_{Gx}$ and $\theta_{Gy}$, and the tool insertion length $l_T$ and rotation $\phi_T$ are calculated using the gear transmission ratio. Because each actuation cable goes through all the joints before its own and because the cable length inside each joint vary as angles change, the kinematics of the tool directional joint is affected by the main directional joint. Likewise, the kinematics of the tool insertion is affected by both main and tool directional joints. The following subsections investigate the transformation and geometrical relations required to obtain the kinematics of the Roboscope in detail.

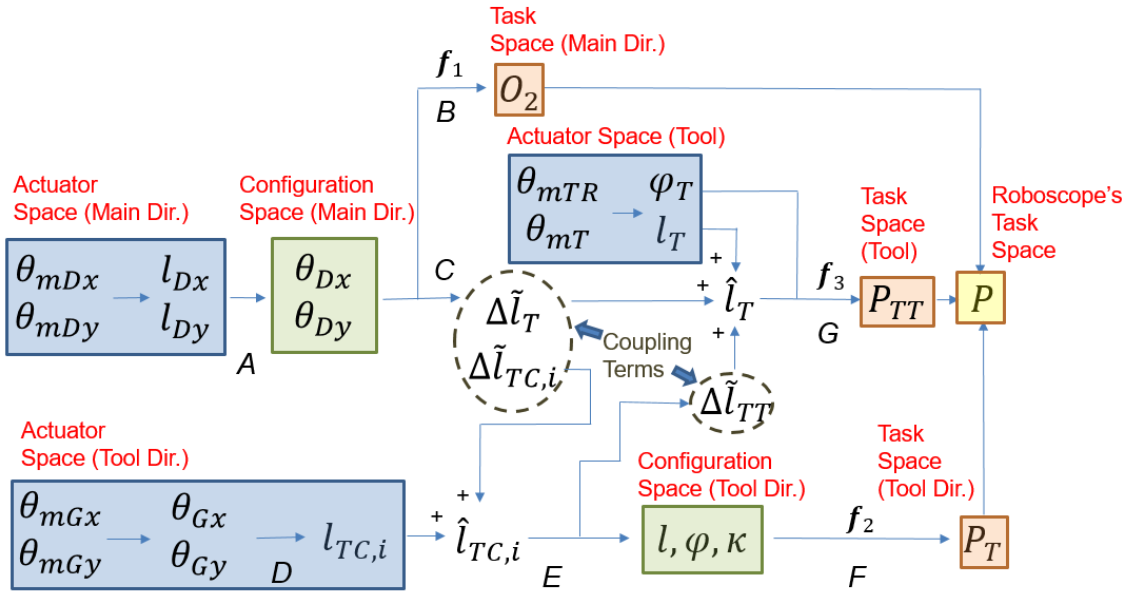


Figure 6.6: Flowchart of obtaining the kinematics of the Roboscope. The transformation between spaces and calculation of coupling terms are discussed in section 6.3.A to G.

### *6.3.1 $l_{Dx}$, $l_{Dy}$ to $\theta_{Dx}$, $\theta_{Dy}$*

The angle of rotation for each segment of the main directional joint is controlled by the linear motion of the cable $l_{Dx}$ and $l_{Dy}$. In order to know the relationship between the cable displacement and the angle of rotation for the main directional joint, the geometry of each main directional joint's segment is investigated. Each segment can be rotated either about x or y axis. Since the x and y rotations are independent (i.e. x-rotation does not affect the length of actuation cable for y-rotation and vice versa), x and y rotations are treated individually. Fig. 6.7 shows how the length of the actuation cable varies when one of the main directional joints is rotated about the y-axis. From the geometrical relation in Fig. 6.8,

$$\theta_{Dy} = \pi - 2\alpha - \beta \tag{6.1}$$

Using the law of cosine, the distance between $D_1$ and $D_1'$ ($|\overline{D_1 D_1'}|$) is written as.

$$|\overline{D_1 D_1'}| = \sqrt{2r^2(1-\cos\beta)} \tag{6.2}$$

Solving eq. (6.2) for $\beta$ gives

$$\beta = \pm\cos\left(1 - \frac{|\overline{D_1 D_1'}|^2}{2r^2}\right) \tag{6.3}$$

Since the range of $\theta_{Dy}$ is limited by the structure ($-30^\circ \leq \theta_{Dy} \leq 30^\circ$), only the positive solution is valid.

If the cable is pulled $l_{Dy}$, with the assumption of the constant-curvature, $|\overline{D_1 D_1'}|$ for each segment is expressed as

$$|\overline{D_1 D_1'}| = d - \frac{l_{Dy}}{N_y} \tag{6.4}$$

where $N_y$ is the number of y-rotation segment. Therefore, in terms of the actuation cable displacement $l_{Dy}$, eq. (6.1) is written as

$$\begin{aligned} \theta_{Dy} &= \pi - 2\alpha - \cos\left(1 - \frac{(d - \frac{l_{Dy}}{N_y})^2}{2r^2}\right) \\ \alpha &= \tan^{-1}\left(\frac{x_{D1}}{d/2}\right) \\ r &= \sqrt{\frac{d^2}{2} + x_{D1}^2} \end{aligned} \tag{6.5}$$

For the x-axis rotation, the relationship between $l_{Dx}$ and $\theta_{Dx}$ is the same as the counterpart of y-rotation. Thus, $\theta_{Dx}$ will be exactly same as eq. (6.5) except that $l_{Dy}$, $N_y$, and $x_{D1}$ are replaced by $l_{Dy}$, $N_x$ (number of x-rotation segment), and $y_{D3}$ (y component of the point $P_3$).

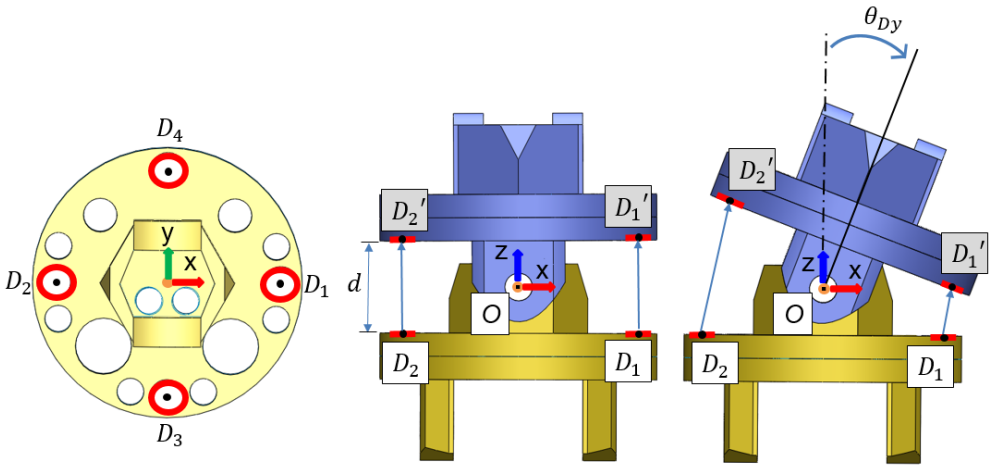


Figure 6.7: One segment of the main directional joint. Left: top view. Middle: x-z plain view. Right: rotated $\theta_{Dy}$ about y-axis. $\theta_{Dy}$ changes as the actuation cables are pulled and the distance $|\overline{D_1D_1'}|$ and $|\overline{D_2D_2'}|$ vary. $|\overline{D_iD_i'}| = d$ when there is no rotation.

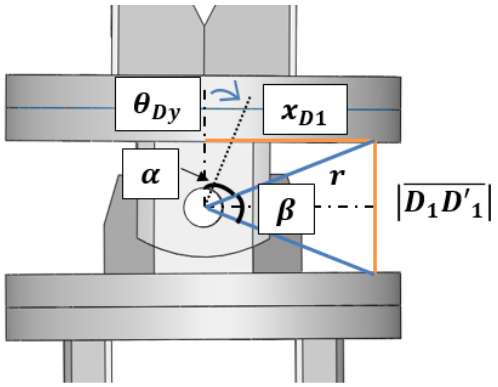


Figure 6.8: Notations assigned for the geometry of one joint segment.

### *6.3.2 $\theta_{Dx}$, $\theta_{Dy}$ to $O_2$*

Denavit-Hartenberg (DH) convention is used for the mapping between $\theta_{Dx}$ $\theta_{Dy}$ and $O_2$ with an assumption that the segments for each x and y rotation rotate equally when cable is actuated. The frame assignment is shown in Fig. 6.9. The distance between each joint frame is denoted $L$. The distance from $O_1$ to the frame of the 1st joint segment is $0.5L$ and from the last (12th) joint segment to $O_2$ is $2L$. The DH parameters of the main directional

joint are in Table 6.1. In order to obtain the kinematics with respect to the base frame $O_1$, the transformation matrix resulting from Table 6.1 (denoted as $T_D$) is pre-multiplied by a transformation matrix. Also, in order to align the frame to $O_2$ including $2L$ translation, the transformation matrix is post-multiplied by another transformation matrix.

$$f_1 = \begin{bmatrix} R_{y(-\frac{\pi}{2})x(-\frac{\pi}{2})} & 0 \\ 0 & 1 \end{bmatrix} T_D \begin{bmatrix} & & 0 \\ R_{x(-\frac{\pi}{2})y(\frac{\pi}{2})z(\frac{\pi}{2})} & & 0 \\ & & 2L \\ 0 & & 1 \end{bmatrix} \tag{6.6}$$

Table 6.1: DH parameter for the main directional joint.

| $i$ | $\alpha_{i-1}$ | $a_{i-1}$ | $d_i$ | $\theta_i$ |
|---|---|---|---|---|
| 1 | 0 | $0.5L$ | 0 | $\theta_{Dy}$ |
| 2 | $\pi/2$ | $L$ | 0 | $\theta_{Dx}$ |
| 3 | $-\pi/2$ | $L$ | 0 | $\theta_{Dy}$ |
| 4 | $\pi/2$ | $L$ | 0 | $\theta_{Dx}$ |
| 5 | $-\pi/2$ | $L$ | 0 | $\theta_{Dy}$ |
| 6 | $\pi/2$ | $L$ | 0 | $\theta_{Dx}$ |
| 7 | $-\pi/2$ | $L$ | 0 | $\theta_{Dy}$ |
| 8 | $\pi/2$ | $L$ | 0 | $\theta_{Dx}$ |
| 9 | $-\pi/2$ | $L$ | 0 | $\theta_{Dy}$ |
| 10 | $\pi/2$ | $L$ | 0 | $\theta_{Dx}$ |
| 11 | $-\pi/2$ | $L$ | 0 | $\theta_{Dy}$ |
| 12 | $\pi/2$ | $L$ | 0 | $\theta_{Dx}$ |

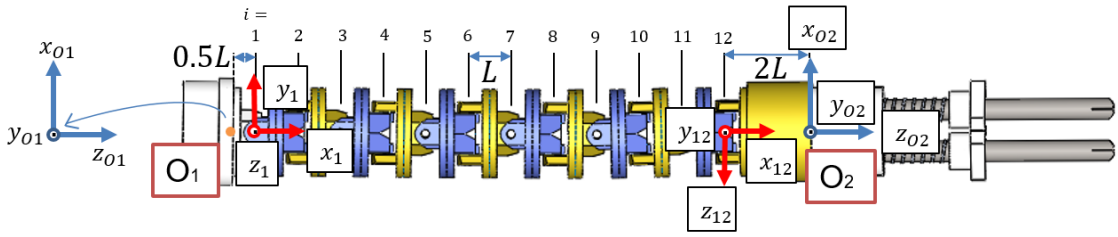


Figure 6.9: Top (x-z plain) view of the Roboscope's flexible joint. The segments with odd index rotate about their z-axis which has the same direction as $z_1$ and the ones with even index rotate about their z-axis which has the same direction as $z_{12}$

### *6.3.3 Coupling terms $\Delta\tilde{l}_{TC,i}$ and $\Delta\tilde{l}_T$*

The motion of the tool directional joint and the tool insertion length is coupled with the main directional joint. Fig. 6.10 shows one segment of the main directional joint with $\theta_{Dy}$ rotation. As it is illustrated, the length of the each actuation joint varies when the main directional joint moves even though the tool directional and tool insertion motors are not actuated. The change in the tool directional joint's actuation cables for each segment caused by y-rotation ($\Delta\tilde{l}_{TCy,i}$ (i = 1,2,3)) is calculated as follows.

$$\Delta\tilde{l}_{TCy,i} = d - |\overline{T_{Ci}T'_{Ci}}|_y \tag{6.7}$$

$$(\overline{T_{Ci}T'_{Ci}})_y = \overline{T_{Ci}O} + R_y(\theta_{Dy})\overline{OT'_{Ci}} \tag{6.8}$$

$$|\overline{T_{Ci}T'_{Ci}}|_y = \Big( \big(x_{TCi}sin(\theta_{Dy}) - x_{TCi} + \frac{dsin(\theta_{Dy})}{2}\big)^2 + \big(\frac{d}{2} - x_{TCi}sin(\theta_{Dy}) + \frac{dsin(\theta_{Dy})}{2}\big)^2 \Big)^{\frac{1}{2}} \tag{6.9}$$

where $x_{TCi}$ is the x component of the point $T_{Ci}$ and $R_y(\theta_{Dy})$ is the rotation matrix for $\theta_{Dy}$ around y-axis. $\theta_{Dy}$ is calculated from the eq. (6.5). For the x-rotation, the change in the actuation cables for each segment becomes

$$\Delta\tilde{l}_{TCx,i} = d - |\overline{T_{Ci}T'_{Ci}}|_x \tag{6.10}$$

$$|\overline{T_{Ci}T'_{Ci}}|_x = \Big( \big(y_{TCi}cos(\theta_{Dx}) - y_{TCi} + \frac{dsin(\theta_{Dx})}{2}\big)^2 + \big(\frac{d}{2} - y_{TCi}sin(\theta_{Dx}) + \frac{dcos(\theta_{Dx})}{2}\big)^2 \Big)^{\frac{1}{2}} \tag{6.11}$$

$y_{TCi}$ is the y component of the point $T_{Ci}$. Since there are $N_x$ and $N_y$ segments for each rotation, the total change in the actuation cable displacement for each actuation cable is

$$\Delta\tilde{l}_{TC,i} = N_y\Delta\tilde{l}_{TCy,i} + N_x\Delta\tilde{l}_{TCx,i} \tag{6.12}$$

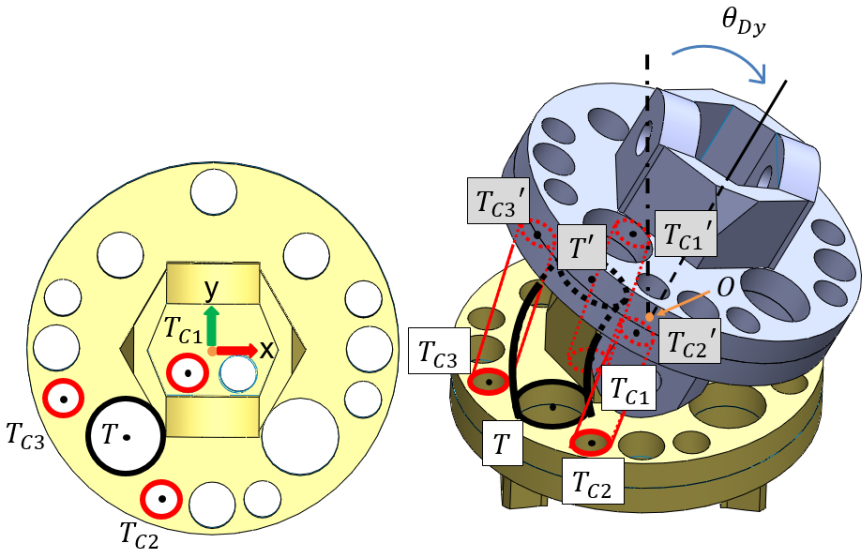


Figure 6.10: One segment of the main directional joint. Left: top view. Right: rotated $\theta_{Dy}$ about y-axis. The segments of the actuation cables are straight lines whereas that of the tool is an arc.

The total change in the tool insertion length is calculated in the same fashion.

$$\Delta\tilde{l}_T = N_y\Delta\tilde{l}_{Ty} + N_x\Delta\tilde{l}_{Tx} \tag{6.13}$$

However, from observation, the tool segment has an arc shape rather than a line when it's bent. Considering the arc shape, the change in the tool insertion length ($\Delta\tilde{l}_{Ty}$ and $\Delta\tilde{l}_{Tx}$) caused by $\theta_{Dy}$ and $\theta_{Dx}$ respectively are calculated as follows.

$$\begin{aligned} \Delta\tilde{l}_{Ty} &= d - l_{Ty} \\ l_{Ty} &= \theta_{Dy}/\kappa_D \\ \kappa_D &= \frac{2cos(\theta_{Dy}/2)}{|\overline{TT'}|_y} \end{aligned} \tag{6.14}$$

and

$$\Delta\tilde{l}_{Tx} = d - \frac{|\overline{TT'}|_x}{2cos(\theta_{Dx}/2)}\theta_{Dx} \tag{6.15}$$

where $\kappa_D$ is the curvature of the arc, $|\overline{TT'}|_y$ and $|\overline{TT'}|_x$ are the distance from $T$ to $T'$ (in Fig. 6.10) for one segment after $\theta_{Dy}$ and $\theta_{Dx}$ rotation.

The roboscope has two instruments. So far, the coupling terms for only one of the tools (eq. (6.12) and (6.13)) are shown but since the calculation procedure is exactly same for both tools, the detailed derivation for the other tool will not be discussed here.

### *6.3.4 $\theta_{Gx}$, $\theta_{Gy}$ to $l_{TC,i}$ and $\hat{l}_{TC,i}$*

The lengths of the three actuation cables for the tool directional joint ($l_{TC,i}$ (i=1,2,3)) are controlled by the motion of the gimbal and swash plate. Therefore, the resultant cable length is written as a function of gimbal angles $\theta_{Gx}$ and $\theta_{Gy}$ as follows.

$$\overline{G_{i,0}P_i} = -G_{i,0} + P_i \tag{6.16}$$

$$\overline{G_iP_i} = -R_y(\theta_{Gy})R_x(\theta_{Gx})G_i + P_i \tag{6.17}$$

$$l_{TC,i} = l_0 - (|\overline{G_iP_i}| - |\overline{G_{i,0}P_i}|) \tag{6.18}$$

where $G_i$ is the point cable is fixed on the gimbal, $G_{i,0}$ is the position of $G_i$ when $\theta_{Gx} = \theta_{Gy} = 0$, $P_i$ is the cable guide point on the tool assembly (Fig. 6.3, 6.11), $R_x$ and $R_y$ are the rotational matrices, and $l_0$ is the initial length of the actuation cables.

As the main directional joint rotates, the length of the actuation cable also varies. This coupling term ($\Delta\tilde{l}_{TC,i}$) is calculated in section 6.3.C. The resultant cable length $\hat{l}_{TC,i}$ with the coupling is expressed as follows.

$$\hat{l}_{TC,i} = l_{TC,i} + \Delta\tilde{l}_{TC,i} \tag{6.19}$$

Since the spring has its minimal (compressed) length ($L_{s,min} = 5mm$) and maximal (natural) length ($L_{s,max} = 9mm$), the resultant cable length is constrained by these values.

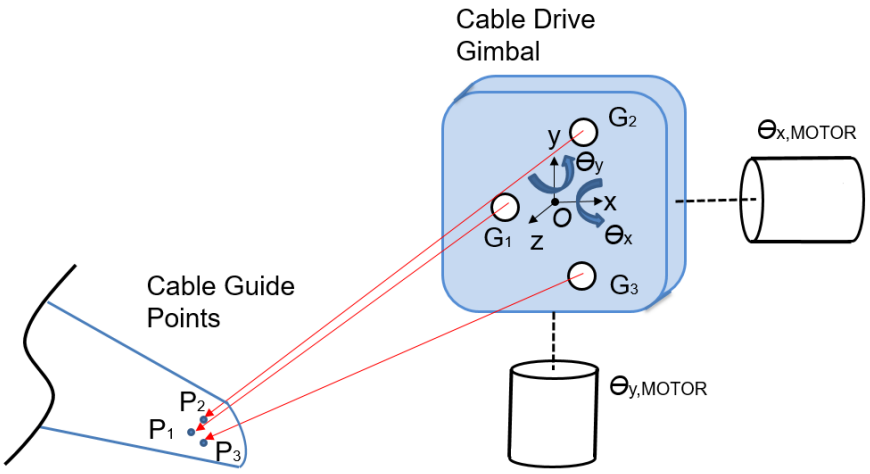


Figure 6.11: Schematic drawing of the gimbal and the cable guide points. Cable length $|\overline{G_iP_i}|$ changes as the gimbal rotates about its x and y axes.

### *6.3.5 $\hat{l}_{TC,i}$ to $l$, $\phi$, $\kappa$, and $\Delta\tilde{l}_{TT}$*

The arc parameters of the tool directional joint in configuration space ($l$, $\phi$, and $\kappa$) are obtained from the lengths of the tool directional joint's actuation cables ($\hat{l}_{TC,i}$). Since the

tool directional joint consists of a helical spring, calculation of the kinematics is performed based on two assumptions presented in [22] and [9]:

1. The center curve of the helical spring is always in a plane.
2. The piecewise curvature of the helical spring is constant.

Besides, it is assumed that the tool separation spring is stiff enough and it will not be compressed while actuating the tool directional joints. Fig. 6.12 illustrates the locations of the actuation cables for the tool directional joint and the relationship between the bending plane of the joint $\phi$ and the actuation cable locations are shown. The arc length $l$, bending plane $\phi$ and curvature of the arc $\kappa$ for the left tool are expressed as follows.

$$l = \frac{\hat{l}_{TC,1} + \hat{l}_{TC,2} + \hat{l}_{TC,3}}{3} \tag{6.20}$$

$$\phi = tan^{-1}\Big(\frac{3(\hat{l}_{TC,3} - \hat{l}_{TC,2})}{\sqrt{3}(\hat{l}_{TC,2} + \hat{l}_{TC,3} - 2\hat{l}_{TC,1})}\Big) \tag{6.21}$$

$$\kappa = \frac{2\sqrt{\hat{l}_{TC,1}^2 + \hat{l}_{TC,2}^2 + \hat{l}_{TC,3}^2 - \hat{l}_{TC,1}\hat{l}_{TC,2} - \hat{l}_{TC,1}\hat{l}_{TC,3} - \hat{l}_{TC,2}\hat{l}_{TC,3}}}{r(\hat{l}_{TC,1} + \hat{l}_{TC,2} + \hat{l}_{TC,3})} \tag{6.22}$$

For the right tool,

$$\phi = tan^{-1}\Big(\frac{3(\hat{l}_{TC,3} - \hat{l}_{TC,1})}{\sqrt{3}(2\hat{l}_{TC,2} - \hat{l}_{TC,3} - \hat{l}_{TC,1})}\Big) \tag{6.23}$$

Note that $\hat{l}_{TC,i}$ are based on the gimbal hole locations defined in Fig. 6.11 which represents the configuration of the left gimbal. Therefore, for the right tool, the frame for the gimbal and the index for the hole location $i$ should be defined such that they match the ones for the tool directional joint and $\hat{l}_{TC,i}$ should be calculated based on that.

The coupling effect $\Delta\tilde{l}_{TT}$ caused by the tool directional joint's motion is simply the difference of the initial spring length $l_s$ and current length of spring.

$$\Delta\tilde{l}_{TT} = l_s - l \tag{6.24}$$

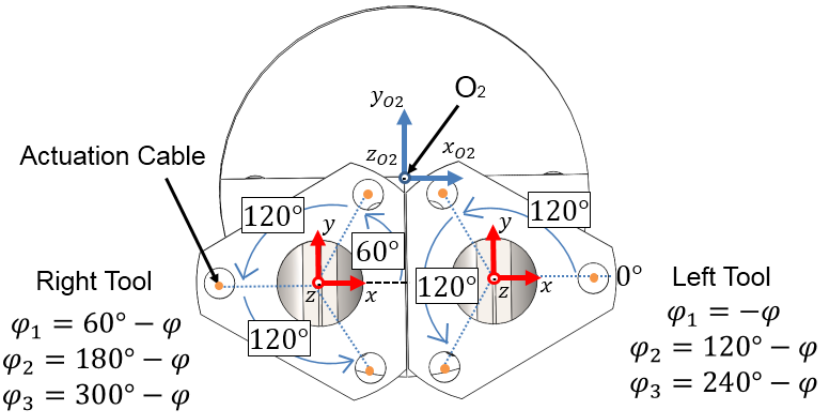


Figure 6.12: Front view (x-y plain) of the flexible manipulator. The actuation cable locations ($\phi_i$(i=1,2,3)) are shown and those locations are related to the bending plane of the joint $\phi$.

### *6.3.6 $l$, $\phi$, and $\kappa$ to $P_T$*

A transformation between configuration space and task space for the tool directional joint can be performed using the robot-independent mapping described in [30] and [84]. With a consideration of aligning the tip frame with the base frame, the transformation matrix is expressed as

$$f = \begin{bmatrix} \cos^2\phi(\cos\kappa l - 1) + 1 & \sin\phi\cos\phi(\cos\kappa l - 1) & \cos\phi\sin\kappa l & \frac{\cos\phi(1-\cos\kappa l)}{\kappa} \\ \sin\phi\cos\phi(\cos\kappa l - 1) & \cos^2\phi(1-\cos\kappa l) + \cos\kappa l & \sin\phi\sin\kappa l & \frac{\sin\phi(1-\cos\kappa l)}{\kappa} \\ -\cos\phi\sin\kappa l & -\sin\phi\sin\kappa l & cos\kappa l & \frac{sin\kappa l}{\kappa} \\ 0 & 0 & 0 & 1 \end{bmatrix} \quad (6.25)$$

During operation, the sheath is removed and the tool directional joints rotate by 20° outward as in Fig. 6.5. Also, there exists offset in x and y axis from $O_2$ to z-axes of both of the tool frames. Therefore, to find out the tool's orientation and position in it's frame, $f_3$ is pre-multiplied by a transformation matrix accordingly.

$$f_2 = \begin{bmatrix} & P_{tx} \\ R_{y(\pm 20^\circ)} & P_{ty} \\ & l_B \\ 0 & 1 \end{bmatrix} f \tag{6.26}$$

where $P_{tx}$ and $P_{ty}$ are the x and y positions of the tool frames with respect to $O_2$ (Fig. 6.12). $l_B$ is the length of the rotating base of the tool directional joint (Fig. 6.5).

### *6.3.7 $P_{TT}$ and Roboscope's Task Space P*

As in Fig. 6.6, the tool's task space $\hat{l}_T$ is

$$\hat{l}_T = l_T + \Delta\tilde{l}_T + \Delta\tilde{l}_{TT} \tag{6.27}$$

There exists an initial offset from the tip of the tool directional joint to the tool joint ($l_{init} = 10mm$). Also, the maximum stroke distance of the tool insertion is $l_{max} = 26mm$). Therefore, the range of $l_T$ is $l_{init} \leq l_T \leq l_{init} + l_{max}$. Besides, the tool can be rotated about its long axis ($\phi_T$). Thus, the transformation from $\hat{l}_T$ to $P_{TT}$ becomes

$$f_3 = \begin{bmatrix} & 0 \\ R_{z(\phi_T)} & 0 \\ & \hat{l}_T \\ 0 & 1 \end{bmatrix} \tag{6.28}$$

Finally, the roboscope's task space $P$ can be obtained by combining all the task spaces $O_2$, $P_T$, and $P_{TT}$.

$$P = f_1 f_2 f_3 \tag{6.29}$$

### *6.4 Experiments and Results*

The kinematic model developed from the previous section was compared with experimental data. Specifically, the pose of all joint when the main directional joint was rotated about its y-axis and x-axis were investigated. In the process, the rotation of the tool directional joint, namely the orientation of the gimbal and the tool insertion were constrained in order to observe the pure coupling effect. For the y-rotation, the positions of the main directional joint ($O_2$), tool directional joints ($P_T$), and tool tip ($P$) for both left and right arms were collected using a sheet with 1 mm grid (Fig. 6.13). From both the model and experiment, no motion in y-axis direction was observed. Therefore, only x-z 2D data will be shown. For the x-rotation, even though the actuation of the main directional joint is planar (y-z plane), the coupling effect causes the arms to bend in the x-axis direction. Hence, the data consist of 3D points. As the left arm and right arm are symmetric about the y-z plane (Fig. 6.17), only the data for the one arm (right arm) was collected.

Fig. 6.14 shows the results for the y-rotation. The positions of the left arm's tool directional joint obtained from the kinematics are the same regardless of the coupling term. This is because the actuation cables for the tool directional joint become slack when extra length is given due to the coupling and they do not push and extend the tool directional joint's spring (this constraint was added to the model). At the first look, for the right arm, the model without the coupling correlates with the experimental data better than the case with the coupling. However, since the error from the main directional joint is added up for the tool directional joint and tool tip, it is difficult to tell which joint caused the error. Therefore, the position of the main directional joint from the experiment was numerically changed to the values obtained from the model. Fig. 6.15 shows the results of the tool directional joint and tool tip after error de-coupling. Errors between the experimental data and the models with and without the coupling are shown in Fig. 6.16. As Table 6.2 indicates, the average error was reduced about 40 - 50% with the coupling terms.

The model and the original results from the x-rotation experiment are shown in Fig. 6.17

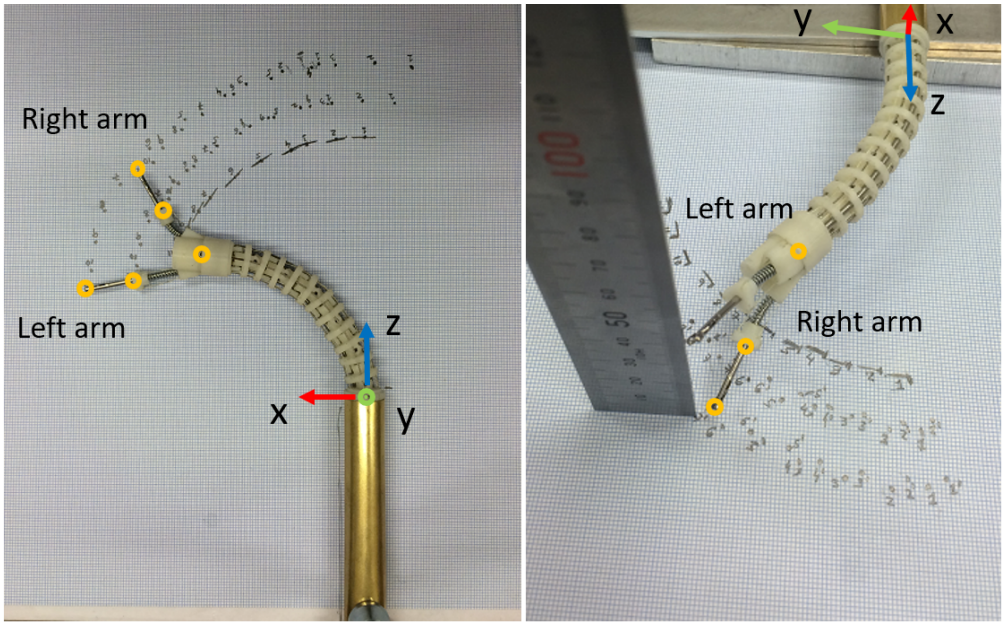


Figure 6.13: The experimental setup to verify the kinematic model. Data in x-z and y-z planar motions were collected using 1 mm grid paper. The positions with the yellow circles were recorded (the positions for the main directional joint were calculated based on the measured points with a constant offset).

and the plots after correcting the error from the main directional joint are shown in Fig. 6.18. The model with coupling is required to capture any of the x-axis motion of the tool directional joint and tool tip which is not captured without the coupling term at all. The coupling effect in the y-z plane is not as significant as it was for the y-rotation. However, the average error was improved by about 30 - 40% due to the coupling term (Fig. 6.19, Table 6.3).

Even with the coupling term, 2-5 mm of error still exists (Table 6.2, 6.3). Due to the uneven friction of each joint section caused by roughness and imperfectness of the 3D printed parts, each section of the main directional joint turns individually. This broke the assumption of the constant curvature and therefore, brought some errors. Besides, stick-slip friction of the actuation cables inside the joints and the complex response of the cable such as non-linear stretch and hysteresis [56] could contribute to more errors.

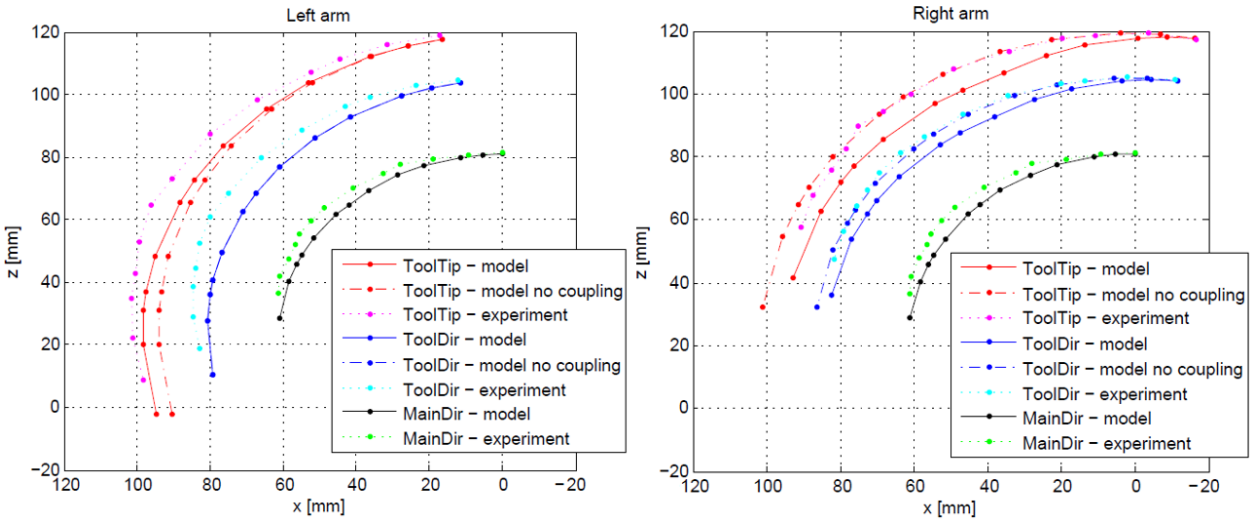


Figure 6.14: Positions of the main directional joint, tool directional joints, and tool top when the main directional joint is rotated about the y axis. Kinematic model with and without coupling term was compared with the experimental data.

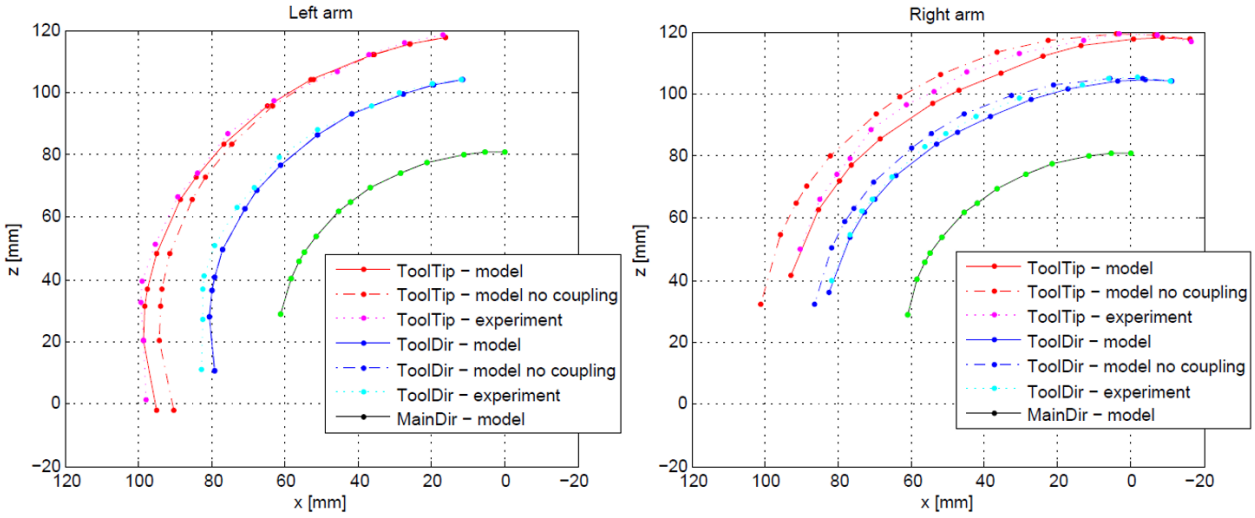


Figure 6.15: Positions of the main directional joint, tool directional joints, and tool top when the main directional joint is rotated about the y axis. Experimentally obtained data were corrected based on the position of the main directional joint obtained from the model.

## *6.5 Workspace*

The workspace of the main directional joint and tool directional joint (left and right) is calculated individually based on kinematics. The base frame of each joint and notations of

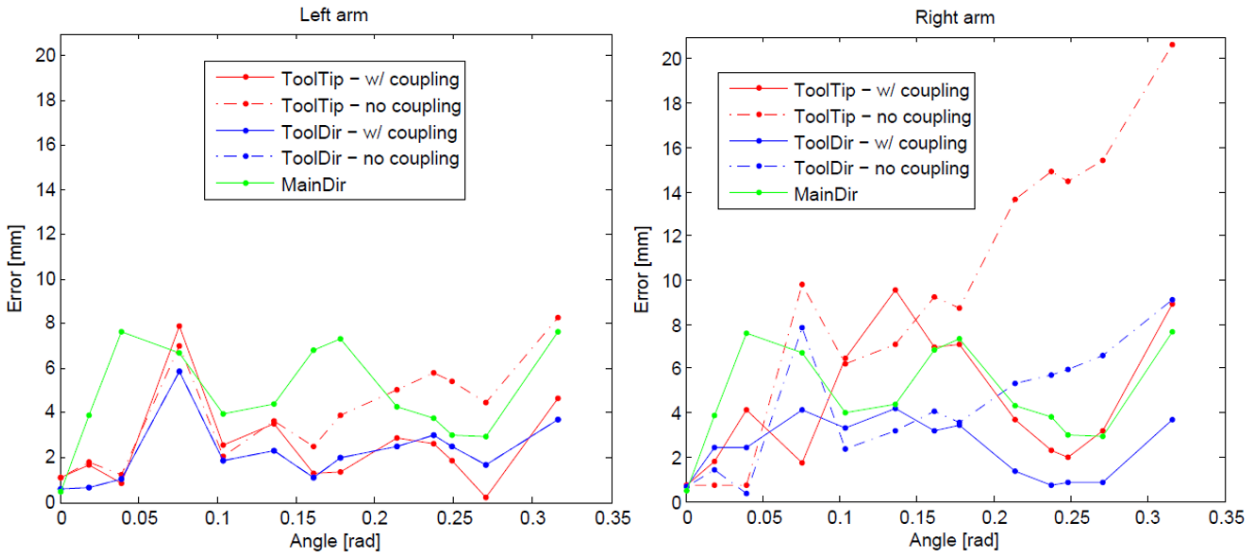


Figure 6.16: The error between the model and the experimental data. The average error is summarized in Table 6.2.

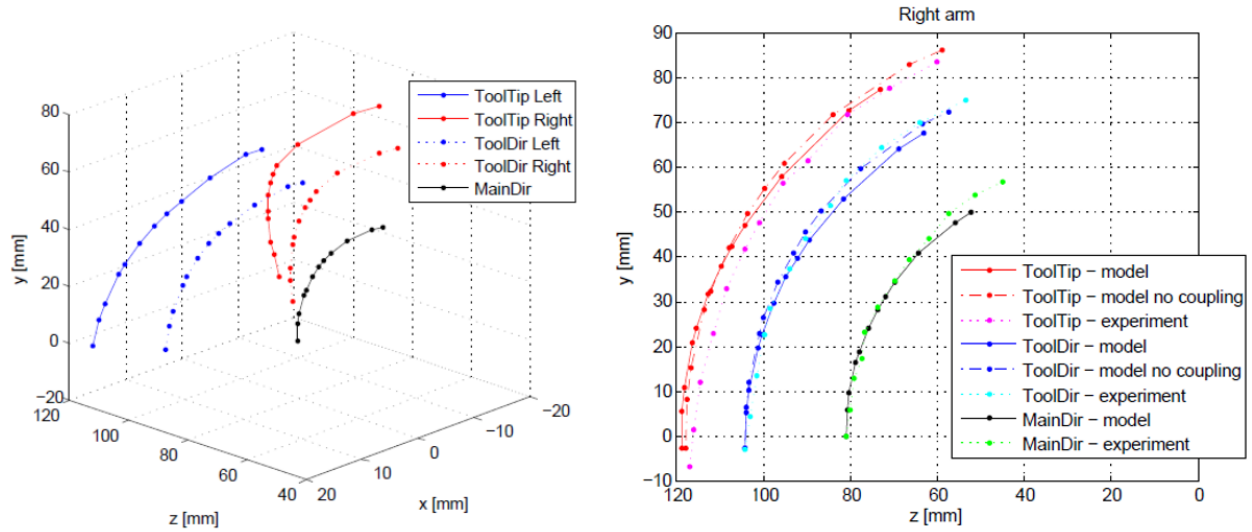


Figure 6.17: Left: Model calculated (with coupling) points of both left and right arms. Right: Positions of the main directional joint, right arm tool directional joint, and right arm tool top when the main directional joint is rotated about the x axis.

Table 6.2: Average error in [mm] and % improvement for the y-rotation experiment.

| | Without Coupling | With Coupling | % Improvement |
|---|---|---|---|
| MainDir | 4.845 | - | - |
| ToolDir Left | 2.221 | 2.221 | 0 |
| ToolTip Left | 4.019 | 2.504 | 37.7 |
| ToolDir Right | 4.324 | 2.407 | 44.3 |
| ToolTip Right | 9.418 | 4.505 | 52.2 |

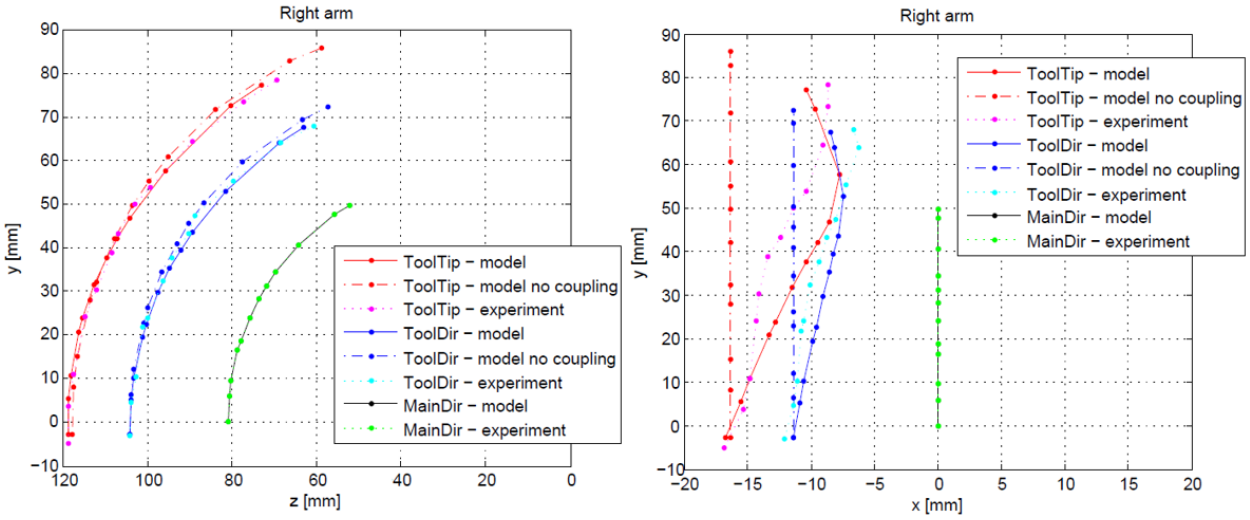


Figure 6.18: y-z plane (left) and x-z plane (right) plots of the model with and without coupling and experimental data after the correction when the main directional joint is rotated about the x axis.

the left and right tool location are assigned as shown in Fig. 6.20.

The main directional joint consists of 12 segments; 6 segments rotate about the x-axis and the other 6 rotate about the y-axis. x and y rotation segments are connected alternately and all segments have a range of motion of ±30 degrees. It is assumed that all segments for each x and y rotation rotate equally and have a constant curvature. Using Denavit-Hartenberg

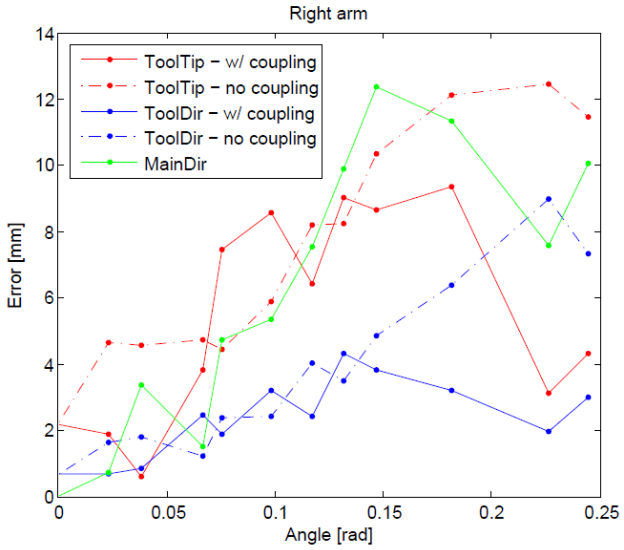


Figure 6.19: The error between the model and the experimental data. The average error is summarized in Table 6.3.

(DH) convention, the kinematics is obtained and the result is shown in Fig. 6.21. Fig. 6.22 shows the shapes of the main directional joint when it is at $P_{M,1}$, $P_{M,2}$, and $P_{M,3}$.

The workspace of the tool directional joint is shown in Fig. 6.23. Pictures of the tool directional joint when the position is $P_{T,1}$, $P_{T,2}$, and $P_{T,3}$ are shown in Fig. 6.24. Since the spring has its minimal (compressed) length ($L_{s,min} = 5mm$) and maximal (natural) length ($L_{s,max} = 9mm$), $\delta l_i$ is constrained by these values.

Calculated and measured angles of the main directional joint at $P_{M,1}$, $P_{M,2}$, $P_{M,3}$ and tool directional joint at $P_{T,1}$, $P_{T,2}$, $P_{T,3}$ are summarized in Table 6.4.

## *6.6 Conclusion*

This chapter presented the calculated and measured kinematics of the Roboscope, a minimally invasive surgical robot with two-arm flexible manipulator, including the coupling effect due to serially connected multiple staged joints. The flexible joint's segments were designed such that all the actuation cables are constrained and cause no unpredictable and excess fric-

Table 6.3: Average error in [mm] and % improvement for the x-rotation experiment.

| | Without Coupling | With Coupling | % Improvement |
|---|---|---|---|
| MainDir | 6.209 | - | - |
| ToolDir Right | 3.771 | 2.371 | 37.1 |
| ToolTip Right | 7.441 | 5.447 | 26.8 |

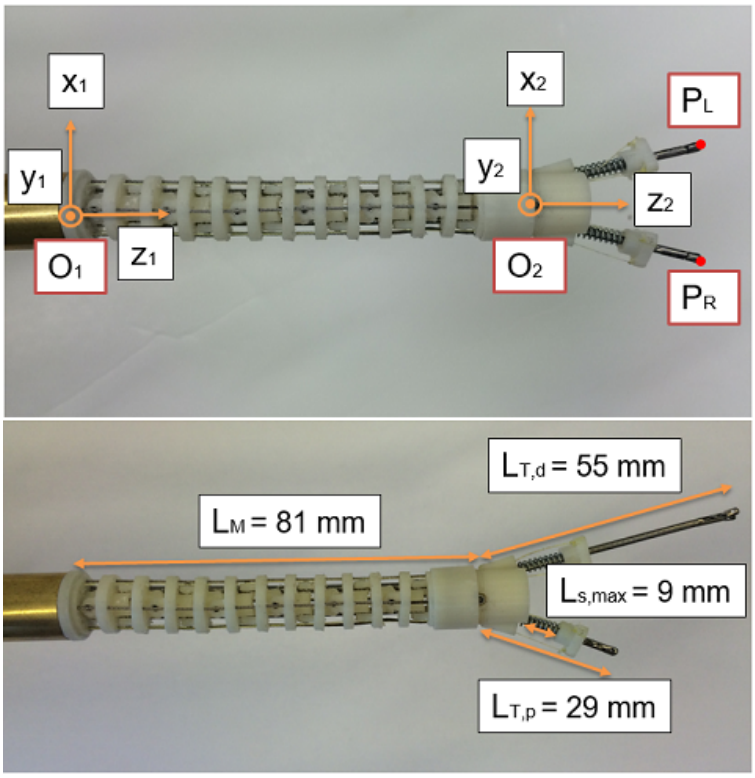


Figure 6.20: Top: Frame assignments for the joints. $z_1$ and $z_2$ are along the center of the main directional joint. Bottom: Lengths of the main directional joint ($L_M$), tool directional joint (at its proximal limit ($L_{T,p}$) and distal limit ($L_{T,d}$)), and spring in the tool directional joint at its natural or maximum length ($L_{s,max}$).

tion. The calculation step and the mappings between actuator space, configuration space, and task space of each part of the joint were shown in detail.

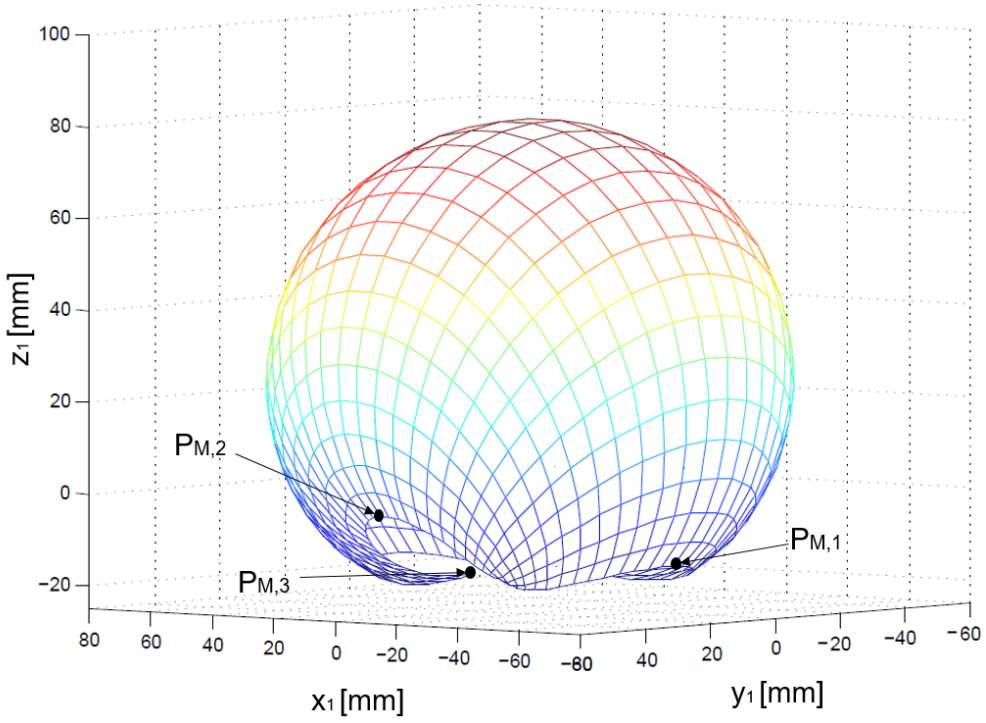


Figure 6.21: Simulation of 2D manifold workspace for the main directional joint. Position of $O_2$ with respect to $O_1$.

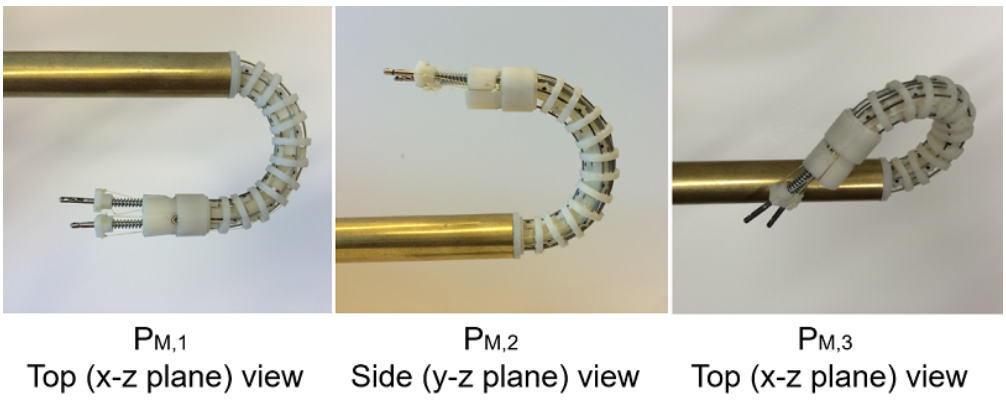


Figure 6.22: Shapes of the main directional joint when the positions are $P_{M,1}$ (left), $P_{M,2}$ (middle), and $P_{M,3}$ (right).

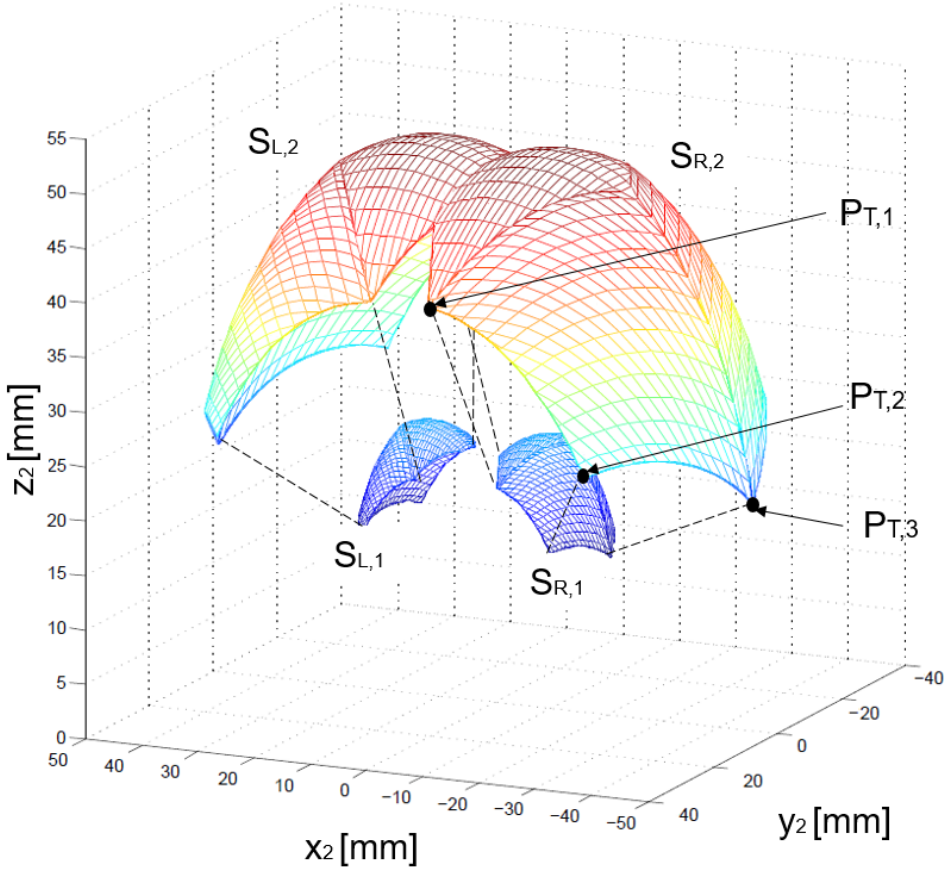


Figure 6.23: Simulation of workspace for the tool directional joint. Positions of the left tool $P_L$ and right tool $P_R$ are with respect to $O_2$. $S_{L,1}$ and $S_{R,1}$ show the workspace when the tools are at the proximal limit and $S_{L,2}$ and $S_{R,2}$ show the workspace when the tools are at the distal limit. The whole workspace of each tool is the space covered by linear projection of inner to outer surface. (i.e. $S_{L,1}$ to $S_{L,2}$ for the left tool and $S_{R,1}$ to $S_{R,2}$ for the right tool).

The experimental result showed that constraining the actuation cables by designing the flexible joint accordingly and modeling the coupling effect improved the position error by 30 - 50% compared to the case ignoring the coupling effect. However, the 3D printed joint segments caused uneven friction throughout the main flexible joint and propagated the error to all the other joints. This friction needs to be reduced by making the joints with higher precision.

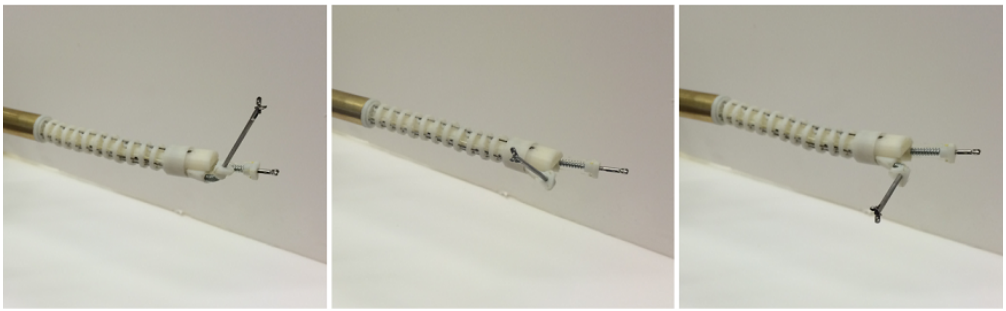


Figure 6.24: Shapes of the tool directional joint when the positions are $P_{T,1}$ (left), $P_{T,2}$ (middle), and $P_{T,3}$ (right).

Table 6.4: Roboscope joint bendable angle.

| | Position | Angle | |
|---|---|---|---|
| | | Calculated | Measured |
| Main Directional Joint | $P_{M,1}$ | 180° | 180° |
| | $P_{M,2}$ | 256° | 251° |
| | $P_{M,3}$ | 180° | 180° |
| Tool Directional Joint | $P_{T,1}$ | 51.7° | 52° |
| | $P_{T,2}$ | 51.3° | 51° |
| | $P_{T,3}$ | 51.7° | 50° |

In order to further improve the accuracy, errors caused by stick-slip friction of the actuation cables inside the flexible joint as well as complex cable behavior including non-linear stretch and hysteresis need to be studied and compensated.

The workspace for the main and tool directional joint is obtained individually. Since there are effect of coupling, the presented workspace for the tool directional joint is correct only when the main directional joint is straight. When the main directional joint is bent, the tool directional joint's workspace deviates from the one presented.

# BIBLIOGRAPHY

[1] Steel wire rope bending cycle fatigue. part one-bending cycle counting. http://www.marineengineering.org.uk/page108.html. Accessed: 2017-02-15.

[2] Farzaneh Abdollahi, Heidar A Talebi, and Rajnikant V Patel. A stable neural network-based observer with application to flexible-joint manipulators. *IEEE Transactions on Neural Networks*, 17(1):118–129, 2006.

[3] Farid Al-Bender. Fundamentals of friction modeling. In *Proceedings, ASPE Spring Topical Meeting on Control of Precision Systems, MIT, April 11-13, 2010*, pages 117–122. ASPE-The American Society of precision Engineering, 2010.

[4] Sören Andersson, Anders Söderberg, and Stefan Björklund. Friction models for sliding dry, boundary and mixed lubricated contacts. *Tribology international*, 40(4):580–587, 2007.

[5] Farshad Anooshahpour, Ilia G Polushin, and Rajni V Patel. Quasi-static modeling of the da vinci instrument. In *Intelligent Robots and Systems (IROS 2014), 2014 IEEE/RSJ International Conference on*, pages 1308–1313. IEEE, 2014.

[6] Berengere Bardou, Philippe Zanne, Florent Nageotte, and Michel de Mathelin. Control of a multiple sections flexible endoscopic system. In *Intelligent Robots and Systems (IROS), 2010 IEEE/RSJ International Conference on*, pages 2345–2350. IEEE, 2010.

[7] R Bouc. Forced vibration of mechanical systems with hysteresis. In *Proceedings of the fourth conference on non-linear oscillation, Prague, Czechoslovakia*, 1967.

[8] David B Camarillo, Christopher F Milne, Christopher R Carlson, Michael R Zinn, and J Kenneth Salisbury. Mechanics modeling of tendon-driven continuum manipulators. *IEEE Transactions on Robotics*, 24(6):1262–1273, 2008.

[9] Kun Cao, Rongjie Kang, Junguo Wang, Zhibin Song, and Jian Dai. Kinematic model and workspace analysis of tendon-driven continuum robots. In *Proceedings of the 14th IFToMM World Congress*, pages 640–644. , 2015.

[10] Ryan James Caverly and James Richard Forbes. State estimator design for a single degree of freedom cable-actuated system. *Journal of the Franklin Institute*, 353(18):4845–4869, 2016.

[11] C Richard Chaplin and Andrew E Potts. Wire rope offshore-a critical review of wire rope endurance research affecting offshore applications. 1991.

[12] CR Chaplin. The fatigue and degradation mechanisms of hoisting ropes. In *Hoist and Haul Conference Perth, WA*, pages 5–7, 2005.

[13] AE Charalampakis and VK Koumousis. On the response and dissipated energy of bouc–wen hysteretic model. *Journal of Sound and Vibration*, 309(3):887–895, 2008.

[14] Quanzhu Chen, Weihai Chen, Rong Liu, and Jianbin Zhang. Error analysis and flexibility compensation of a cable-driven humanoid-arm manipulator. In *Robotics and Automation (ICRA), 2011 IEEE International Conference on*, pages 988–993. IEEE, 2011.

[15] James Clark, David P Noonan, Valentina Vitiello, Mikael H Sodergren, Jianzhong Shang, Christopher J Payne, Thomas P Cundy, Guang-Zhong Yang, and Ara Darzi. A novel flexible hyper-redundant surgical robot: prototype evaluation using a single incision flexible access pelvic application as a clinical exemplar. *Surgical endoscopy*, 29(3):658–667, 2015.

[16] PR Dahl. A solid friction model. Technical report, DTIC Document, 1968.

[17] TN Do, T Tjahjowidodo, MWS Lau, T Yamamoto, and SJ Phee. Hysteresis modeling and position control of tendon-sheath mechanism in flexible endoscopic systems. *Mechatronics*, 24(1):12–22, 2014.

[18] TN Do, Tegoeh Tjahjowidodo, Michael Wai Shing Lau, and Soo Jay Phee. An investigation of friction-based tendon sheath model appropriate for control purposes. *Mechanical Systems and Signal Processing*, 42(1):97–114, 2014.

[19] Pierre Duhem. *Die dauernden Änderungen und die Thermodynamik: IX*. Engelmann, 1903.

[20] Klaus Feyrer. *Wire ropes*. Springer, 2007.

[21] Gerald M Fried. Fls assessment of competency using simulated laparoscopic tasks. *Journal of Gastrointestinal Surgery*, 12(2):210–212, 2008.

[22] Bingtuan Gao, Jianguo Zhao, Ning Xi, and Jing Xu. Combined kinematic and static analysis of a cable-driven manipulator with a spring spine. In *Robotics and Automation (ICRA), 2011 IEEE International Conference on*, pages 2725–2730. IEEE, 2011.

[23] PT Gibson, FG White, LA Schalit, RE Thomas, RW Cote, and HA Cress. A study of parameters that influence wire-rope fatigue life. Technical report, DTIC Document, 1974.

[24] Marco Giglio and A Manes. Life prediction of a wire rope subjected to axial and bending loads. *Engineering Failure Analysis*, 12(4):549–568, 2005.

[25] Marc Gouttefarde, Dinh Quan Nguyen, and Cédric Baradat. Kinetostatic analysis of cable-driven parallel robots with consideration of sagging and pulleys. In *Advances in Robot Kinematics*, pages 213–221. Springer, 2014.

[26] Mohammad Haghighipanah, Yangming Li, Muneaki Miyasaka, and Blake Hannaford. Improving position precision of a servo-controlled elastic cable driven surgical robot using unscented kalman filter. In *Intelligent Robots and Systems (IROS), 2015 IEEE/RSJ International Conference on*, pages 2030–2036. IEEE, 2015.

[27] Mohammad Haghighipanah, Muneaki Miyasaka, Yangming Li, and Blake Hannaford. Unscented kalman filter and 3d vision to improve cable driven surgical robot joint angle estimation. In *2016 IEEE International Conference on Robotics and Automation (ICRA)*, pages 4135–4142. IEEE, 2016.

[28] Mohhamad Haghighipanah, Yangming Li, Muneaki Miyasaka, and Blake Hannaford. Improving position precision of a servo-controlled elastic cable driven surgical robot using unscented kalman filter. In *Intelligent Robots and Systems (IROS), 2015 IEEE International Conference on*. IEEE, 2015 in Press.

[29] Blake Hannaford, Jacob Rosen, Diana W Friedman, Hawkeye King, Phillip Roan, Lei Cheng, Daniel Glozman, Ji Ma, Sina Nia Kosari, and Lee White. Raven-ii: an open platform for surgical robotics research. *Biomedical Engineering, IEEE Transactions on*, 60(4):954–959, 2013.

[30] Michael W Hannan and Ian D Walker. Kinematics and the implementation of an elephant's trunk manipulator and other continuum style robots. *Journal of Field Robotics*, 20(2):45–63, 2003.

[31] John Henry Holland. *Adaptation in natural and artificial systems: an introductory analysis with applications to biology, control, and artificial intelligence*. MIT press, 1992.

[32] Danying Hu, Yuanzheng Gong, Blake Hannaford, and Eric J Seibel. Semi-autonomous simulated brain tumor ablation with ravenii surgical robot using behavior tree. In *Robotics and Automation (ICRA), 2015 IEEE International Conference on*, pages 3868–3875. IEEE, 2015.

[33] Danying Hu, Yuanzheng Gong, Blake Hannaford, and Eric. J Seibel. Semi-autonomous simulated brain tumor ablation with raven ii robot using behavior tree. In *Robotics and Automation (ICRA), 2015 IEEE International Conference on*. IEEE, 2015 in Press.

[34] Ben Kehoe, Gregory Kahn, Jeffrey Mahler, Jonathan Kim, Alex Lee, Anna Lee, Keisuke Nakagawa, Sachin Patil, W Douglas Boyd, Pieter Abbeel, et al. Autonomous multilateral debridement with the raven surgical robot. In *International Conference on Robotics and Automation*, 2014.

[35] MA Khosravi and HD Taghirad. Robust pid control of cable-driven robots with elastic cables. In *Robotics and Mechatronics (ICRoM), 2013 First RSI/ISM International Conference on*, pages 331–336. IEEE, 2013.

[36] Mohammad A Khosravi and Hamid D Taghirad. Robust pid control of fully-constrained cable driven parallel robots. *Mechatronics*, 24(2):87–97, 2014.

[37] Chi Yen Kim, Min Cheol Lee, Ryan Blaine Wicker, and Sung-Min Yoon. Dynamic modeling of coupled tendon-driven system for surgical robot instrument. *International Journal of Precision Engineering and Manufacturing*, 15(10):2077–2084, 2014.

[38] Hiroyuki Kimura, Tomoki Iijima, Shigenori Matsuo, and Yoshiaki Fujita. Vibration analysis of elevator rope (comparison between experimental results and calculated results). *Journal of System Design and Dynamics*, 3(3):420–428, 2009.

[39] Hawkeye King. Sina nia kosari. *Blake Hannaford, Ji Ma,Kinematic Analysis of the Raven-IITM Research Surgical Robot Platform., UWEE (University of Washington Electrical Engineering) Technical Report Number UWEETR*, 2012.

[40] Sina Nia Kosari, Srikrishnan Ramadurai, Howard Jay Chizeck, and Blake Hannaford. Control and tension estimation of a cable driven mechanism under different tensions. In *ASME 2013 International Design Engineering Technical Conferences and Computers and Information in Engineering Conference*, pages V06AT07A077–V06AT07A077. American Society of Mechanical Engineers, 2013.

[41] Werner Kraus, Michael Kessler, and Andreas Pott. Pulley friction compensation for winch-integrated cable force measurement and verification on a cable-driven parallel robot. In *Robotics and Automation (ICRA), 2015 IEEE International Conference on*, pages 1627–1632. IEEE, 2015.

[42] Werner Kraus, Valentin Schmidt, Puneeth Rajendra, and Andreas Pott. System identification and cable force control for a cable-driven parallel robot with industrial servo drives. In *International conference on robotics and automation (ICRA)*, 2014.

[43] Anthony R Lanfranco, Andres E Castellanos, Jaydev P Desai, and William C Meyers. Robotic surgery: a current perspective. *Annals of surgery*, 239(1):14, 2004.

[44] Cameron M Lee, Christoph J Engelbrecht, Timothy D Soper, Fritjof Helmchen, and Eric J Seibel. Scanning fiber endoscopy with highly flexible, 1-mm catheterscopes for wide-field, full-color imaging. *Journal of biophotonics*, 3(5-6):385, 2010.

[45] Jusuk Lee, Jiyoung Kim, Kwang-Kyu Lee, Seungyong Hyung, Yong-Jae Kim, Woong Kwon, Kyungshik Roh, and Jung-Yun Choi. Modeling and control of robotic surgical platform for single-port access surgery. In *Intelligent Robots and Systems (IROS 2014), 2014 IEEE/RSJ International Conference on*, pages 3489–3495. IEEE, 2014.

[46] Tae-Kyung Lee, Chi-Yen Kim, and Min Cheol Lee. Friction analysis according to pretension of laparoscopy surgical robot instrument. *International Journal of Precision Engineering and Manufacturing*, 12(2):259–266, 2011.

[47] Andrew Lewis. Block transfer cable data. 2013.

[48] Yangming Li, Muneaki Miyasaka, Mohammad Haghighipanah, Lei Cheng, and Blake Hannaford. Dynamic modeling of cable driven elongated surgical instruments for sensorless grip force estimation. In *2016 IEEE International Conference on Robotics and Automation (ICRA)*, pages 4128–4134. IEEE, 2016.

[49] Ning Liu, Christos Bergeles, and Guang-Zhong Yang. Design and analysis of a wire-driven flexible manipulator for bronchoscopic interventions. In *Robotics and Automation (ICRA), 2016 IEEE International Conference on*, pages 4058–4063. IEEE, 2016.

[50] Jeffrey Mahler, Sanjay Krishnan, Michael Laskey, Siddarth Sen, Adithyavairavan Murali, Ben Kehoe, Sachin Patil, Jiannan Wang, Mike Franklin, Pieter Abbeel, et al. Learning accurate kinematic control of cable-driven surgical robots using data cleaning and gaussian process regression.

[51] Jeffrey Mahler, Sridhar Krishnan, Michael Laskey, Satyaki Sen, Adithyavairavan Murali, Ben Kehoe, Swapnil Patil, Jiannan Wang, Matthew Franklin, Pieter Abbeel, et al. Learning accurate kinematic control of cable-driven surgical robots using data cleaning and gaussian process regression. In *Automation Science and Engineering (CASE), 2014 IEEE International Conference on*, pages 532–539. IEEE, 2014.

[52] Jacques Marescaux, Bernard Dallemagne, Silvana Perretta, Arnaud Wattiez, Didier Mutter, and Dimitri Coumaros. Surgery without scars: report of transluminal cholecystectomy in a human being. *Archives of surgery*, 142(9):823–826, 2007.

[53] Georg Masing. Zur heynschen theorie der verfestigung der metalle durch verborgen elastische spannungen. In *Wissenschaftliche Veröffentlichungen aus dem Siemens-Konzern*, pages 231–239. Springer, 1923.

[54] Jean-Pierre Merlet. The influence of discrete-time control on the kinematico-static behavior of cable-driven parallel robot with elastic cables. In *Advances in Robot Kinematics*, pages 113–121. Springer, 2014.

[55] Chowarit Mitsantisuk, Kiyoshi Ohishi, and Seiichiro Katsura. Control of interaction force of twin direct-drive motor system using variable wire rope tension with multisensor integration. *IEEE Transactions on Industrial Electronics*, 59(1):498–510, 2012.

[56] Muneaki Miyasaka, Mohammad Haghighipanah, Yangming Li, and Blake Hannaford. Hysteresis model of longitudinally loaded cable for cable driven robots and identification of the parameters. In *Robotics and Automation (ICRA), 2016 IEEE International Conference on*, pages 4051–4057. IEEE, 2016.

[57] Muneaki Miyasaka, Joseph Matheson, Andrew Lewis, and Blake Hannaford. Measurement of the cable-pulley coulomb and viscous friction for a cable-driven surgical robotic system. In *Intelligent Robots and Systems (IROS), 2015 IEEE/RSJ International Conference on*, pages 804–810. IEEE, 2015.

[58] Muneaki Miyasaka, Joseph Matheson, Andrew Lewis, and Blake Hannaford. Measurement of the cable-pulley coulomb and viscous friction for a cable-driven surgical robotic system. In *Intelligent Robots and Systems (IROS), 2015 IEEE International Conference on*. IEEE, 2015 in Press.

[59] Edvard Naerum, Hawkeye HI King, and Blake Hannaford. Robustness of the unscented kalman filter for state and parameter estimation in an elastic transmission. In *Robotics: Science and Systems*, 2009.

[60] YQ Ni, JM Ko, CW Wong, and S Zhan. Modelling and identification of a wire-cable vibration isolator via a cyclic loading test. *Proceedings of the Institution of Mechanical Engineers, Part I: Journal of Systems and Control Engineering*, 213(3):163–172, 1999.

[61] H Nijmeijer and Ir R HB Fey TUE. Modelling and identification of the dynamic behavior of a wire rope spring.

[62] Henrik Olsson, Karl J Åström, C Canudas De Wit, Magnus Gäfvert, and Pablo Lischinsky. Friction models and friction compensation. *European journal of control*, 4(3):176–195, 1998.

[63] YA Onur and CE İmrak. The influence of rotation speed on the bending fatigue lifetime of steel wire ropes. *Proceedings of the Institution of Mechanical Engineers, Part C: Journal of Mechanical Engineering Science*, 225(3):520–525, 2011.

[64] Cong Bang Pham, Huat Yeo, Guilin Yang, Mustafa Shabbir Kurbanhusen, I Chen, et al. Force-closure workspace analysis of cable-driven parallel mechanisms. *Mechanism and Machine Theory*, 41(1):53–69, 2006.

[65] Srikrishnan Ramadurai, Sina Nia Kosari, H Hawkeye King, Howard Jay Chizeck, and Blake Hannaford. Application of unscented kalman filter to a cable driven surgical robot: A simulation study. In *Robotics and Automation (ICRA), 2012 IEEE International Conference on*, pages 1495–1500. IEEE, 2012.

[66] Mohammed Raoof and Ivana Kraincanic. Determination of wire recovery length in steel cables and its practical applications. *Computers & structures*, 68(5):445–459, 1998.

[67] Austin Reiter, Peter K Allen, and Tao Zhao. Appearance learning for 3d tracking of robotic surgical tools. *The International Journal of Robotics Research*, page 0278364913507796, 2013.

[68] I ML Ridge, J Zheng, and CR Chaplin. Measurement of cyclic bending strains in steel wire rope. *The Journal of Strain Analysis for Engineering Design*, 35(6):545–558, 2000.

[69] Jacob Rosen, Laligam N. Sekhar, Daniel Glozman, Muneaki Miyasaka, Jesse Dosher, Brian Dellon, Kris S. Moe, Aylin Kim, Louis J. Kim, Thomas Lendvay, Yangming Li, and Blake Hannaford. Roboscope: A flexible and bendable surgical robot for single portal minimally invasive surgery. In *Robotics and Automation (ICRA), 2017 IEEE International Conference on*. IEEE, 2017.

[70] Kenneth Salisbury, William Townsend, B Ebrman, and David DiPietro. Preliminary design of a whole-arm manipulation system (wams). In *Robotics and Automation, 1988. Proceedings., 1988 IEEE International Conference on*, pages 254–260. IEEE, 1988.

[71] Daniel Sauter. *Modeling the dynamic characteristics of slack wire cables in Stockbridge dampers*. PhD thesis, TU Darmstadt, 2004.

[72] W Schwanen. Modelling and identification of the dynamic behavior of a wire rope spring. *Technische Universiteit Eindhoven*, 2004.

[73] Carlo A Seneci, Jianzhong Shang, Konrad Leibrandt, Valentina Vitiello, Nisha Patel, Ara Darzi, Julian Teare, and Guang-Zhong Yang. Design and evaluation of a novel flexible robot for transluminal and endoluminal surgery. In *Intelligent Robots and Systems*

*(IROS 2014), 2014 IEEE/RSJ International Conference on*, pages 1314–1321. IEEE, 2014.

[74] Jianzhong Shang, David P Noonan, C Payne, James Clark, Mikael Hans Sodergren, Ara Darzi, and G-Z Yang. An articulated universal joint based flexible access robot for minimally invasive surgery. In *Robotics and Automation (ICRA), 2011 IEEE International Conference on*, pages 1147–1152. IEEE, 2011.

[75] Edward R Snow. *The load/deflection behavior of pretensioned cable/pulley transmission mechanisms*. PhD thesis, Massachusetts Institute of Technology and Woods Hole Oceanographic Institution, 1993.

[76] Junho Song and Armen Der Kiureghian. Generalized bouc–wen model for highly asymmetric hysteresis. *Journal of engineering mechanics*, 132(6):610–618, 2006.

[77] Kaitlin Spak, Gregory Agnes, and Daniel Inman. Cable modeling and internal damping developments. *Applied Mechanics Reviews*, 65(1):010801, 2013.

[78] DS Tchankov and KV Vesselinov. Fatigue life prediction under random loading using total hysteresis energy. *International journal of pressure vessels and piping*, 75(13):955–960, 1998.

[79] William Thomas Townsend. The effect of transmission design on force-controlled manipulator performance. 1988.

[80] Mattias F Traeger, Daniel B Roppenecker, Matthias R Leininger, Florian Schnoes, and Tim C Lueth. Design of a spine-inspired kinematic for the guidance of flexible instruments in minimally invasive surgery. In *Intelligent Robots and Systems (IROS 2014), 2014 IEEE/RSJ International Conference on*, pages 1322–1327. IEEE, 2014.

[81] Mikel Aingeru Urchegui, Wilson Tato, and Xabier Gómez. Wear evolution in a stranded rope subjected to cyclic bending. *Journal of Materials Engineering and Performance*, 17(4):550–560, 2008.

[82] Augusto Visintin. Mathematical models of hysteresis. *The science of hysteresis*, 1:1–114, 2006.

[83] Augusto Visintin. *Differential models of hysteresis*, volume 111. Springer Science & Business Media, 2013.

[84] Robert J Webster III and Bryan A Jones. Design and kinematic modeling of constant curvature continuum robots: A review. *The International Journal of Robotics Research*, 29(13):1661–1683, 2010.

[85] Yi-Kwei Wen. Method for random vibration of hysteretic systems. *Journal of the Engineering Mechanics Division*, 102(2):249–263, 1976.

[86] Erik Wernholt and Stig Moberg. Nonlinear gray-box identification using local models applied to industrial robots. *Automatica*, 47(4):650–660, 2011.

[87] Wirerope Works, Inc. Technical bulletin no. 10 - sheaves & grooves. http://www.wwwrope.com/literature.htm. Accessed: 2017-02-15.

[88] Wirerope Works, Inc. Technical bulletin no. 9 - fatigue. http://www.wwwrope.com/literature.htm. Accessed: 2017-02-15.

[89] Kai Xu and Nabil Simaan. Actuation compensation for flexible surgical snake-like robots with redundant remote actuation. In *Robotics and Automation, 2006. ICRA 2006. Proceedings 2006 IEEE International Conference on*, pages 4148–4154. IEEE, 2006.

[90] IL Yeoh, Per G Reinhall, Martin C Berg, and Eric J Seibel. Self-contained image recalibration in a scanning fiber endoscope using piezoelectric sensing. *Journal of Medical Devices*, 9(1):011004, 2015.

[91] Lingtao Yu, Zhengyu Wang, Wenjie Wang, Hongwei Li, and Lan Wang. Research on micromanipulators clamping force sensing based on static wirerope tension of a surgical robot. *Advances in Mechanical Engineering*, 7(4):1687814015581246, 2015.

[92] Dekun Zhang, Kai Chen, Xiaofan Jia, Dagang Wang, Songquan Wang, Yong Luo, and Shirong Ge. Bending fatigue behaviour of bearing ropes working around pulleys of different materials. *Engineering Failure Analysis*, 33:37–47, 2013.